

Damage Analysis and Fundamental Studies

Quarterly Progress Report
October-December 1983

February 1984

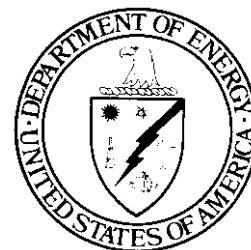
**U.S. Department of Energy
Office of Energy Research
Office of Fusion Energy
Washington, DC 20545**

NOTICE

This report was prepared as an account of work sponsored by an agency of the United States Government. Neither the United States Government nor any agency thereof, nor any of their employees, nor any of their contractors, subcontractors or their employees, makes any warranty, express or implied, **or** assumes any legal liability or responsibility for the accuracy, completeness, or any third party's use or the results of such use of any information, apparatus, product, **or** process disclosed, or represents that its use would not infringe privately owned rights. Reference herein to any specific commercial product, process, or service by trade name, trademark, manufacturer, or otherwise, does not necessarily constitute or imply its endorsement, recommendation, or favoring by the United States Government or any agency thereof or its contractors or subcontractors.

Printed in the United States of America
Available from
National Technical Information Service
U.S. Department of Commerce
5285 Port Royal Road
Springfield, VA 22161

NTIS price codes
Printed copy: A 05
Microfiche copy: A01



Damage Analysis and Fundamental Studies

Quarterly Progress Report
October-December 1983

February 1984

U.S. Department of Energy
Office of Energy Research
Office of Fusion Energy
Washington, DC 20545

FOREWORD

This report is the twenty-fourth in a series of Quarterly Technical Progress Reports on *Damage Analysis and Fundamental Studies* (DAFS), which is one element of the Fusion Reactor Materials Program, conducted in support of the Magnetic Fusion Energy Program of the U.S. Department of Energy (DOE). The first eight reports in this series were numbered DOE/ET-0065/1 through 8. Other elements of the Fusion Materials Program are:

- Alloy Development for Irradiation Performance (ADIP)
- Plasma-Materials Interaction (PMI)
- Special Purpose Materials (SPM).

The DAFS program element is a national effort composed of contributions from a number of National Laboratories and other government laboratories, universities, and industrial laboratories. It was organized by the Materials and Radiation Effects Branch; DOE/Office of Fusion Energy, and a Task Group on *Damage Analysis and Fundamental Studies*, which operates under the auspices of that branch. The purpose of this series of reports is to provide a working technical record of that effort for the use of the program participants, the fusion energy program in general, and the DOE.

This report is organized along topical lines in parallel to a Program Plan of the same title so that activities and accomplishments may be followed readily, relative to that Program Plan. Thus, the work of a given laboratory may appear throughout the report. Note that a new chapter has been added on Reduced Activation Materials to accommodate work on a topic not included in the early program plan. The Contents is annotated for the convenience of the reader.

This report has been compiled and edited under the guidance of the Chairman of the Task Group On *Damage Analysis and Fundamental Studies*, D. G. Doran, Hanford Engineering Development Laboratory (HEDL). His efforts, those of the supporting staff of HEDL, and the many persons who made technical contributions are gratefully acknowledged. T. C. Reuther, Materials and Radiation Effects Branch, is the DOE counterpart to the Task Group Chairman and has responsibility for the DAFS program within DOE.

G. M. Haas, Chief
Reactor Technologies Branch
Office of Fusion Energy

CONTENTS

| | <u>Page</u> |
|--|-------------|
| Foreword | iii |
| CHAPTER 1: IRRADIATION TEST FACILITIES | 1 |
| 1. <u>RTNS-II Irradiations and Operations (LLNL)</u> | 2 |
| <i>Irradiations were performed for 13 different experimenters during this quarter. The 50-cm targets are now in use on both the right and left machines. The extraction power supply upgrade for the left and right machines was completed.</i> | |
| CHAPTER 2: DOSIMETRY AND DAMAGE PARAMETERS | 4 |
| 1. <u>Fission Reactor Dosimetry - HFIR-T1, CTR39 (ANL)</u> | 5 |
| <i>Dosimetry measurements and damage calculations are reported for the T1 and CTR39 irradiations in HFIR. The T1 experiment had a maximum fluence of 1.47×10^{23} n/cm² with 29 dpa and 2291 appm He in 316 SS, while CTR39 had 5.32×10^{22} n/cm² with 13 dpa and 617 appm He in 316 SS.</i> | |
| 2. <u>Helium Production Cross Sections for 14.8-MeV Neutrons (RI-ESG)</u> | 9 |
| <i>Total helium production cross-section measurements have been completed for the elements Be, O, Cr, and Mn, based on samples irradiated in the 14.8-MeV T(d,n) neutron spectrum of RTNS-II.</i> | |
| 3. <u>TKIO-1 Tritium Breeding Experiment in ORR (ANL)</u> | 12 |
| <i>The TRIO-1 solid breeder (LiAlO₂) tritium experiment has been completed in ORR. Tritium was extracted by a helium purge stream and counted on-line, providing a time- and temperature-dependent profile of tritium release. These tritium measurements and the dosimetry-based tritium calculations are in excellent agreement with a total tritium generation of 35.1 Ci, corresponding to a ⁶Li burnup of 33% (0.18% of total lithium).</i> | |
| CHAPTER 3: REDUCED ACTIVATION MATERIALS | 16 |
| 1. <u>Reduced Activation Activities (HEDL)</u> | 17 |
| <i>Four reduced activation alloy classes, two austenitic and two ferritic, have been incorporated into the MOTA-1B experiment in the FFTF reactor to provide an early assessment of the suitability of such alloys for fusion reactor service.</i> | |

CONTENTS (Cont'd)

| | Page |
|---|------|
| CHAPTER 4: FUNDAMENTAL MECHANICAL BEHAVIOR | 19 |
| 1. <u>Sub-critical Crack Growth in HT9 (PNL)</u> | 20 |
| <i>Sub-critical crack growth measurements have been made on HT9 at 25°C in a 1 N H₂SO₄ solution with the sample held at a cathodic potential of -600 mV (SCE). The tensile ductility of HT9 has previously been shown to be a minimum at -600 mV (SCE). The sub-critical crack growth behavior of HT9 was similar for material in the tempered (760°C/2.5 h) or tempered + segregated (540°C/240 h) conditions. A rising load fracture threshold of 20 MPa√m and a decreasing load fracture threshold of 65 MPa√m was measured. A rising load fracture toughness of 110√m was determined from extrapolation of the stage III crack growth curve. A K independent stage II was observed, and a stage II crack growth rate of 0.5 to 1 x 10⁻⁵ mm/s was measured.</i> | |
| 2. <u>Critical Leak Rate Flaw Sizes for Water of Lithium-Cooled Fusion Reactors (PNL)</u> | 30 |
| <i>Results suggest that the critical leak rate flaw size for helium and water are the smallest flaws that may affect reactor performance and that the threshold for subcritical crack growth in fatigue is a critical material property. Creep processes are shown to have a significant effect on the critical leak rate flaw size.</i> | |
| CHAPTER 5: CORRELATION METHODOLOGY | 37 |
| 1. <u>Swelling of Fe-Ni-Cr Ternary Alloys at High Exposure (HEDL)</u> | 38 |
| <i>Acquisition of higher fluence data (70-110 dpa) on the swelling of austenitic Fe-Ni-Cr ternary alloys confirms the conclusion drawn earlier that the eventual swelling rate of all austenitic Fe-Ni-Cr alloys in EBR-II is ~1%/dpa in the range 400-650°C. The influence of composition and temperature lies only in the duration of the transient regime of swelling. At temperatures below 500°C, saturation of swelling appears to be occurring, often at very high swelling levels. The saturation level decreases with decreasing temperature, increasing nickel level and decreasing chromium content.</i> | |

CONTENTS (Cont'd)

| | <u>Page</u> |
|--|-------------|
| 2. <u>Transmutation of Manganese-Substituted Steels in STARFIRE (HEDL)</u> | 46 |
| <i>The transmutations calculated for a STARFIRE first wall employing the manganese substitution alloys currently under investigation in the DAFS program are not expected to alter the phase stability of these alloys.</i> | |
| 3. <u>Recent Insights on the Swelling and Creep of Irradiated Austenitic Alloys (HEDL)</u> | 49 |
| <i>It appears that all austenitic Fe-Ni-Cr alloys eventually swell during neutron irradiation at a rate of $\sim 1\%/dpa$ over a surprisingly large range of temperature. In addition, there is no evidence that saturation of swelling will occur in commercial alloys at engineering-relevant levels. The sensitivities of swelling to variations in composition, fabrication, and environment lie almost exclusively in the duration of the transient regime of swelling. Irradiation creep rates at high exposures are also expected to exhibit a similar parametric insensitivity, largely because the major creep contribution appears to be proportional to the swelling rate.</i> | |
| 4. <u>Swelling of AISI 304L in Response to Simultaneous Variations in Stress and Displacement Rate (ANL-HEDL)</u> | 62 |
| <i>The duration of the transient regime of neutron-induced swelling in annealed AISI 304L at 400°C is sensitive to both stress and displacement rate variations. However, the duration cannot be reduced below an exposure of ~ 10 dpa, which has been found to be characteristic of all Fe-Ni-Cr austenitic alloys. This is four times larger than that currently assumed in the stress-affected swelling equation for 20% cold-worked AISI 316.</i> | |
| 5. <u>Simple Polynomial Expressions for the Helium Equation of State (U. Wisc)</u> | 68 |
| <i>The compressibility factor $z = pV/NkT$ for gaseous and solid helium has been fitted to expressions of the form $z = A + Bx + Cx^2 + Dx^3$, where x is the density, and the coefficients A through D are functions of temperature.</i> | |

CHAPTER 1

IRRADIATION TEST FACILITIES

RTNS-II IRRADIATIONS AND OPERATIONS

C.M. Logan and D. W. Heikkinen (Lawrence Livermore National Laboratory)

1.0 Objective

The objectives of this work are operation of RTNS-II (a 14-MeV neutron source facility), machine development, and support of the experimental program that utilizes this facility. Experimenter services include dosimetry, handling, scheduling, coordination, and reporting. RTNS-II is dedicated to materials research for the fusion power program. Its primary use is the development of models of high-energy neutron effects needed to project engineering data obtained in fusion reactors to fusion environments. The facility is currently operated jointly by USDOE and Japan-Mombusha.

2.0 Summary

Irradiations were performed for 13 different experimenters during this quarter. Fifty centimeter targets are being used on the right and left machines now. Ion source development continues. The extraction power supply upgrade for the left and right machines was completed.

3.0 Program

Title: RTNS-II operations (WZJ-16)
Principal Investigator: C. M. Logan
Affiliation: Lawrence Livermore National Laboratory

4.0 Relevant DAFS Program Plan Task/Subtask

Task II.A.2,3,4,
Task II.B.3,4
Task II.C.1,2,6,11,18.

5.0 Irradiation - M. Logan, D. W. Heikkinen and M. W. Guinan

During this quarter, irradiations (both dedicated and add-on) were done for the following people.

| <u>Experimenter</u> | <u>P or A*</u> | <u>Sample Irradiated</u> |
|---------------------|----------------|--|
| J. Fowler (LANL) | P | MACOR - electrical and mechanical properties. |
| R. Smither (ANL) | A | Al - the $^{27}\text{Al}(n,2n)^{26}\text{Al}$ cross section near threshold |
| R. Borg (LLNL) | A | 1. NiRh - magnetic properties 2. KBr and KI - inert gas production and diffusion. |
| K. Saneyoshi (TIT) | A | LiF - determine the feasibility of TLD self irradiation as a tritium production |

| <u>Experimenter</u> | <u>P or A*</u> | <u>Sample Irradiated</u> |
|-----------------------------|----------------|--|
| K. Shinohara (Kyushu) | A | Cu - fluence dependence of yield stress |
| D. Heikkinen (LLNL) | A | Nb - dosimetry calibration |
| N. Itoh (Nagoya) | P | Ceramics - in-situ expansion due to radiation damage |
| K. Abe (Tohoku) | P | Metals - mechanical properties |
| H. Matsui (Tohoku) | | |
| H. Kayano (Tohoku) | | |
| M. Kiritani (Hokkaido) | | |
| H. Takahashi (Hokkaido) | | |
| K. Shinohara (Kyushu) | | |
| E. Kuramoto (Kyushu) | | |
| N. Yoshida (Kyushu) | | |
| T. Kinoshita (Kyushu) | | |
| N. Igata (Tokyo) | | |
| A. Kohyama (Tokyo) | | |
| K. Mihayara (Tokyo) | | |
| H. Kawanishi (Tokyo) | | |
| K. Kamada (Nagoya) | | |
| M. Iseki (Nagoya) | | |
| K. Sata (Nagoya) | | |
| K. Sumita (Osaka) | A | Insulators - electrical and mechanical properties |
| Y. Tabata (Tokyo) | A | Polymers - tensile strength |
| Y. Yamaoka (Kyoto) | A | Polymers - tensile strength |
| C. Ichihara (Kyoto) | A | MgO - light absorption for dosimetry |
| F. Deadrick (LLNL) | A | Linear amplifiers - performance |

*P - primary, A = Add-on

5.1 RTNS-II Sta - M. Logan and D. W. Heikkinen

The ion source system development for the right and left machine continues. Deuteron currents over 120 mA had already been obtained.

Both the left and right machines are now operating with 35-kV Cober extraction power supplies.

On November 30, 1983, both the right and left machines were in operation at the same time using 50-cm targets. This was a historical event for RTNS-II.

6.0 Future Work

Irradiations will be continued for J. Fowler (LAML), R. Borg, (LLNL), K. Abe (Tohoku) et al., Y. Tabata (Tokyo), Y. Yamaoka (Kyoto), K. Sumita (Osaka) and K. Saneyoshi (TIT). Also during this period, irradiations for Y. Shimomura (Hiroshima), H. Heinisch (HEDL) and D. Methaway (LLNL) will be initiated.

CHAPTER 2

DOSIMETRY AND DAMAGE PARAMETERS

FISSION REACTOR DOSIMETRY - HFIR - T1 - CTR39)

L. R. Greenwood (Argonne National Laboratory)

1.0 Objective

To characterize neutron irradiation facilities in terms of neutron flux, spectra, and damage parameters (dpa, gas generation, transmutation) and to measure these exposure parameters during fusion materials irradiations.

2.0 Summary

Dosimetry measurements and damage calculations are summarized for the T1 and CTR39 irradiations in MIR. The status of all other experiments is summarized in Table 1.

TABLE 1

| STATUS OF DOSIMETRY EXPERIMENTS | | |
|---------------------------------|---------------------|--------------------------|
| | Facility/Experiment | Status/Comments |
| ORR | - MFE 1 | Completed 12/79 |
| | - MFE 2 | Completed 06/81 |
| | - MFE 4A1 | Completed 12/81 |
| | - MFE 4A2 | Completed 11/82 |
| | - MFE 4B | Samples Received 09/83 |
| | - MFE 4C | Irradiation in Progress |
| | - TBC 07 | Completed 07/80 |
| | - TRIO-Test | Completed 07/82 |
| | - TRIO-1 | completed 12/83 |
| | - Hf Test | Planned for 01/84 |
| | HFIR | - CTR 32 |
| - CTR 31, 34, 35 | | Completed 04/83 |
| - CTR 30 | | Irradiations in Progress |
| - T2, RB1 | | Completed 09/83 |
| - T1, CTR 39 | | Completed 01/84 |
| - RB2, RB3, T2 | | Irradiations in Progress |
| - CTR 40-52 | | Irradiations in Progress |
| Omega West | - JP 1-8 | Irradiations in Progress |
| | - Spectral Analysis | Completed 10/80 |
| EBR II | - HEDL1 | Completed 05/81 |
| | - HEDL2 | Samples Sent 05/83 |
| IPNS | - X287 | Completed 09/81 |
| | - Spectral Analysis | Completed 01/82 |
| | - LANL1 (Hurley) | completed 06/82 |
| | - Hurley | Completed 02/83 |
| | - Coltman | Completed 08/83 |

3.0 Program

Title: Dosimetry and Damage Analysis
 Principal Investigator: L. R. Greenwood
 Affiliation: Argonne National Laboratory

4.0 Relevant DAFS Program Plan Task/Subtask

Task II.A.1 Fission Reactor Dosimetry

5.0 Accomplishments and Status

Measurements and calculations have been completed for the T1 and CTR39 irradiations in the High Flux Isotopes Reactor (HFIR) at Oak Ridge National Laboratory. Both experiments were designed to study ferritic steels and consisted of tensile and fatigue specimens. The irradiation histories are, as follow:

| <u>Experiment</u> | <u>Reactor Position</u> | <u>Dates</u> | <u>Exposure, MWD</u> |
|-------------------|-------------------------|--------------|----------------------|
| CTR39 | PTP | 6/82 - 10/82 | 13,004 |
| T1 | Target | 2/81 - 8/82 | 32,272 |

Dosimeters were located at two heights in T1 and three heights in the CTR39 subassembly. The T2 capsules contained Ni, Cu, Co-A1, Mn-Cu, Nb, Ti, Fe, and Zr dosimeter wires while the CTR39 capsules contained only Fe, Ti, Mn-Cu, and Co-A1 dosimeters.

The measured activation rates are listed in Table 2. When the present values were compared to previous values^{1,2} measured in similar locations in HFIR, it was apparent that the $^{54}\text{Fe}(n,p)^{54}\text{Mn}$ and $^{55}\text{Mn}(n,2n)^{54}\text{Mn}$ reaction rates showed much more scatter (15-20%) than expected. This can be easily explained by the uncertainty in the burnup corrections for ^{54}Mn since the thermal cross section is not well known.

TABLE 2

ACTIVITY RATES MEASURED IN FIR-T1, CTR39
(Values normalized to 100 MW; corrected for burnup)

| Reaction | Activity Rate, atom/atom-s | | | |
|--|----------------------------|------|-------|-------|
| | Height, cm: | 7.22 | 16.95 | |
| T1 Experiment: | | | | |
| $^{58}\text{Fe}(n,\gamma)^{59}\text{Fe}$ | (10-9) | 2.26 | 1.82 | |
| $^{59}\text{Co}(n,\gamma)^{60}\text{Co}$ | (10-8) | -- | 6.03 | |
| $^{54}\text{Fe}(n,p)^{54}\text{Mn}$ | (10-11) | 5.58 | 4.36 | |
| $^{46}\text{Ti}(n,p)^{46}\text{Sc}$ | (10-12) | -- | 6.36 | |
| $^{55}\text{Mn}(n,2n)^{54}\text{Mn}$ | (10-13) | 1.59 | 1.35 | |
| $^{63}\text{Cu}(n,\alpha)^{60}\text{Co}$ | (10-13) | -- | 2.99 | |
| CTR39 Experiment: | | 2.00 | 10.89 | 19.78 |
| $^{58}\text{Fe}(n,\gamma)^{59}\text{Fe}$ | (10-9) | 2.10 | 1.84 | 1.30 |
| $^{59}\text{Co}(n,\gamma)^{60}\text{Co}$ | (10-8) | 7.54 | 6.57 | 4.57 |
| $^{54}\text{Fe}(n,p)^{54}\text{Mn}$ | (10-11) | 7.36 | 6.55 | 4.68 |
| $^{55}\text{Mn}(n,2n)^{54}\text{Mn}$ | (10-13) | 2.14 | 1.95 | 1.42 |

ENDF/B-IV³ listed the ^{54}Mn thermal cross section as <10b. The newly released ENDF/B-V⁴ value is 38b. If we compare reaction rates measured in similar positions over various exposure times (6000 - 30000 MWD), then both reactions show reasonably good agreement (5-10%) using a ^{54}Mn thermal cross section of about 10b. Consequently, we have adopted this value for the present data. Unfortunately, this means that all previous

$^{54}\text{Fe}(n,p)$ and $^{55}\text{Mn}(n,2n)$ rates should be revised; however, the corrections, which scale with the exposure, are less than 10% in all cases. Since these reactions are not the only ones used to determine fluences and damage parameters, these data should have changes of less than 5%. Data from future irradiations in HFIR will help us to further refine our estimate of the ^{54}Mn thermal cross section and all data will be revised as necessary.

The present gradient data is well-described by a quadratic polynomial and the coefficients are listed in Table 3. Using this function and the midplane values, users can readily determine fluence or damage rates at any point in the subassembly. Of course, helium production in nickel is not so easily determined and the helium and dpa rates are listed separately in Table 4. A more complete description of helium measurements and calculations was presented at the Albuquerque meeting.⁵

TABLE 3

NUTRON FLUENCE AND DAMAGE PARAMETERS FOR HFIR-T1, CTR39
 Values are listed at midplane; gradients are described by $f = a(1 + bz + cz^2)$ where $b = 1.95 \times 10^{-4}$, $c = -9.75 \times 10^{-4}$

| Neutron Fluence, $\times 10^{22}$ n/cm ² | | T1 | CTR39 |
|---|--|-------|-------|
| Total | | 14.74 | 5.92 |
| Thermal (<.5 eV) ^a | | 7.00 | 2.47 |
| Fast (>.11 MeV) | | 3.37 | 1.54 |

| Element | T1 | | CTR39 | | |
|---------------------|------------------|----------|--------|----------|-------|
| | dpa | He, appm | dpa | He, appm | |
| Al | 43.85 | 19.41 | 20.23 | 9.86 | |
| Ti | 27.84 | 13.37 | 12.88 | 6.58 | |
| V | 31.25 | 0.67 | 14.41 | 0.33 | |
| Cr | 27.37 | 4.49 | 12.71 | 2.26 | |
| Mn ^b | 30.80 | 3.93 | 14.01 | 2.00 | |
| Fe | 24.12 | 7.89 | 11.25 | 4.02 | |
| Co ^b | 32.42 | 3.89 | 14.22 | 1.98 | |
| Ni ^c | Fast | 104.68 | 12.10 | 53.32 | |
| | ⁵⁹ Ni | 30.82 | 17476. | 8.23 | 4668. |
| | Total | 57.05 | 17581. | 20.33 | 4721. |
| cu | 23.67 | 7.05 | 10.97 | 3.58 | |
| Nb | 23.35 | 1.44 | 10.86 | 0.74 | |
| Mo | 17.47 | -- | 8.08 | -- | |
| 316 SS ^d | 28.94 | 2291. | 12.66 | 617. | |

^aThe 2200 m/s thermal flux is equal to 0.866 times the value listed.

^bThermal self-shielding must be considered for (n,γ) damage.

^cSee Table IV for Ni gradients.

^d316 SS: Fe(0.645), Ni(0.13), Cr(0.18), Mn(0.019), Mo(0.026).

TABLE 4

HELIUM AND DPA GRADIENTS FOR NICKEL IN HFIR-T2, RB1
 Helium values include ⁵⁹Ni and fast reactions
 dpa values include extra thermal effect (He/567)
 Gradients are very nearly symmetric about midplane

| Height, cm | T1 | | CTR39 | |
|------------|----------|------|----------|------|
| | He, appm | dpa | He, appm | dpa |
| 0 | 17,581 | 57.1 | 4,721 | 20.3 |
| 3 | 17,429 | 56.6 | 4,666 | 20.1 |
| 6 | 16,932 | 55.0 | 4,487 | 19.5 |
| 9 | 16,105 | 52.4 | 4,192 | 18.5 |
| 12 | 14,915 | 48.8 | 3,781 | 17.0 |
| 15 | 13,372 | 44.0 | 3,268 | 15.2 |
| 18 | 11,439 | 38.1 | 2,660 | 13.0 |
| 21 | 9,113 | 31.0 | 1,984 | 10.4 |
| 24 | 6,437 | 22.9 | 1,284 | 7.6 |

6.0 References

1. L. R. Greenwood, "Fission Reactor Dosimetry - HFIR - CTR31, 32, 34, and 35," Damage Analysis and Fundamental Studies Quarterly Progress Report, DOE/ER-0046/13, pp. 17-26, May 1983.
2. L. R. Greenwood, Fission Reactor Dosimetry - HFIR-T2 and RB1, Damage Analysis and Fundamental Studies Quarterly Progress Report, DOE/ER-0046/15, in print, 1984.
3. S. F. Mughabghab and D. 1. Gerber, "Neutron Cross Sections," Resonance Parameters, BNL325, Third Edition, Volume I, Brookhaven National Laboratory, June 1973.
4. S. F. Mughabghab, M. Divadeenam, N. E. Holden, "Neutron Cross Sections: Neutron Resonance Parameters and Thermal Cross Sections, Volume I, Part A: Z = 1-60, Academic Press, New York, 1981.
5. L. R. Greenwood, D. W. Kneff, R. P. Skowronski, and F. M. Mann, " Comparison of Measured and Calculated Helium Production in Nickel Using Newly Evaluated Neutron Cross Sections for ^{59}Ni ," Proceedings of the Third Topical Meeting on Fusion Reactor Materials, Albuquerque, NM, September 1983, to be published.

7.0 Future Work

Samples are being analyzed for the MFE4B irradiation in ORR. A test of the Hf shield design for the MFE4A experiment in ORR is planned for January 1984.

8.0 Publications

1. L. R. Greenwood, Neutron Measurements and Radiation Damage Calculations for Fusion Materials Studies, presented at the 1983 Winter Meeting of the American Nuclear Society, San Francisco, CA, November 1983.

HELIUM PRODUCTION CROSS SECTIONS FOR 14.8-MeV NEUTRONS

D. W. Kneff, B. M. Oliver, R. P. Skowronski, and H. Farrar IV (Rockwell International, Energy Systems Group)

1.0 Objective

The objectives of this work are to measure helium generation rates of materials for Magnetic Fusion Reactor applications in the -14.8-MeV T(d,n) neutron environment, and to develop helium accumulation neutron dosimeters for this test environment.

2.0 Summary

The total helium production cross sections of Be, O, Cr, and Mn have been measured for -14.8-MeV T(d,n) neutrons from RTNS-II. Additional helium analyses were performed for selected encapsulated samples of Be, Cr, and Mn to test the helium retention of those elements.

3.0 Program

Title: Helium Generation in Fusion Reactor Materials
Principal Investigators: D. W. Kneff and H. Farrar IV
Affiliation: Rockwell International, Energy Systems Group

4.0 Relevant OAFS Program Plan Task/Subtask

Subtask II.A.4.2 T(d,n) Helium Gas Production Data

5.0 Accomplishments and Status

The total helium production cross sections of the elements Be, O, Cr, and Mn have been measured for -14.8-MeV T(d,n) neutrons from the Rotating Target Neutron Source-I1 (RTNS-II). The measurements were made by irradiating multiple samples of each material of interest in close geometry to the RTNS-II source and subsequently analyzing the samples for helium by high-sensitivity gas mass spectrometry. (1) The irradiation was a joint Rockwell International-Argonne National Laboratory (ANL)-Lawrence Livermore National Laboratory (LLNL) experiment that also included numerous other helium generation materials. (2) The neutron fluence received by each irradiated sample was determined by detailed neutron fluence mapping of the irradiation volume using a combination of radiometric and helium accumulation dosimetry, as described previously. (3,4) Various aspects of the present measurements were supported by the Office of Fusion Energy and Office of Basic Energy Sciences of the U.S. Department of Energy.

Several of the present set of samples were individually vacuum-encapsulated in miniature platinum capsules for irradiation and subsequent helium analysis. The manganese samples, and selected samples of Be and Cr, were encapsulated to ensure and verify complete sample helium retention. The oxygen samples were irradiated in the oxide forms PbO and Nb₂O₅, and were encapsulated to maintain sample integrity as well as complete helium retention. These oxides were selected because of the low Pb and Nb helium generation cross sections (0.62 ± 0.05 mb and 14 ± 1 mb, respectively), which were measured separately as part of this RTNS-II experiment. (3,5) Platinum was selected as the encapsulating material because of its relatively small helium generation cross section (0.71 ± 0.10 mb), which was also measured as part of this experiment. (6) Each capsule and its contents were vaporized and analyzed together for helium. A calculated platinum helium generation contribution, based on its measured cross section, the capsule mass, and the neutron fluence at the capsule location, was subtracted from the total amount of helium measured.

TABLE 1

EXPERIMENTAL HELIUM GENERATION CROSS SECTIONS
FOR -14.8-MeV NEUTRONS

| Material | Cross Section (mb) | Material | Cross Section (mb) |
|----------|--------------------|----------|--------------------|
| Be | 1018 ± 83 | Cr | 34 • 3 |
| O | 401 ± 32 | Mn | 28 ± 2 |

Each platinum capsule, and each unencapsulated Be and Cr sample, was etched before analysis; to eliminate surface recoil effects.

Helium measurements were made in two analysis steps for selected platinum capsules containing Be, Mn, and Cr. The first analysis step involved shearing the capsule while it was in the mass spectrometer vacuum system, and measuring any helium that had been released from the sample into the capsule void. In the second analysis step, the capsule plus its contents were vaporized to measure the helium retained in the sample (plus any helium that recoiled from the sample into the inner capsule wall). The results of these two-step capsule analyses, plus several analyses of unencapsulated Be and Cr samples, showed negligible (<0.2%) helium diffusion from the Cr and Mn samples, and a small 1% loss from beryllium (based primarily on one shearing measurement). The Cr and Mn results verify the helium retention in Cr and Mn under RTNS irradiation conditions without the need for encapsulation, as has been verified previously for other RTNS-irradiated metals using a variety of irradiation conditions. A 1% correction was made to the helium measurement for each of the unencapsulated beryllium samples.

The oxygen cross section was obtained by first determining the PbO and Nb₂O₅ cross sections, and then unfolding the Pb and Nb cross sections from these results. The oxide stoichiometries used in the derivation of the oxygen cross section were obtained from an independent series of Rockwell analyses comparing the helium generation in four oxide powders (Al₂O₃, GeO, Nb₂O₅, and PbO) in a fast breeder reactor neutron environment. The results showed agreement between the oxygen helium generation rates for Al₂O₃, GeO, and Nb₂O₅, assuming stoichiometries given by their empirical formulas. PbO was found to be non-stoichiometric, with the relative Pb and O concentrations better represented by Pb_{0.134}O_{1.015}. Qualitative x-ray diffraction also indicated the presence of other oxidation states. Fast-neutron activation analysis was also investigated as a tool to measure PbO and Nb₂O₅ stoichiometries, but initial results indicated that uncertainties in the γ attenuation corrections were unacceptably large for the standard test geometry employed, so accurate stoichiometries could not be obtained.

The measured total helium production cross sections for the four elements are given in Table 1. The beryllium cross section is large, as expected, because it is dominated by the 2α contribution from the ${}^9\text{Be}(n,2n){}^8\text{Be} \rightarrow 2\alpha$ reaction.⁽⁷⁾ The chromium cross section has been measured in a previous Rockwell RTNS-I experiment using unencapsulated samples,⁽²⁾ and that result (34 ± 4 mb) is in excellent agreement with the 34 • 3 mb cross section from the present RTNS-II measurement.

6.0 References

1. H. Farrar IV, W. N. McElroy, and E. P. Lippincott, "Helium Production Cross Section of Boron for Fast-Reactor Neutron Spectra," Nucl. Technol., **25**, 305 (1975).
2. D. W. Kneff, B. M. Oliver, M. M. Nakata, and H. Farrar IV, "Experimental Helium Generation Cross Sections for Fast Neutrons," J. Nucl. Mater., **103 & 104**, 1451 (1981).
3. D. W. Kneff, B. M. Oliver, M. M. Nakata, and H. Farrar IV, "RTNS-II Fluence Mapping and Helium Generation Cross Sections," in Damage Analysis and Fundamental Studies. Quarterly Progress Report January-March 1982, DOE/ER-0046/9, U.S. Department of Energy, 16 (1982).
4. D. W. Kneff, B. M. Oliver, M. M. Nakata, and H. Farrar IV, "Helium Production Cross Sections for 14.8-MeV Neutrons," in Damage Analysis and Fundamental Studies, Quarterly Progress Report April - June 1982, DOE/ER-0046/10, U.S. Department of Energy, 19 (1982).

5. B. M. Oliver, O. W. Kneff, M. M. Nakata, and H. Farrar IV. "Helium Generation Cross Sections for 14.8-MeV Neutrons," in Damage Analysis and Fundamental Studies, Quarterly Progress Report July - September 1981, DOE/ER-0046/77, U.S. Department of Energy, 28 (1981).
6. B. M. Oliver, O. W. Kneff, M. M. Nakata, and H. Farrar IV, "Helium Generation Cross Sections for 14.8-MeV Neutrons, in "Damage Analysis and Fundamental Studies, Quarterly Progress Report October - December 1981, DOE/ER-0046/8, Vol. 1, U.S. Department of Energy, 31 (1982).
7. See, for example, D. I. Garber and R. R. Kinsey, Neutron Cross Sections. Volume II, Curves, BNL 325, Third Edition, Volume II, Brookhaven National Laboratory (1976).

7.0 Future Work

A comprehensive paper covering all of Rockwell's 14.8-MeV $\tau(d,n)$ total helium production measurements will be submitted for publication shortly. Further RTNS-II cross section analyses will be performed for low-level samples when a constant-temperature vaporization furnace, now being developed under an Office of Basic Energy Sciences program, is completed. The Office of Basic Energy Sciences is also sponsoring the current analysis of a joint LLNL-Rockwell RTNS-I experiment to measure the 6Li and 7Li helium production cross sections using lead-encapsulated metal samples.

8.0 Publications

None.

THE TRIO-1 TRITIUM BREEDING EXPERIMENT IN ORR

L. R. Greenwood and R. G. Clemner (Argonne National Laboratory)

1.0 Objective

To characterize neutron irradiation facilities in terms of neutron flux, spectra, and damage parameters (gas generation, dpa, transmutation) and to measure these exposure data during fusion materials experiments.

2.0 Summary

The TRIO-1 solid breeder (γ -LiAlO₂) tritium experiment has been completed in ORR. The experiment was designed to test in-situ tritium recovery and heat transfer performance. The results showed that nearly all of the tritium generated was recovered. The on-line tritium measurements were in good agreement with our dosimetry calculations. The total tritium generated was 35.1 Ci corresponding to a ⁶Li burnup of about 33% (0.18% of total lithium).

3.0 Program

Title: Dosimetry and Damage Analysis
Principal Investigator: L. R. Greenwood
Affiliation: Argonne National Laboratory

4.0 Relevant OAFS Program Plan Task/Subtask

Task II.A.1 Fission Reactor Dosimetry
Task II.A.4 Gas Generation Rates

5.0 Accomplishments and Status

The TRIO-01 experiment has been completed in the Oak Ridge Research Reactor (ORR) at the Oak Ridge National Laboratory. The present report is designed to focus on tritium measurements and calculations; a more complete description can be found in other recent publications.¹⁻⁴ The TRIO-01 experiment was designed to test in-situ tritium recovery and heat transfer performance of a candidate solid fusion breeder material, γ -LiAlO₂. To decrease self-shielding, Li depleted to 0.55% ⁶Li was used. The experiment was irradiated in Position A2 of the ORR from March 12 to June 13, 1983, for a total exposure of 2558 MWd. Neutron dosimeters were included with the sample, and the neutron spectrum was measured earlier in a mockup test described previously.⁵ In the mockup test, the ⁶Li burnup rate was measured by Oak Ridge National Laboratory and by Rockwell International. These measurements agreed with the ANL dosimetry-based calculations to within $\pm 4\%$.

In the actual TRIO-01 irradiation Fe, Ni, and Ti dosimetry wires were located in separate tubes on the west side, east side, and center of the TRIO capsule. The 10-mil wires were cut into six pieces, each about 1.4 cm long, and gamma counted by Ge(Li) spectroscopy. The reaction rates were corrected for decay during the irradiation using the flux histories from three self-powered neutron detectors which were wound around the outside of the TRIO capsule. It is worth noting that these flux histories show some significant local variations ($\pm 10\%$) which are not seen in the overall ORR power history. These variations are probably due to fuel changes during the course of the experiment. This effect is not very important for the interpretation of our dosimetry data since we used rather long-lived activities. However, the effect is quite important in the daily comparison of measured and calculated tritium levels, as will be discussed later.

The measured activity rates are listed in Table 1. Since there was no measurable gradient over the length of the experiment, results from all six samples were averaged. As can be seen, the thermal flux is about the same on the two outside (West/East) positions but drops about 32% in the center due to neutron self-shielding, primarily from the stainless steel sleeve (0.5 cm thick). This shielding effect was also seen in the mockup test.⁵ Analytical approximations indicate a shielding factor of about 0.74 for the stainless steel and an initial additional shielding of about 0.95 from the LiAlO₂ itself. The fast flux gradients are rather steep, 100% from west to east, due to the location of the A2 position on the corner of the ORR core assembly. This fast gradient is insignificant in terms of tritium generation and will have only a small effect on the damage rates. The activities measured in the TRIO-01 irradiation were about 30-40% lower than measured in the mockup tests, due to changes in the fuel loading of the ORR core.

TABLE 1

MEASURED ACTIVATION RATES FOR TRIO-01
Results are the average of six samples normalized to 100 MW

| Position | Activation Rate, atom/atom-s | | |
|----------|--|--|--|
| | ⁵⁸ Fe(n,γ) ⁵⁹ Fe | ⁵⁴ Fe(n,p) ⁵⁴ Mn | ⁴⁶ Ti(n,p) ⁴⁶ Sc |
| West | 1.24 E-10 | 5.34 E-12 | 7.47 E-13 |
| Center | 8.31 E-11 | 3.42 E-12 | 5.26 E-13 |
| East | 1.22 E-10 | 2.67 E-12 | 3.82 E-13 |

The activities in Table 1 were used to adjust the neutron spectrum measured in the mockup tests using the STAYSL computer code. The resultant neutron fluences and damage parameters are listed in Tables 2 and 3, respectively. The radiation damage is equivalent to about 0.6 MMy or about two months in a fusion reactor such as STARFIRE.

TABLE 2

ADJUSTED NEUTRON FLUENCES

| Energy, MeV | Neutron Fluence, x 10 ²⁰ n/cm ² | | |
|-------------------|---|-------|------|
| | Center | West | East |
| Total | 19.1 | 28.7 | 19.7 |
| Thermal (<.5 eV)* | 6.93 | 10.30 | 9.52 |
| 0.5 eV - 0.1 MeV | 6.01 | 8.98 | 5.13 |
| >0.1 MeV | 6.15 | 9.05 | 5.00 |

*The 2200 m/s thermal flux is 0.886 times the quoted value.

TABLE 3

DAMAGE PARAMETERS FOR TRIO-01

| | Source | Damage |
|-------|-----------------------|-------------------------|
| dpa: | ⁶ Li(n,α)t | 0.30 |
| | Fast Reactions | 0.51 |
| | Total | 0.81 |
| Rads: | ⁶ Li(n,α)t | 1.67 x 10 ¹² |
| | Fast Reactions | 0.15 x 10 ¹² |
| | Gamma Heating* | 3.54 x 10 ¹² |
| | Total | 5.36 x 10 ¹² |

*Based on a value of 4.8 W/g measured by ORNL in the A2 position.

Tritium production can be directly calculated using our dosimetry data. The adjusted neutron flux spectrum was used to calculate an unshielded (outer) ⁶Li burnup rate of 9.70 x 10⁻⁸ atoms/atom-s and an average inner (shielded) rate of 5.87 x 10⁻⁸ atoms/atom-s. The self-shielding caused by the ⁶Li itself decreases during the experiment as the atoms are burned up. Over the 97 days of the run, we calculate that the shielding decreases from about 0.952 to 0.968. An iterative procedure was thus used to determine the daily tritium production. The fluxes from the self-powered neutron detectors were used to determine the daily fluence and hence the tritium and ⁶Li burnup. The self-shielding was then readjusted prior to the next calculation. The daily tritium generation is shown in Figure 1.

The total ⁶Li burnup was thus calculated to be 37.1% corresponding to a tritium generation of 39.2 Ci. This value is compared with other measurements in Table 4. Due to the uncertainties in the fluence measurements and self-shielding approximations, the calculated value has an uncertainty of 10-15%. Our calculated value is somewhat higher than the other measurements, although these other values have errors of 5-10%. In the mockup tests the ⁶Li measurements were also lower than our calculations. Using these lower rates would reduce the calculated tritium level to 37.5 Ci, in better agreement with the other data

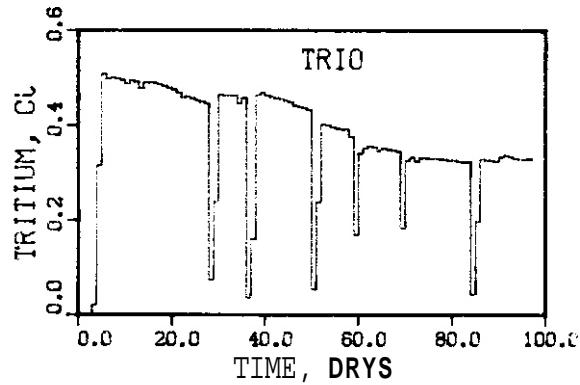


Figure 1. Calculated daily tritium generation for the 97 day TRIO-01 experiment in ORR. The large dips correspond to reactor shut-downs. The overall decline is due to the burnup of ${}^6\text{Li}$.

TABLE 4

SUMMARY OF TRITIUM RESULTS FOR TRIO-01
The quantity measured is indicated by the box

| Method | Tritium, C/I | Burnup (% ${}^6\text{Li}$) | Burnup (% Li) | Error, % |
|-----------------------|--------------|--------------------------------|------------------|----------|
| Tritium Collected | <u>35</u> | 33 | 0.18 | 5 |
| ${}^6\text{Li}$ Assay | 32 | <u>31</u> | <u>0.17</u> | 10 |
| Thermal Gradient | 35 | <u>33</u> | 0.18 | 10 |
| Dosimetry | <u>39</u> | <u>38</u> | 0.21 | 10-15 |
| Average | <u>35</u> | <u>33</u> | <u>0.18</u> | <u>5</u> |

The tritium values listed in Table 4 are consistent within the stated uncertainties and demonstrate that we can account for all tritium within an uncertainty of about 5%. The sample itself retained less than 0.1-wppm tritium, indicating a very low tritium inventory for a fusion reactor (e.g., <100 g in STARFIRE). The detailed tritium generation shown in Figure 1 is now being compared in detail with the actual tritium measurements. This comparison will provide significant new data concerning tritium release and transport over a temperature range from 400-700°C. Interesting information can also be extracted from variations due to changes in the sweep gas, nominally 0.1% H_2 in He at 100 cc/min.

The most important conclusions from the TRIO-01 experiment are as follows:

- (1) Nearly all of the tritium was released and recovered.
- (2) Tritium retention in the sample was <0.1 wppm following a run at 650°C with 0.1% H_2 in the sweep gas.
- (3) Irradiation to a Li burnup of 0.18% (equivalent to 0.6 MW-y/m²) produced no detectable changes in thermal conductivity or the microstructure of the LiAlO_2 .

6.0 References

1. R. G. Clemner, P. A. Finn, M. C. Billone, B. Misra, L. R. Greenwood, F. F. Oyer, I. T. Dudley, L. C. Bate, E. O. Clemner, P. W. Fischer, J. L. Scott, and J. S. Watson, "The TRIO-01 Experiment: In-Situ Tritium Recovery Results," Proceedings of the Tenth Symposium on Fusion Engineering, IEEE, Philadelphia, PA, December 1983.
2. R. G. Clemner, P. A. Finn, M. C. Billone, B. Misra, R. M. Arons, R. B. Peoppel, F. F. Dyer, I. T. Dudley, L. C. Bate, E. D. Clemner, J. L. Scott, J. S. Watson, and P. W. Fischer, "The TRIO-01 Experiment: In-Situ Tritium Recovery Results," Proceedings of the Third Topical Meeting on Fusion Reactor Materials, Albuquerque, NM, September 1983, to be published in the J. of Nucl. Mater.

3. R. G. Clemer, R. F. Malecha, and I. T. Dudley, "The TRIO-01 Experiment," Nucl. Technol./Fusion, Vol. 4, p. 83, September 1983.
4. B. Misra, R. G. Clemer, and P. A. Finn, "Heat Transfer Performance of a Solid Breeder Blanket Comparison of TRIO-01 Experimental Data with Models," ANS Transactions **45**, 176 (1983).
5. L. R. Greenwood, "Dosimetry Results for the TRIO Test in ORR," Damage Analysis and Fundamental Studies Quarterly Progress Report, DOE/ER-0046/10, pp. 9-15, August 1982.

7.0 Future Work

Plans are being made to study other solid breeder materials such as Li_2O , either as a follow-up experiment in ORR or in EBR II.

8.0 Publications

See Reference 1.

CHAPTER 3

REDUCED ACTIVATION MATERIALS

REDUCED ACTIVATION ACTIVITIES

F. A. Garner, H. R. Brager and O. S. Gelles (Hanford Engineering Development Laboratory)

1.0 Objective

The object of this effort is to provide information on the suitability for fusion reactor service of various alloy classes being developed to exhibit low residual radioactivity.

2.0 Summary

Four reduced activation alloy classes, two austenitic and two ferritic, have been incorporated into the MOTA-16 experiment in the FFTF reactor to provide an early assessment of the suitability of such alloys for fusion reactor service.

3.0 Program

Title: Irradiation Effects Analysis (AKJ)
Principal Investigator: D. G. Doran
Affiliation: Hanford Engineering Development Laboratory

4.0 Relevant OAFS Plan Task/Subtask

Task II.C.1 Effects of Materials Parameters on Microstructure

5.0 Accomplishments and Status

5.1 Introduction

The fusion materials community has recently begun to focus attention on the potential for development of fusion reactor structural materials with greatly reduced residual radioactivity. These materials would meet criteria for shallow burial and perhaps permit some recycling.

As discussed in an earlier report,¹ current guidelines place restrictions on several elements commonly used for stabilization of austenite or for solute-hardening or precipitate-strengthening. Thus, many of the reduced activation alloys currently under consideration lie in metallurgical and compositional regimes that are not well explored. Prior to committing large amounts of time, effort and funds in the exploration of such regimes, it is deemed necessary to secure an early indication of the relative behavior of these alloy classes in an irradiation environment.

An opportunity to quickly secure such an assessment arose in the reinsertion of the MOTA-1 experiment into the Fast Flux Test Facility (FFTF). The fusion materials portion of this experiment operates at three different temperatures (420, 500 and 600°C) and is currently scheduled to reach four exposure levels (15, 60, 105, 210 dpa). The specimens at the first exposure level will be available for examination shortly before the end of FY84. In early FY87 60 dpa will be reached, and 105 dpa will be reached in early FY88.

The types of specimens in each alloy class that were included into FFTF in MOTA-16 are discussed in the following sections.

5.2 Manganese-Substituted Austenitics - H. R. Brager and F. A. Garner

Two of the four DAFS fundamental alloy series are based on the Fe-Cr-Mn system. These alloys can be divided into two further categories, those with ~15% Mn and those with ~30%. The Invar-low swelling concept employed to develop the latter category has not yet been tested, however.

Five commercial alloys (2 US, 2 French and 1 Japanese), 10 Fe-Cr-Mn simple ternary alloys and 15 solute-modified Fe-Cr-Mn alloys were incorporated in MOTA-16. The solute-modified alloys are within the ADIP program. Space limitations dictated that the primary emphasis be placed on TEM disks, of which 720 were included. There were also included, however, 40 miniature tensile specimens of two alloys, R77 and R87.

5.3 Low-Activation Ferritics - D. S. Gelles

As described elsewhere, two ferritic alloy classes are currently being considered for low activation studies within the ADIP program. These are Fe-Cr-V bainitic alloys with properties similar to 2-1/4Cr-1Mo and Fe-Cr-V martensitic steels with properties similar to HT9.

To date nine alloys spanning these two classes have been manufactured in fifteen pound heats. Metallographic examination showed that eight of these had acceptable delta-ferrite levels. TEM disks were fabricated for all nine alloys and miniature tensile specimens were made for the eight alloys with acceptable delta-ferrite levels. The specimens included in MOTA-16 were primarily aimed at phase stability considerations (325 TEM disks) although 48 miniature tensile specimens were also included.

6.0 References

1. F. M. Mann and W. E. Kennedy Jr, "Activation of Components of Fusion Alloy," DAFS Quarterly Progress Report, DOE/ER-0046/14, August 1983, p. 63.
2. D. S. Gelles, H. R. Brager and F. A. Garner, "Low Activation Approaches to Materials Development," ADIP Quarterly Progress Report, DOE/ER-0045/10, March 1983, p. 3.

7.0 Future Work

The thermal stability and corrosion resistance will be explored for the manganese-substituted alloys. Fabrication of DBTT specimens of the ferritic alloys is now proceeding.

8.0 Publications

None.

CHAPTER 4

FUNDAMENTAL MECHANICAL BEHAVIOR

SUB-CRITICAL CRACK GROWTH IN HT-9

K.H. Jones (Pacific Northwest Laboratory)

1.0 Objective

Several recent studies have shown that internal or external cathodic^{2,3} hydrogen induces brittle, intergranular fracture of HT-9. These studies measured only the tensile ductility while fracture threshold and crack growth rate data are needed for identifying the embrittling mechanism and for critical flaw size determination. Therefore the purpose of this study was to measure the sub-critical crack growth of HT-9 in the presence of external cathodic hydrogen at 25°C. Future experiments will include crack-growth measurements in aqueous environments at 288°C.

2.0 Summary

Sub-critical crack growth measurements have been made on HT-9 at 25°C in a 1 N H₂SO₄ solution with the sample held at a cathodic potential of -600 mV (SCE). The tensile ductility of HT-9 was shown in a previous study² to be a minimum at -600 mV (SCE). The sub-critical crack growth behavior of HT-9 was similar for material in the tempered (760°C/2.5 hrs) or tempered + segregated (540°C/240 hrs) conditions. A rising load fracture threshold of 20 MPa \sqrt{m} and a decreasing load fracture threshold of 65 MPa \sqrt{m} was measured. A rising load fracture toughness of 110 \sqrt{m} was determined from extrapolation of the stage III crack growth curve. A ~~X~~ independent stage II was observed and a stage II crack growth rate of 0.5 to 1 x 10⁻⁵ mm/s was measured.

3.0 Program

Title: Mechanical Properties
Principal Investigator: R. H. Jones
Affiliation: Pacific Northwest Laboratory

4.0 Relevant UAFS Program Plan Task/Subtask

Task II.C.2 Effects of Helium and Displacements on Fracture
Task II.C.9 Effects of Hydrogen on Fracture
Task II.C.12 Effects of Cycling on Flow and Fracture

5.0 Accomplishments and Status

5.1 Background

Ferritic stainless steels are being considered for structural applications in fusion reactors where hydrogen embrittlement and stress corrosion may occur. Since the integrity of the plasma chamber and structural components is an important factor in fusion reactor design, potential material degradation processes are of great concern. Segregation of impurity elements such as phosphorus and sulfur have been shown to have an effect on the hydrogen embrittlement and intergranular corrosion of ferritic steels^{4,5} and it is known that phosphorus and sulfur Segregation can occur during heat treatment, fabrication and service above 450°C. Therefore, the effects of impurity segregation on the hydrogen embrittlement and stress corrosion of ferritic stainless steels are being determined as a part of their evaluation for fusion reactor structural applications.

In a previous study¹, the effect of heat treatment on grain boundary chemistry, hydrogen embrittlement and stress corrosion were evaluated. It was found in this previous study that the grain boundary phosphorus and sulfur concentrations of HT-9 depend on heat treatment in a manner consistent with other ferritic steels. After a tempering treatment of 25 hrs at 760°C the grain boundary phosphorus and sulfur concentrations were 0.015 and 0.03 monolayers, respectively while after a heat treatment of 240 hrs at 540°C their grain boundary concentrations were 0.04 and 0.01 monolayers, respectively. Straining electrode tests at cathodic and anodic test potentials revealed that HT-9 is sensitive to hydrogen embrittlement but not stress corrosion at 25°C in an acidic electrolyte. The reduction of area was 13% at cathodic test potentials and 60% in air and at anodic test potentials. This decrease in reduction of area was accompanied by an increase in quasi-cleavage and intergranular fracture.

5.2 Experimental Procedure

5.2.1 Material

Samples for straining electrode tests were taken from a piece of 13 mm thick plate of the fusion AOD heat (No. 9607) of HT-9 received from General Atomics. The chemical composition of this material as reported by General Atomics is given in Table 1. From this table it can be seen that this heat of HT-9 has 325 at. ppm phosphorus and 123 at. ppm sulfur which are both sufficient quantities to produce grain boundary segregation. Grain boundary chemistry analysis and straining electrode tests were performed on material given the following heat treatments:

- 1) 1040°C for 30 min, air-cooled + 760°C for 2-1/2 hr, air-cooled
- 2) Same as 1 + 240 hr at 540°C.

TABLE 1
CHEMICAL COMPOSITION OF FUSION AOD PROCESSED HT-9, (HEAT NO. 9607) WT. FRACTION

| | | | | | | |
|----------|-----------|-----------|----------|-----------|-----------|-----------|
| <u>C</u> | <u>Si</u> | <u>Mn</u> | <u>P</u> | <u>S</u> | <u>Cr</u> | <u>Mo</u> |
| 0.20 | 0.24 | 0.57 | 0.018 | 0.007 | 11.64 | 1.01 |
| | <u>Ni</u> | <u>V</u> | <u>W</u> | <u>Fe</u> | | |
| | 0.52 | 0.30 | 0.57 | Bal. | | |

A detailed description of the grain boundary chemistry analysis methods and results were published previously²⁻³ so that only a summary is given here. As seen in Table 2, both phosphorus and sulfur segregation was observed although the concentrations were low. The grain boundary phosphorus concentration was low after heat treatment at 760°C and increased with heat treatment at 540°C while the sulfur concentration behaved in an opposite manner to phosphorus. It was also shown in the previous study that the grain boundary phosphorus concentration was distributed from 0 to 15% after heat treatment at 540°C while the grain boundary sulfur concentration was distributed from 0 to 10% of a monolayer after heat treatment at 760°C. Therefore, it was concluded that the average grain boundary concentrations do not reflect the potential effect of impurity segregation on the hydrogen embrittlement of HT-9.

TABLE 2
GRAIN BOUNDARY CHEMISTRY OF HT-9

| <u>Treatment</u> | <u>P</u> | <u>S</u> | <u>Mo</u> | <u>Cr</u> | <u>C</u> | <u>O</u> |
|------------------|----------|----------|-----------|-----------|----------|----------|
| 760°C/2.5 h | 0.015 | 0.03 | 0.02 | 0.53 | 0.14 | 0.16 |
| 760°C/2.5 h | 0.04 | 0.01 | 0.03 | 0.73 | 0.14 | 0.10 |
| 540°C/240 h | | | | | | |

5.2.2 Sub-critical Crack Growth

Compact tension (CT) fracture samples were prepared from the heat treated sample blanks with the following sample dimensions: W = 44.45 mm, B = 2.54 mm, and a = 19.1 mm. One to two mm long pre-cracks were produced

in the CT samples at a ΔK of $14 \text{ MPa} \sqrt{\text{m}}$ and a frequency of 10 Hz . Sub-critical crack growth rate measurements were made in an inverted load frame immersed in $1\text{N H}_2\text{SO}_4$ as shown in Figure 1. A three electrode corrosion cell was used to control the sample potential with the platinum electrode surrounding the uncracked ligament of the sample. The sample was lacquered except for a strip 6 mm wide by 25 mm long on each side of the sample. A saturated calomel reference electrode was isolated from the test solution but monitored the sample potential through a Luggin probe salt bridge with the tip $2\text{--}3 \text{ mm}$ from the pre-crack. The crack length was monitored with an LVDT COD gage with a sensitivity of $8 \times 10^{-5} \text{ mm}$ of opening and also with a telescope viewing the crack length on the sample surface. A ratio of crack length to COD opening of 1.4 was observed. Tests were conducted at constant load for the time interval needed to obtain the crack growth rate at the selected stress intensity. A Model 1120 Instron constant crosshead machine was used for these tests, in which a constant load was obtained by setting the voltage on the load cell. A variation of 2% from the selected load was possible using this procedure. Tests were conducted with increasing and decreasing K by adjusting the load to the desired K and holding the load constant for the time interval needed to obtain crack growth rate measurements. This time interval depended on the crack growth rate with the shortest time interval being about 200 s and the longest time interval being about $5 \times 10^4 \text{ s}$.

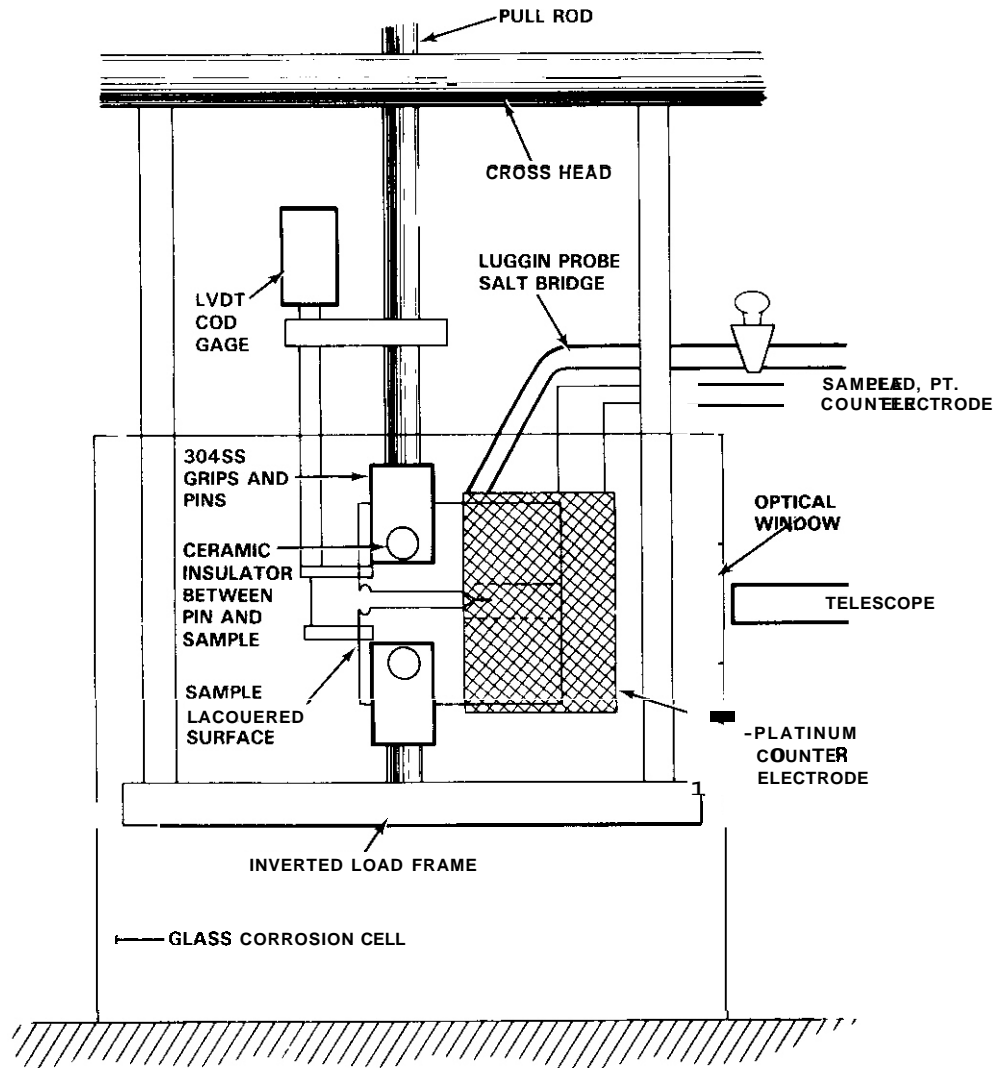


FIGURE 1. Schematic of Inverted Load Frame Apparatus

5.2.3 Stress Intensity Calculations

Kumar, German, and Shih' have recently presented an approach for estimating the elastic-plastic stress intensity for a variety of sample shapes. Their approach starts with the "corrected" linear elastic solutions and combines it with the fully plastic solutions to obtain an elastic-plastic J integral as follows:

$$J^{e-p} = J^e(a_e) + J^p(a, n), \quad (1)$$

where a_e is the effective elastic crack length

$$a_e = a + \phi r_p, \quad (2)$$

r_p is the strain hardening corrected plastic zone size expressed in Equation 3:

$$r_p = \frac{1}{2\pi} \left(\frac{K_I}{\sigma_y} \right)^2 \left(\frac{n-1}{n+1} \right) \quad (3)$$

$J^e(a_e)$ is determined from the following relationship:

$$J^e(a_e) = \frac{\sigma^2 \pi a_e \{F(a_e/b)\}^2}{E} \quad (4)$$

where a_e is determined from Equation 2 with ϕ determined from Equation 5 below:

$$\phi = 1/[1 + (P/P_0)^2] \quad (5)$$

$F(a_e/b)$ is merely the value $f(a/W)$ obtained from ASTM E399 divided by $\sqrt{\pi}$. J^p is determined from the following relationships:

$$J^p = a \sigma_y \epsilon_y (a/b) c h_1 (P/P_0)^{n+1} \quad (6)$$

$$P/P_0 = \sigma b / 1.07 \eta c \sigma_y \quad (7)$$

$$\eta = [1 + (a/c)^2]^{1/2} - a/c \quad (8)$$

The values for α and n are the coefficient and exponent in the Ramberg-Osgood flow relationship:

$$\epsilon/\epsilon_y = a (\sigma/\sigma_y)^n \quad (9)$$

Data for HT-9 straining electrode samples tested at -0.45 (corrosion potential), -0.6, and -1.0 V and in air are shown plotted as a function of $\log(\epsilon/\epsilon_y)$ versus $\log(\sigma/\sigma_y)$ in Figure 2. The values for α and n are given in the legend and it can be seen that the values are essentially independent of test condition. The results for the sample tested at -1.0 V (SCE) suggest that hydrogen may have increased the work hardening rate but the results at -0.6 V, -0.45 V and air are very similar. The sub-critical crack growth tests were conducted at -0.6 V; therefore, the average values for a and n were used to describe the stress-strain response of HT-9. Some of the parameters used in the above equations are defined below:

σ_y = yield strength = 510 MPa
 $\epsilon_y = \sigma_y/E = 2.5 \times 10^{-3}$
 a_0 = crack length (initial value) = 19.1×10^{-3} m
 b = sample width, $W = 44.45 \times 10^{-3}$ m
 $c = b - a$ (initial value) = 25.35×10^{-3} m
 $h_1 = 0.62$ for a CT sample (value obtained from Reference 7)
 σ = sample stress.

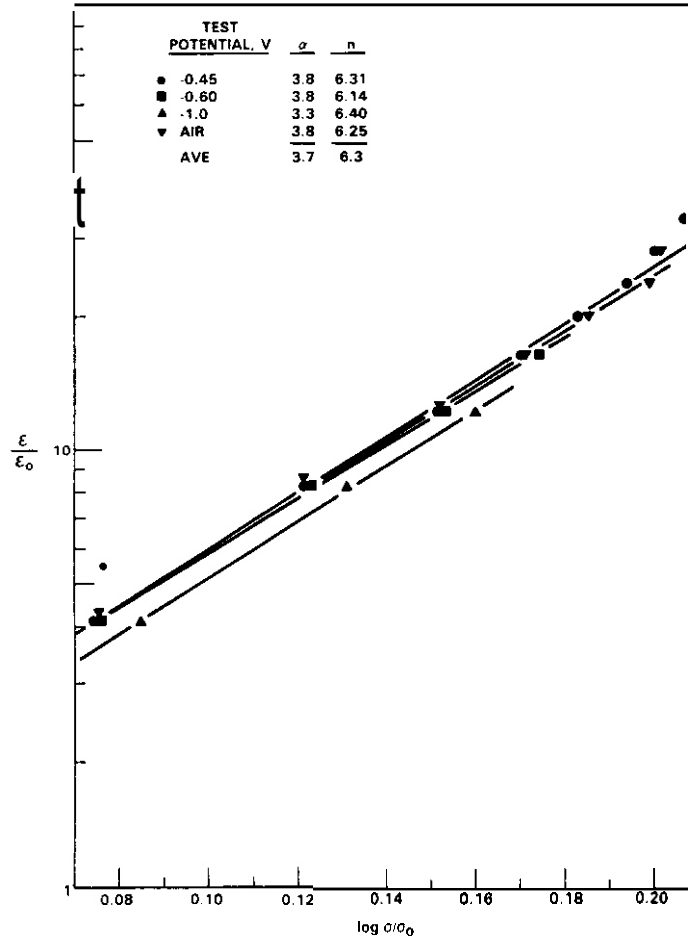


FIGURE 2. Log ϵ/ϵ_0 Versus Log σ/σ_0 for HT9 Tested in Air and Various Cathodic Potentials at 25°C in 1N H₂SO₄

J^{e-p} is obtained from Equation 1 and K^{e-p} from Equation 10,

$$K^{e-p} = \left\{ (K^e)^2 + (K^p)^2 \right\}^{1/2} \quad (10)$$

and the following relationship between J and K

$$K = \left\{ \frac{JE}{(1-\nu^2)} \right\}^{1/2} \quad (11)$$

Using the values given above Equation 4 reduces to Equation 4a and Equation 6 reduces to Equation 6a:

$$J^e = \frac{a^2}{207 \times 10^3 \text{ MPa}} \left\{ a_0 + \frac{0.116 (K_I)^2}{1 + 2.02} \right\} \left[f \left(\frac{a_e}{b} \right) \right]^2 \frac{N-m}{m^2} \quad (4a)$$

$$J^p = 3.1 \times 10^4 (1.423 \times 10^{-2} \sigma)^{7.3} \frac{N-m}{m^2} \quad (6a)$$

Values for K^e , K^p and K^{e-p} obtained with the equations and values above are listed in Table 3:

TABLE 3
STRESS INTENSITY VALUES FOR HT-9, MPa \sqrt{m}

| K_I ASTM | K^e | K^p | K^{e-p} | % DIFF $K_I - K^{e-p}$ | r_p , mm |
|---------------|-------|-------|-----------|---------------------------|------------|
| 30 | 35 | 0.33 | 35 | 16% | 0.4 |
| 60 | 77 | 37 | 77 | 29% | 1.6 |

where it can be seen that K^e and K^{e-p} are equal but there is a difference between the linear elastic stress intensity K_I , calculated using the ASTM approach and K^e using the Kumar, German and Shih approach. The ASTM value K_I was used to calculate the stress intensity since this method is widely accepted but it is possible that this value underestimates the stress intensity. The plastic zone calculated with Equation 3 is also given in Table 3. With a prior austenite grain size of 100 μm , the plastic zone size is 4 and 16 times larger than the grain size at K_I equal to 30 and 60 MPa \sqrt{m} , respectively. These plastic zone sizes indicate that HT-9 is not fully plastic in stage I and II but at a stress intensity of 60 MPa \sqrt{m} HT-9 is clearly in the elastic-plastic regime. Therefore, the linear elastic stress intensity values determined using the ASTM approach are probably lower than the actual value at the crack tip.

5.3 Experimental Results

Sub-critical crack growth rate versus stress intensity for HT-9 tested at -0.6 V (SCE) are given in Figures 3 and 4. Results are shown for 2 samples for the 540°C heat treatment with the resulting sub-critical crack growth behavior essentially independent of heat treatment. Both sets of data show a clear stage II (K-independent) and stage III while a clear stage I (threshold) was not clearly delineated. Since the data given in Figures 3 and 4 were obtained at constant load, the results are for a rising K condition since an increase in crack length increases the stress intensity. An estimate for the rising K threshold of 20 MPa \sqrt{m} was obtained from this data. A decreasing K threshold was also obtained by fixing the crosshead after loading the sample to the stage II-III region and allowing the load to decay to a minimum value. A decreasing K threshold of 70 MPa \sqrt{m} for a sample heat treated at 760°C and 60 MPa \sqrt{m} for a sample heat treated at 760°C + 540°C was obtained using this method. The appropriate use of these values will depend on the specific application and whether a component is in a constant load or constant deflection condition. Clearly a constant load situation is worse than a constant deflection situation.

A fracture toughness, K_{IC} , of about 110 MPa \sqrt{m} can be estimated by extrapolation of the stage III crack growth rate data. This value compares to a fracture toughness of 155 MPa \sqrt{m} estimated by Jones and Thomas³ for this steel from Charpy impact data. A lower fracture toughness is expected from the sub-critical crack growth data for the following reasons:

- the crack is growing and is therefore in a dynamic state,
- hydrogen has embrittled a volume of material ahead of the crack tip,
- the sub-critical crack is partially intergranular while the impact fracture was quasi-cleavage.

Therefore, a crack growing in a structure under the influence of hydrogen is more susceptible to overloads than a similar length, static flaw in the absence of hydrogen.

A stage II sub-critical crack growth rate of approximately 10^{-5} mm/s was determined from the results in Figures 3 and 4. Scatter in the data gives a range of 0.5 to 1.0×10^{-5} mm/s for the stage II crack growth rate with the results from samples heat treated at 760°C and 760°C + 540°C fitting this range.

A mixed transgranular-intergranular fracture mode resulted as shown in Figure 5 for a sample heat treated at 760°C + 540°C. The percent intergranular fracture is equivalent to that obtained with straining electrode samples at -0.6 V (SCE) as given by the straining electrode data in Figure 6.

5.4 Discussion

The absence of an effect of heat treatment on the sub-critical crack growth data is consistent with the straining electrode results shown in Figure 7. The sub-critical crack growth tests were conducted at the minimum in the total elongation and reduction of area - test potential results. Sub-critical crack growth

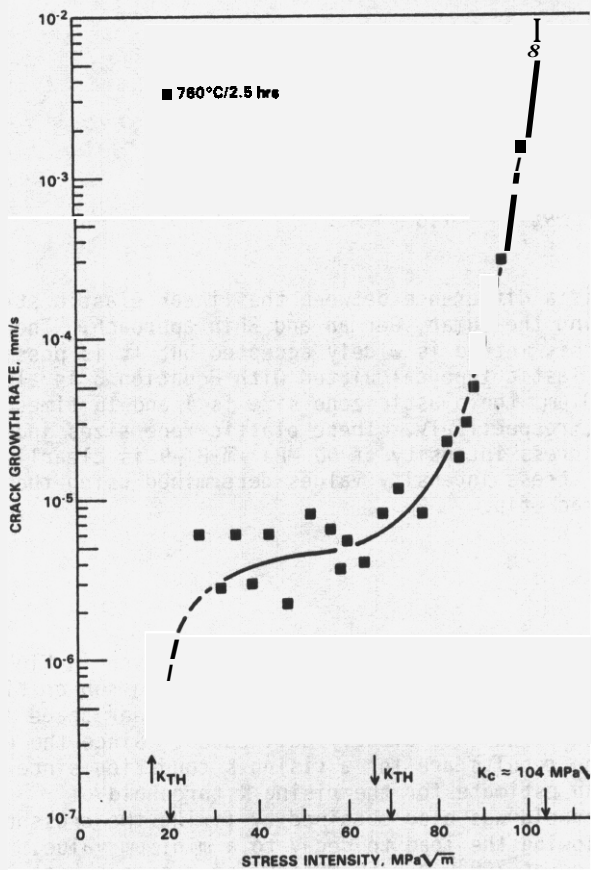


FIGURE 3. Crack Growth Rate Versus Stress Integrity for HT9 Heat Treated at 760°C/2.5 h and Tested in 1N H₂SO₄ at -0.6 V (SCE).

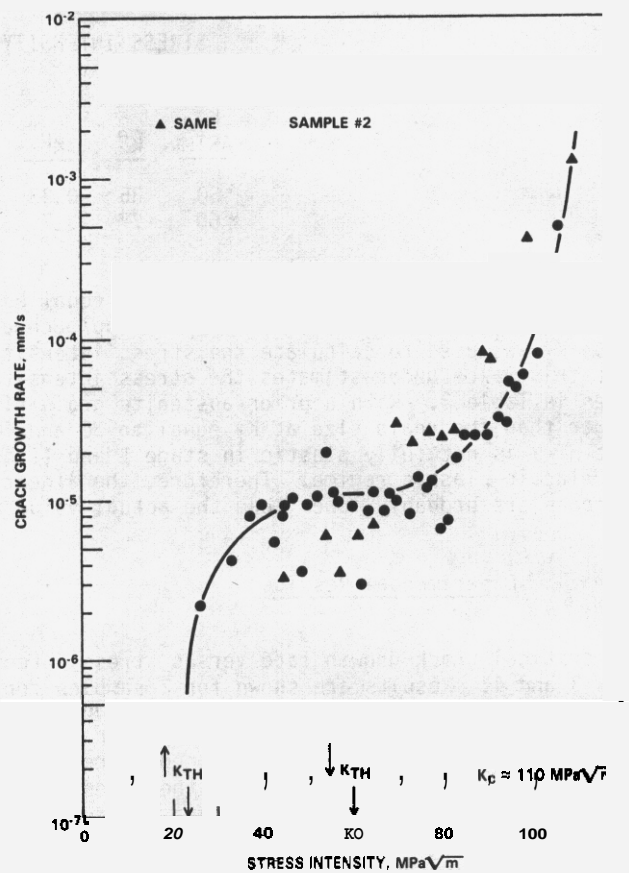


FIGURE 4. Crack Growth Rate Versus Stress Integrity for HT9 Heat Treated at 540°C/500 h and Tested in 1N H₂SO₄ at -0.6 V (SCE).

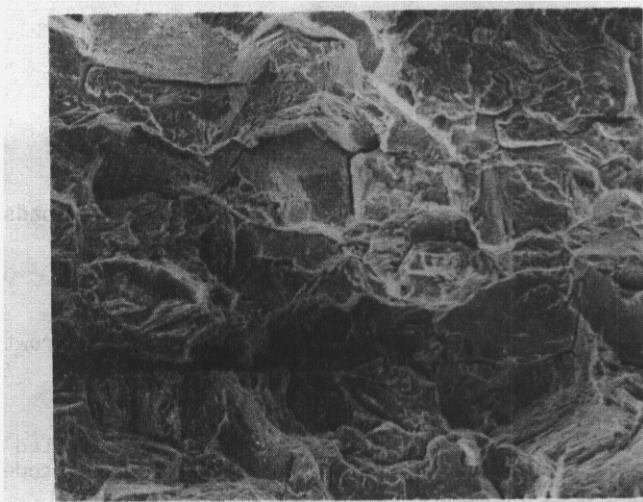


FIGURE 5. Scanning Electron Micrograph of a Fracture Surface from an HT9 Sample Heat Treated at 540°C/500 h and Tested in 1N H₂SO₄ at 25°C.

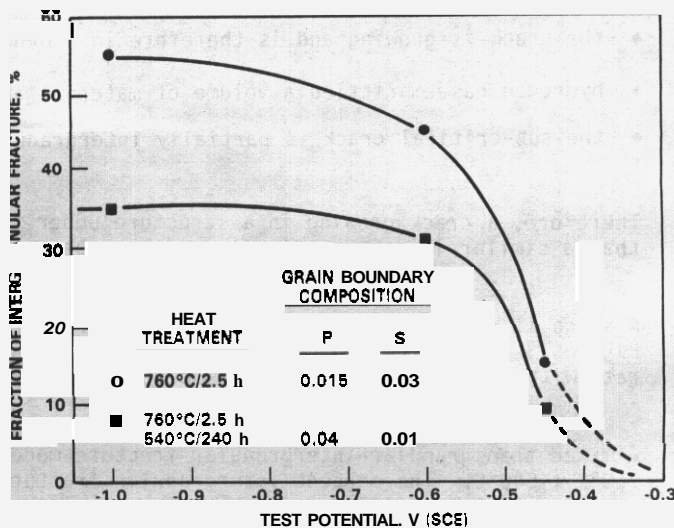


FIGURE 6. Percent Intergranular Fracture Versus Test Potential for HT9 Straining Electrode Samples Tested in 1N H₂SO₄ at 25°C.

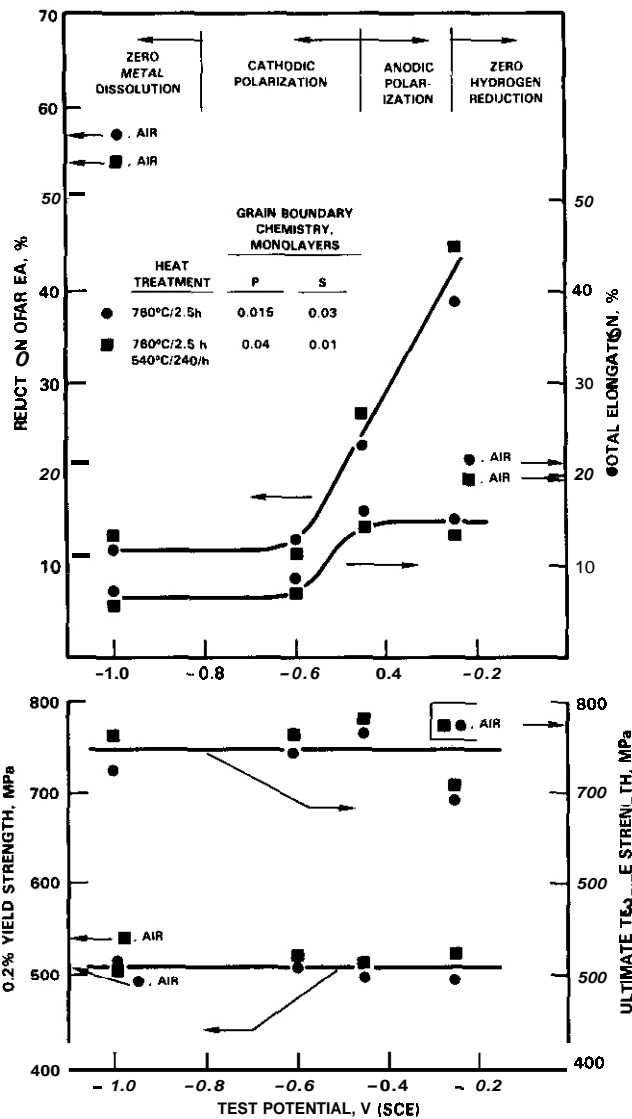


FIGURE 7. Straining Electrode Results for HT9 Tested in 1N H₂SO₄ at 25°C.

tests at less cathodic test potentials would be expected to result in higher fracture thresholds and possibly slower stage II crack growth rates. Jones et al. observed that the fracture threshold, K_{TH} , for intergranular sub-critical crack growth in iron was a function of the test potential. This observation was consistent with $K_{TH} \propto \log P_{H_2}$ observed for several steels in gaseous hydrogen. Therefore, a smaller hydrogen reduction rate at less cathodic potentials, corresponding to a smaller hydrogen pressure, would increase K_{TH} . Also, the smaller hydrogen pressure expected in a fusion reactor structure would be expected to produce higher K_{TH} values than measured in the present experiments. Determination of the hydrogen concentration in a fusion reactor structural material is not simple. The total hydrogen inventory from ions injected from the plasma, (n,p) reactions within the material and possibly from corrosion reactions from a water coolant must be considered.

Gerberich and Wright¹⁴ developed a model which relates the fracture threshold, K_{TH} , to the grain boundary impurity concentration and hydrogen concentration. This model was applied to HT-9 by Jones and Wolfer¹⁵ with the result shown in Figure 8. The calculated K_{TH} value is related to a decreasing K value which approximates an equilibrium threshold value. Using the average grain boundary phosphorus concentration, the calculated K_{TH} is $150 \text{ MPa} \sqrt{\text{m}}$ which is considerably larger than the measured value of $65 \text{ MPa} \sqrt{\text{m}}$. However, other than an error in the model of Gerberich and Wright there are two possible explanations for the lower observed K_{TH} . One explanation is that the hydrogen pressure and therefore the near surface quantity, C_D , is greater in the cathodic test than the value assumed by Gerberich and Wright. A second explanation is that the maximum grain boundary phosphorus concentration and not the average concentration controls the fracture threshold. This assumption is physically attractive since the fracture threshold is the stress intensity below which the crack growth rate is zero. Therefore, the fracture threshold for intergranular fracture

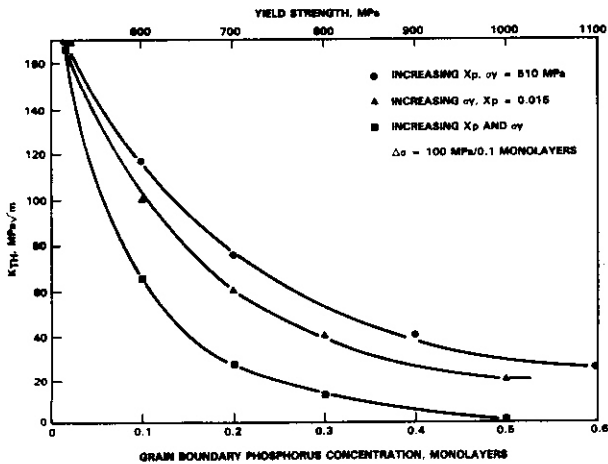


FIGURE 8. Calculated Sub-critical Crack Growth Threshold Versus Grain Boundary Phosphorus Concentration for HT9.

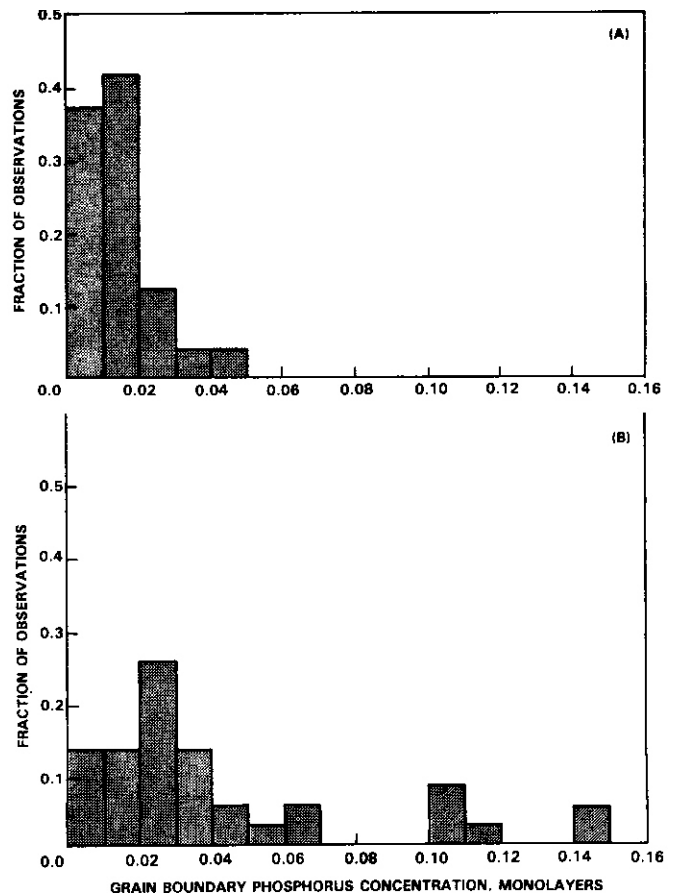


FIGURE 9. Grain Boundary Phosphorus Concentration Histograms for HT9.

must be the stress intensity below which the most probable grain boundary will not fracture. The probability that a grain boundary will fracture depends on its orientation to the stress, type of boundary, grain boundary chemistry and many other factors. Considering only the grain boundary chemistry, the maximum grain boundary phosphorus concentration was 15% of a monolayer, as shown by the histogram in Figure 9b. Using this value for the grain boundary phosphorus concentration in Figure 8 gives a calculated K_{TH} of 90 MPa√m. Therefore, the combination of a higher hydrogen concentration in the cathodic test and the fracture threshold being primarily controlled by the maximum grain boundary phosphorus concentration would give good agreement between the measured and calculated values for K_{TH} .

6.0 References

1. J. M. Hyzak and W. M. Garrison, Alloy Development for Irradiation Performance Semi-annual Progress Report for Period Ending March 31, 1982, DOE/ER-0045/8, 401 (1982).
2. R. H. Jones and M. T. Thomas, Damage Analysis and Fundamental Studies Quarterly Progress Report for Period Ending March 31, 1983, DOE/ER-0045/13, Vol. 1, p. 77.
3. R. H. Jones and M. T. Thomas, "Hydrogen Embrittlement of a 12 Cr-1 Mo Steel," in "Proceedings of the Topical Conference on "Ferritic Alloys for Use in Nuclear Energy Technologies", Snowbird Utah June 1983, TMS-AIME, Warrendale, PA.
4. R. H. Jones, S. M. Bruemmer, M. T. Thomas and D. R. Baer, Met. Trans, A, 12A, 1621 (1981).

5. J. Kameda and C. J. McMahon, Jr., Met. Trans. A, 12A, 31 (1981).
6. C. L. Briant, Scripta Met., 15, 1013 (1981).
7. V. Kumar, M. D. German and C. F. Shih, "An Engineering Approach for Elastic-Plastic Fracture Analysis," EPRI NP-1931, (1981).
8. R. H. Jones, M. T. Thomas and D. R. Baer, submitted to Met. Trans.
9. R. A. Oriani and P. H. Josephic, Acta Met., 22, 1065 (1974).
10. W. W. Gerberich, J. Garry and J. F. Lessar, in Effect of Hydrogen on Behavior of Materials, A. W. Thompson and I. M. Bernstein, eds., p. 70, TMS-AIME, Warrendale, Pennsylvania (1975).
11. R. A. Oriani and P. H. Josephic, Acta Met., 25, 979 (1977).
12. W. H. Clark and J. D. Landes, Stress Corrosion-New Approaches, p. 108, ASTM STP 610, American Society for Testing Materials, Philadelphia, Pennsylvania (1976).
13. K. Sieradzki, Scripta Met., 15, 171 (1981).
14. W. W. Gerberich and A. H. Wright, in: Proceedings of the Second International Conference on Environmental Degradation of Engineering Materials, eds. M. R. Louthan, Jr., R. P. McNitt and R. D. Sisson Jr., Virginia Polytechnic Institute, Blacksburg, VA, 1981 p. 183.
15. R. H. Jones and W. G. Wolfer, in Proceedings of the Third Fusion Reactor Materials Meeting, Albuquerque, NM, August 1983.

7.0 Future Work

Sub-critical crack growth rate tests will be conducted at several cathodic potentials for the purpose of evaluating the dependence of K_{TH} and da/dt on hydrogen pressure. Also, further modeling of the effect of hydrogen on the intergranular crack growth rate will be completed. A scoping experiment to measure the stress corrosion threshold of HT-9 and 316 SS in water at 288°C will be completed.

CRITICAL LEAK RATE FLAW SIZES FOR WATER OR LITHIUM-COOLED FUSION REACTORS

R.H. Jones (Pacific Northwest Laboratory)

1.0 Objective

The purpose of this evaluation was to extend a previous¹ analysis of critical leak rate flaw size for a helium cooled reactor to a water or liquid lithium cooled reactor. As in the previous report, the critical leak rate flaw sizes are compared to threshold flaw sizes for fatigue or environmentally induced sub-critical crack growth and to flaw sizes for unstable flaw growth.

2.0 Summary

The results of this analysis indicate that the critical leak rate flaw size for water and lithium is about 1 mm and 1500 mm respectively for an elastically loaded crack and about 0.04 mm and 12 mm, respectively, for a crack which has opened by creep. By comparison, the critical leak rate flaw size for helium which was reported previously¹ is 12 mm for an elastically loaded crack and 0.04 mm for a crack opened by creep. The threshold flaw sizes for fatigue and corrosion fatigue sub-critical crack growth of 316 SS and HT-9 range from 0.2 to 2 mm and the flaw sizes for unstable crack growth of irradiated 316 SS and HT-9 are 4 mm and 50 mm, respectively. These results suggest that the critical leak rate flaw size for helium and water are the smallest flaws which may affect reactor performance and that the threshold for sub-critical crack growth in fatigue is a critical material property. Also, creep processes are shown to have a significant effect on the critical leak rate flaw size.

3.0 Program

Title: Mechanical Properties
Principal Investigator: R. H. Jones
Affiliation: Pacific Northwest Laboratory

4.0 Relevant OAFS Program Plan Task/Subtask

Task II.C.8. Effects of Helium and Displacement on Fracture
Task II.C.9. Effects of Hydrogen on Fracture
Task II.C.12. Effects of Cycling on Flow and Fracture

5.0 Accomplishments and Status

5.1 Background

The lifetime of fusion reactor first wall materials will be a function of many factors such as load, temperature and neutron irradiation history, and plasma-wall and coolant-wall interactions. Fatigue crack growth has been identified by Cramer et al.² as the primary structural failure mode for Tokamak first walls. More recently, Watson et al.³ evaluated the effect of irradiation creep, swelling, wall erosion and embrittlement on the fatigue life of a Tokamak first wall made of 316 SS. They concluded that fatigue crack growth is the life-limiting process in Tokamak reactors and that the shortest lifetime occurs when a flaw exists on the coolant side. Embrittlement induced by neutron irradiation and surface erosion were predicted to decrease the lifetime by increasing the crack propagation rate.

A fusion reactor-vacuum first wall may lose its vacuum integrity before losing its structural integrity by allowing coolant to leak into the plasma. A leak before break criterion has been assessed for 20% CW 316 SS by Wolfer and Jones⁴ and the results show that unstable flaw growth is favored as the stress and wall thickness increases and the critical stress intensity, K_{IC} , decreases. A leak producing flaw was defined as any through wall flaw which was too small for unstable crack growth. In a separate study, Jones and Bruemmer⁵ concluded that a 0.1 mm wide through wall flaw in a helium cooled reactor would allow the helium concentration in the plasma to reach 50% in a 1000s period. Since first wall thicknesses are expected to be greater than 1 mm, a through wall flaw with a width to length ratio of 1/10 would be sufficient to shut down a reactor. Flaws of this dimension may be present in the as-fabricated first wall or may grow to this dimension during reactor operation. Flaws of this size will be difficult to locate by non-destructive testing, NDT, techniques in a non-radioactive structure and even more difficult once the reactor has been operating and the first wall and blanket structure are radioactive. Since detection of flaws becomes more difficult with decreasing flaw size it is important to know the smallest critical flaw so that NDT evaluation can be limited to flaws greater than or equal to the critical size.

Analysis of whether a flaw will merely cause a leak or will grow in an unstable manner causing a break is an important aspect of any critical flaw size analysis. Factors which decrease K_{IC} or increase the yield strength, σ_y , will decrease the flaw size for unstable crack growth and hence favor a break before leak failure. Temper, hydrogen and helium embrittlement, radiation induced grain boundary segregation and phase changes are processes which can decrease K_{IC} while radiation induced hardening can increase the yield strength.

Sub-critical crack growth can occur in corrosive or hydrogen environments during static or dynamic loading conditions. Static load sub-critical crack growth is commonly called stress corrosion cracking while dynamic load sub-critical crack growth is known as corrosion fatigue. A threshold stress intensity exists below which measureable crack growth cannot be detected in corrosive environments. At static loads, this threshold is called the K_{ISCC} while at dynamic loads, this threshold is called the ΔK_{ISCC} . A critical flaw size can be derived from these threshold stress intensities which defines the flaw size which will propagate under a given environment and loading condition. Knowledge of the size of the threshold flaw sizes in corrosion fatigue or stress corrosion is important because they may define the smallest flaw size. Environmentally critical flaws do not present as immediate a problem for reactor operation as a leak or break; however, the environmentally enhanced crack growth rate may be sufficiently high that a leak or a break will form in a relatively short time.

The purpose of this research was to determine and compare the critical flaw sizes of fusion reactor materials. These results will be useful for focusing attention on the physical processes controlling the lifetime of fusion reactors with the expectation that systems can be designed which are insensitive to the presence of flaws smaller than those which can be readily detected with NDT techniques or the need for better data to define the critical flaw sizes. Critical flaw sizes for unstable crack growth, stress corrosion, corrosion fatigue and hydrogen embrittlement for 316 SS and HT-9 are compared to the critical leak rate flaw size for helium, water and lithium coolants.

5.2 Critical Leak Rate Flaw Sizes for Water and Lithium

The leak rate process and equations for this analysis were discussed previously¹ such that only the methodology and results for the water and liquid lithium results are presented.

The approach used for water and lithium leak rates differed from that used for helium since they are in the liquid state on the coolant side. It was assumed that water or lithium leakage through a small orifice occurs by gas phase transport and that the water vapor or lithium gas pressure at the input side of the orifice is equal to the vapor pressure at the temperature of interest. Water was assumed to be at a temperature of 288°C which is consistent with present day light water reactors and that lithium was at 500°C. There is a possibility that water or lithium would partially or completely penetrate a through wall flaw and that evaporation or boiling would occur at temperatures greater than the coolant temperature. Since the extent of liquid penetration is unknown, it was assumed that water and lithium leakage occurs by gas transport which originated on the coolant side of the flaw.

The vapor pressure of water at 288°C is 5.4×10^4 torr⁶ while the vapor pressure for lithium at 500°C is 3×10^{-3} torr. Only the leak rate for pure lithium was considered although lithium-lead and other mixtures are being considered as coolants. A temperature of 500°C was chosen for lithium to give a comparison to helium at the same temperature. At a pressure of 5.4×10^4 torr (5.4×10^7 μm), water vapor would have a $\delta P = 16,000$ for a crack with a cross-section of $a(1) = 0.17$ cm and $b = 3 \times 10^{-4}$ cm and a $\delta P = 65,000$ for a crack with a cross-section of $a = 0.003$ cm and $b = 1.2 \times 10^{-3}$ cm. At a coolant pressure of 50 atm (3.8×10^7 μm)

helium would also have δP values considerably greater than 500 for similar crack dimensions. Therefore, water vapor at 288°C and helium at 500°C would be in the viscous flow regime. Lithium gas at 500°C, however, would flow through small cracks by a molecular flow process since a flaw with a cross-section as large as 8.5 $\mu\text{m} \times 1.7 \mu\text{m}$ would have a $\delta P \sim 5$.

Using the equation for viscous flow presented previously for the leak rate of water and molecular flow for lithium and the vapor pressures given above, the leak rate versus flaw size relationships for water and lithium given in Figures 1 and 2, respectively were derived. For comparison, the helium leak rate versus flaw size relation is given in Figure 3. It should be noted that experimental verification of the calculated water and lithium leak rates through small cracks are not carried out as it was for helium; therefore, the accuracy of the water and lithium leak rate flaw sizes is unknown. However, based on the data in Figures 1 and 3 the critical leak rate flaw sizes for water are very comparable to those for helium. For instance, the critical flaw size for a 1% water concentration in a UWMAK II reactor is 0.067 μm in the absence of creep and 0.003 μm with creep crack opening. These values compare to 0.08 μm and 0.003 μm for critical helium leak rate flaws.

The small vapor pressure of lithium at 500°C results in large critical flaw sizes. For a 1% lithium concentration in a UWMAK II, the critical leak rate flaw size is 150 μm in the absence of creep and 7 μm with creep. These flaw sizes are unrealistic since it is very likely that some other failure mechanism will supersede the failure of a first wall by lithium leakage into the plasma.

5.3 Flaw Size Comparison

Comparison of the critical leak rate flaw size for 1%He, H₂O or Li in the plasma and sub-critical and critical flaw sizes in austenitic and ferritic stainless steels is given in Table 1 and 2.

The following conclusions can be made regarding critical flaws in austenitic stainless steels: 1) a helium cooled reactor will be shut-down because of a critical leak before a large break in the first wall and 2) fatigue stresses will cause sub-critical flaw growth at lower stresses or for shorter flaws than static stresses. Fatigue or corrosion fatigue will cause growth of sub-critical flaws to a size where they become a critical leak rate flaw while static stresses require flaws that are larger than the critical leak rate flaw size. This comparison demonstrates the desirability of a steady state fusion reactor which minimizes cyclic stresses in the blanket and first wall material over a pulsed fusion reactor in which the stresses and temperatures will cycle.

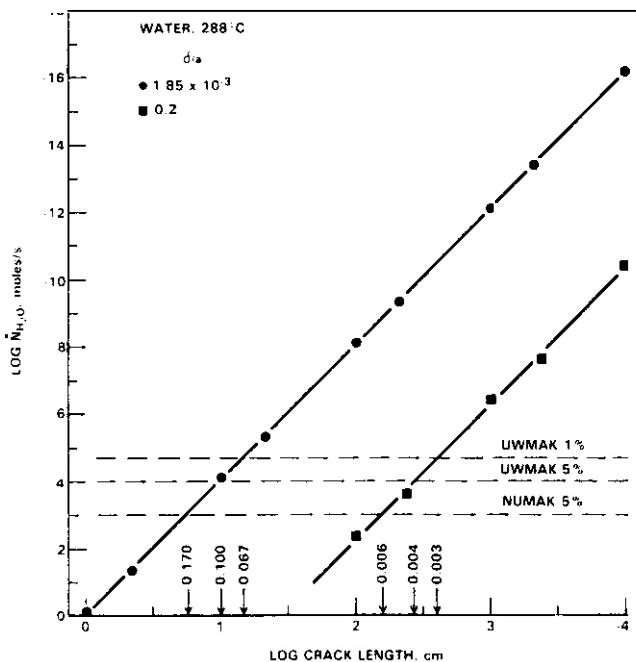


FIGURE 1. Crack Length, a, Versus Leak Rate for a Water-Cooled Fusion Reactor.

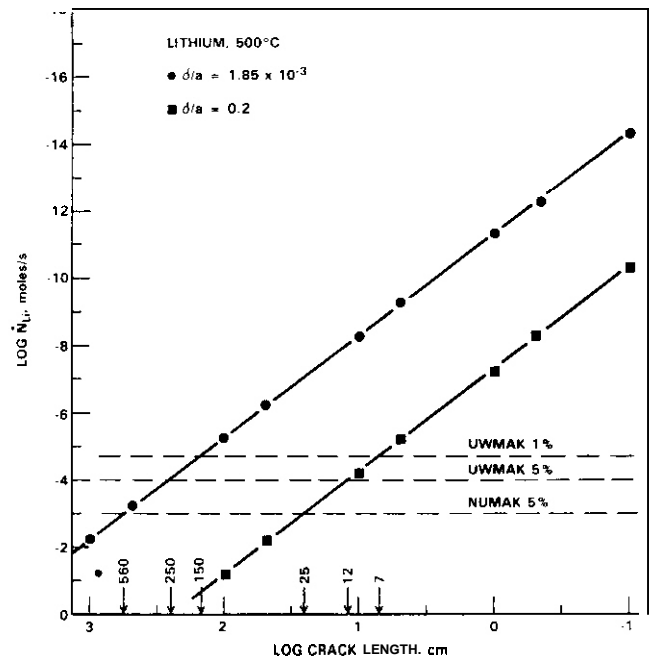


FIGURE 2. Crack Length, a, Versus Leak Rate for a Liquid Lithium-Cooled Fusion Reactor.

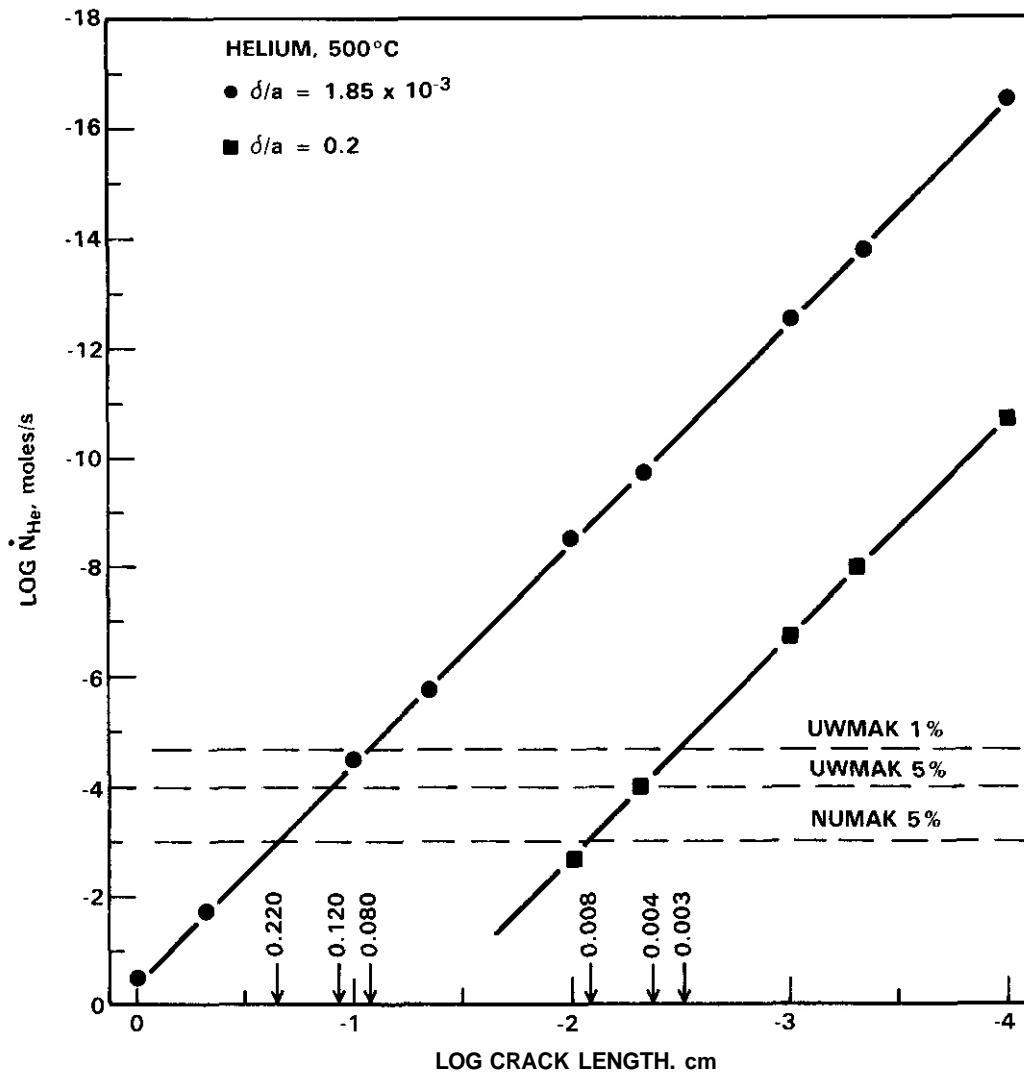


FIGURE 3. Crack Length, a , Versus Leak Rate for a Helium-Coated Fusion Reactor,

The flaw size comparison given in Table 1 is useful for showing the kind of test data needed to evaluate materials for fusion reactors. A list of test data needed to evaluate austenitic stainless steels for fusion reactor applications is listed below along with the reason this data is needed:

- fracture toughness of 316 SS (25°C-450°C) irradiated at the fusion Helipa: helium is known to embrittle 316 SS and will therefore reduce the critical flaw size. Welded test samples should be included in this series.
- fatigue and/or corrosion fatigue (300-500°C) of 316 SS irradiated at the fusion Helipa: this test and material condition will probably define the smallest critical flaw size. Welded test samples should be included in this series.
- creep crack opening rate since the critical flaw size (length) is 20X smaller for He and H₂O and 200X for Li for a flaw opened by creep than an elastically loaded crack.

TABLE 1
CRITICAL FLAW SIZES IN AUSTENITIC STAINLESS STEELS

| Failure Criterion | Conditions | Stress, MPa | Critical Stress Intensity MPa $\sqrt{\text{m}}$ | Critical Flaw Size, mm | Ref. |
|--------------------------------|--|--------------------------|---|---|------|
| Coolant Leak Rate | Coolant leakage into plasma chamber during 1000s burn | Elastically Loaded Crack | --- | 1% He: 0.8 1% H ₂ O: 0.7 1% Li: 1500 | --- |
| | | Crack Opened by Creep | | 1% He: 0.03 1% H ₂ O: 0.03 1% Li: 7 | |
| Unstable Flaw Growth | 20% CW 316 SS, 400°C Unirradiated | 550 | 110 | 10 | 3 |
| | Irradiated, 10 ²³ cm ⁻² fast neutrons, 400°C | 550 | 70 | 4 | 3 |
| Fatigue Crack Growth | 20% CW, 316 SS Unirradiated 550°C, vacuum | 550 | 12 | 0.1 | 9 |
| Corrosion Fatigue Crack Growth | Sensitized 304 SS Unirradiated, 95°C, Argon | 200 | 11 | 0.8 | 10 |
| | Sensitized 304 SS 95°C, H ₂ O/1.5 ppm O ₂ | 200 | 6 | 0.2 | 10 |
| Stress Corrosion Crack Growth | Sensitized 304 SS 95°C, H ₂ O/1.5 ppm O ₂ | 200 | 15 | 1.4 | 10 |
| | Sensitized 304 SS 228°C, H ₂ O/1.0 ppm O ₂ | 200 | 17 | 1.8 | 11 |

Ferritic stainless steels show similar trends to austenitic stainless steels in that fatigue stresses produce sub-critical crack growth with the smallest flaw size. Ferritic stainless steels appear to be more sensitive to stress corrosion than austenitic stainless steels where the critical flaw size for sub-critical crack growth in water at 25°C is 0.2 mm. Ferritic stainless steels can be embrittled by grain boundary impurity segregation (temper embrittlement) resulting in a critical flaw size of 1 mm in a 12 Cr steel at 25°C. The critical flaw size for temper embrittlement, hydrogen embrittlement and stress corrosion cracking of ferritic steels will presumably be greater at reactor service temperatures than at 25°C unless the ductile to brittle transition temperature, DBTT, is shifted to the reactor service temperatures by radiation hardening and helium. Smidt¹⁰ has measured the fracture properties of HT-9 irradiated to 10²² cm⁻² and his results indicate that the critical flaw size was reduced from 95 mm to 50 mm. It is possible that the critical flaw size of HT-9 irradiated to higher fluences at a fusion He/dpa will be less than 50 mm; however, this data is not presently available.

As in austenitic stainless steels, the critical helium leak rate flaw size is similar in size to that for sub-critical crack growth during fatigue and less than the critical flaw size for unstable flaw growth. However, the flaw size for unstable flaw growth of temper embrittled HT-9 is only 5X greater than a critical leak rate flaw size while the smallest flaw size for unstable flaw growth of austenitic stainless steel was 20X greater than the critical leak rate flaw size. Therefore, the transition between leak before break in ferritic stainless steels may be less than for austenitic stainless steels. This situation changes if temper embrittlement does not occur in ferritic stainless steels and if irradiation to fluences greater than 10²² cm⁻² does not significantly decrease the critical flaw size for unstable flaw growth.

The data in Table 2 indicates the need for more data which is relevant to the fusion reactor environment. A list of test data needed to evaluate ferritic stainless steels for fusion reactor applications is listed below along with the reason this data is needed:

- fracture toughness (25°C-450°C) of HT-9 irradiated to fluences of $>10^{23} \text{ cm}^{-2}$ at the fusion Heldpa: radiation hardening and helium will raise the DBTT and decrease the upper shelf fracture toughness.
- fatigue, stress corrosion or corrosion fatigue tests (300-500°C) of HT-9 irradiated to fluences of $>10^{23} \text{ cm}^{-2}$ at the fusion Heldpa: fatigue, stress corrosion and corrosion fatigue tests of irradiated material will define the smallest critical flaw size.
- fatigue, stress corrosion or corrosion fatigue tests (300-500°C) of temper embrittled and irradiated HT-9: HT-9 temper embrittled by improper thermal-mechanical treatment (such as during welding, heat treatment or fabrication) prior to irradiation could conceivably produce the smallest critical flaw size and would therefore represent the worst case.
- creep crack opening rate of HT-9. The lower creep rate of HT-9 relative to 316 SS should result in HT-9 having a larger critical leak rate flaw size than 316 SS. However, the extent of creep crack opening in HT-9 needs analysis since any creep opening will decrease the critical leak rate flaw size relative to an elastically loaded crack.

TABLE 2
CRITICAL FLAW SIZES IN FERRITIC STAINLESS STEELS

| Failure Criterion | Conditions | Stress, MPa | Critical Stress Intensity MPa $\sqrt{\text{m}}$ | Critical Flaw Size, mm | Ref. |
|-------------------------------|---|--------------------------|---|--|------|
| Coolant Leak Rate | Coolant leakage into plasma chamber during 1000s burn | Elastically Loaded Crack | -- | 1% He: 0.8 1% H ₂ O: 0.7 1% H ₂ : 1500 | --- |
| | | Crack Opened by Creep | | 1% He: 0.03 1% H ₂ O: 0.03 1% H ₂ : 7 | |
| Unstable Flaw Growth | HT-9 Unirradiated 427°C | 450 | 275 | 95 | 8 |
| | HT-9 Irradiated 10^{22} cm^{-2} , 427°C | 450 | 200 | 50 | 8 |
| | 12 Cr Steel, Temper embrittled 25°C | 650 | 40 | 1 | 12 |
| | HT-9, Hydrogen embrittled, 25°C | 650 | 75 | 3 (calc) | 13 |
| Fatigue Crack Growth | HT-9 Unirradiated 150°C-600°C | 450 | 8 | 0.1 | 14 |
| Stress Corrosion Crack Growth | 12 Cr steel, 25°C water | 650 | 20 | 0.2 | 12 |

6U References

1. R. H. Jones, "Critical Flaws in Fusion Reactor Materials," Damage Analysis and Fundamental Studies Quarterly Report for Period Ending March, 1982, DOE/ER-0046/9.
2. B. Cramer et al., Fusion Reactor First Wall/Blanket Systems Analysis, Interim Report, MDAC/EPRI 472-1, Oct. 1977.
3. R. D. Watson, R. R. Peterson and W. G. Wolfer, "The Effect of Irradiation Creep, Swelling, Wall Erosion and Embrittlement on the Fatigue Life of a Tokamak First Wall" in Proceedings of the Second Meeting on Fusion Reactor Materials, Aug. 1981.
4. W. G. Wolfer and R. H. Jones, "Flow and Fracture of Alloys in the Fusion Environment" in the Proceedings of the Second Meeting on Fusion Reactor Materials, Aug. 1981, J. Nucl. Mater., 103 and 104 (1981) 1305.
5. R. H. Jones and S. M. Bruemmer, Damage Analysis and Fundamental Studies Quarterly Report for Oct.-Dec. 1980, DOE/ER-0046/4, p. 65.
6. CPC Handbook of Chemistry and Physics, R. C. Weast and M. J. Astle, eds., CRC Press, West Palm Beach, Florida, 1979, p. D233.
7. T. B. Douglas et al., "Lithium: Heat Content from 0 to 900°, Triple Point and Heat of Fusion, and Thermodynamics Properties of the Solid and Liquid," J. Am. Chem. Soc. 77(8), 2144-2150 (1955).
8. F. A. Smidt, J. Hawthorne, and V. Provenzano, Alloy Development for Irradiation Performance, Quarterly Report, DOE/ER-0045/2, p. 163.
9. D. J. Michel and H. H. Smith, "Environmental Effects on Elevated Temperature Fatigue Crack Propagation in Type 316 SS for Fusion Reactor Applications," in Environmental Oeyradation of Engineering Materials, Virginia Polytechnic Institute, Sept. 1981, p. 313.
10. F. P. Ford and M. Silverman, Corrosion, Vol. 36, No. 11, (1980), p. 597
11. R. D. Caligiuri, "Low Temperature Sensitization of Weld Heat Affected Zones in 304 SS," in proceedings of EPRI International Workshop on Low Temperature Sensitization, Paper No. 4, January 1982, Palo Alto, CA.
12. M. O. Speidel, "Corrosion Fatigue in Fe-Cr-Ni Alloys," in Stress Corrosion Cracking and Hydrogen Embrittlement of Iron Base Alloys, Conference held at Unieux-Firminy, France, June 1973, R. W. Staehle, J. Hochmann, R. D. McCright and J. E. Slater, eds., NACE-5, p. 1071.
13. J. M. Hyzak and R. E. Stoltz, Alloy Development of Irradiation Performance Quarterly Report, DOE/ER-0045/3, p. 180.
14. D. A. Mervyn, Alloy Development for Irradiation Performance Quarterly Report, DOE/ER-0045/3, p. 226.

7.0 Future Work

Further work on leak rate analysis is not currently planned but experiinental leak rate-flaw size measurements are needed for water and liquid lithium. Further work in modeling and measuring the sub-critical crack growth behavior of 316 SS and HT-9 is planned.

CHAPTER 5

CORRELATION METHODOLOGY

SWELLING OF Fe-Ni-Cr TERNARY ALLOYS AT HIGH EXPOSURE

F. A. Garner and H. R. Brager (Hanford Engineering Development Laboratory)

1.0 Objective

The objective of this effort is to determine the origins of the composition and temperature dependence of swelling in simple austenitic alloys.

2.0 Summary

Acquisition of higher fluence data (70-110 dpa) on the swelling of austenitic Fe-Ni-Cr ternary alloys confirms the conclusion drawn earlier that the eventual swelling rate of all austenitic Fe-Ni-Cr alloys in EBR-II is $\sim 1\%/dpa$ in the range 400-650°C. The influence of composition and temperature lies only in the duration of the transient regime of swelling. At temperatures below 500°C, saturation of swelling appears to be occurring, often at very high swelling levels. The saturation level decreases with decreasing temperature, increasing nickel level and decreasing chromium content.

3.0 Program

Title: Irradiation Effects Analysis (AKJ)
Principal Investigator: O. G. Doran
Affiliation: Hanford Engineering Development Laboratory

4.0 Relevant OAFS Plan Task/Subtask

Task I.C.1 Effects of Material Parameters on Microstructure
Task II.C.16 Composite Correlation Models and Experiments

5.0 Accomplishments and Status

5.1 Introduction

In earlier reports it was shown that the influence of both composition and temperature on the swelling of austenitic Fe-Ni-Cr ternary alloys in EBR-II lay primarily in the duration of the transient regime of swelling. It was further stated that the eventual swelling rate of all austenitic Fe-Ni-Cr alloys was $\sim 1\%/dpa$ over a surprisingly large range of temperature. While this latter conclusion was amply demonstrated for alloys with relatively low (12.4%) nickel levels and relatively high (>15% chromium) levels, some doubt could still be expressed concerning the eventual swelling rate for alloys with higher nickel and lower chromium levels. The transients of these alloys were still in progress at the last report, particularly for the higher irradiation temperatures.

Additional density change measurements at higher fluence have now been made, concentrating particularly on the higher nickel range and the higher temperatures. The new data (beyond that listed in Reference 1) are listed in Table 1. Except where noted each measurement is the average swelling of two identical specimens irradiated side-by-side. When the swelling varied more than 0.2% between members of the pair, the two values are reported separately.

TABLE 1

ADDITIONAL SWELLING DATA FOR Fe-Ni-Cr ALLOYS*

| Alloy | Temperature (°C) | $\phi t/10^{22}$ n/cm ² (E > 0.1 MeV) | Swelling (%) |
|-------------------------------|---------------------|---|-----------------|
| Alloy E18 Fe-12.1Ni-15.1Cr | 427 | 18.5 | 49.5 |
| | 650 | 21.9 | 31.1 |
| Alloy E90 Fe-15.7Ni-15.6Cr | 427 | 18.5 | 52.6 |
| | 593 | 22.0 | 53.7 |
| | 650 | 21.9 | 21.2 |
| Alloy E39 Fe-20.3Ni-7.5Cr | 538 | 20.4 | 20.2 |
| | 593 | 22.0 | 3.19 |
| | 650 | 21.9 | 2.14 |
| Alloy E26 Fe-20.1Ni-11.8Cr | 538 | 20.4 | 47.8 |
| | 593 | 22.0 | 20.9, 23.0** |
| | 650 | 21.9 | 5.40 |
| Alloy E19 Fe-19.4Ni-14.9Cr | 593 | 22.0 | 46.3, 49.1** |
| | 650 | 21.9 | 13.2 |
| Alloy E27 Fe-24.7Ni-10.2Cr | 538 | 20.4 | 9.45 |
| | 593 | 22.0 | 3.06 |
| | 650 | 21.9 | 1.74 |
| Alloy E20 Fe-24.4Ni-14.9Cr | 538 | 20.4 | 66.1 |
| | 593 | 22.0 | 16.0 |
| | 650 | 21.9 | 6.48 |
| Alloy E21 Fe-29.6Ni-15.3Cr | 538 | 20.4 | 47.3 |
| | 593 | 22.0 | 7.38 |
| | 650 | 21.9 | 5.35 |
| Alloy E37 Fe-35.5Ni-7.5Cr | 400 | 15.1 | 1.71 |
| | 454 | 13.4 | 1.89 |
| | 482 | 17.4 | 0.95 |
| | 650 | 21.9 | 0.31 |
| Alloy E22 Fe-34.5Ni-15.1Cr | 400 | 15.1 | 16.2 |
| | 427 | 18.5 | 21.9 |
| | 482 | 17.4 | 20.8 |
| | 538 | 20.4 | 10.3 |
| | 593 | 22.0 | 2.90 |
| | 650 | 21.9 | 4.42 |
| Alloy E38 Fe-35.2Ni-20.0Cr | 427 | 18.5 | 38.0 |
| | 482 | 17.4 | 44.8 |
| | 538 | 20.4 | 61.1 |
| | 593 | 22.0 | 16.4 |
| | 650 | 21.9 | 17.0 |
| Alloy E25 Fe-35.1Ni-21.7Cr | 427 | 18.5 | 33.2 |
| | 482 | 17.4 | 60.7 |
| | 538 | 20.4 | 66.6 |
| | 593 | 22.0 | 54.2, 50.1** |
| | 650 | 21.9 | 23.7 |
| Alloy E23 Fe-45.3Ni-15.0Cr | 400 | 15.1 | 2.38 |
| | 427 | 18.5 | 8.19 |
| | 482 | 17.4 | 9.42 |
| | 538 | 20.4 | 5.26 |
| | 593 | 22.0 | 1.09 |
| 650 | 21.9 | 4.96 | |
| Alloy E24 Fe-75.1Ni-14.6Cr | 400 | 15.1 | 2.49 |
| | 427 | 18.5 | 9.03 |
| | 510 | 21.0 | 21.1 |
| | 538 | 20.4 | 18.7 |
| | 593 | 22.0 | 4.13, 2.37** |
| | 650 | 21.9 | 31.0 |

*These data are in addition to those published in Reference 1.

**Each of these two nominally identical specimens exhibited a different swelling, while all other specimen pairs exhibited identical swelling within $\pm 0.2\%$.

5.2 Results and Discussion

Figure 1a shows a subset of the data published in Reference 1 and demonstrates that over a range of 12.1 to 24.4 wt% nickel and chromium levels of 7.5 to 15.6%, there is surprisingly little sensitivity of swelling to both composition and temperature for temperatures between 400 and 510°C. There are no data below 400°C. Figure 2 shows the increasing impact of temperature above 510°C on the duration of the transient regime for these alloys.

Note that Figure 1b shows that the seven alloys listed in Figure 1 inhabit one end of the experimental matrix. At higher nickel levels the influence of temperature is observed much sooner, as demonstrated in Figure 3a. Increasing the chromium level or decreasing the nickel level tends to postpone the effect of temperature somewhat, as shown in Figures 3b and 3c. Figures 4 and 5 show that increases in chromium level at a given temperature and nickel level tend to shorten the duration of the transient regime of swelling. The influence of nickel, however, is exactly the opposite of that of chromium, as shown in Figures 6a, 6b, and 6c.

It is important to note that the swelling rate of all curves shown thus far tends to increase with fluence and eventually approach $\sim 1\%/dpa$. Swelling levels in the range of 50-70% are often shown in the preceding curves, confirming our previous conclusion that saturation of swelling will not occur at engineering-relevant levels in the Fe-Ni-Cr system,

The minimum in ion-induced swelling in the alloy series at 35-45% nickel (observed by Johnston and coworkers)⁷ obviously arises from a maximum in the duration of the transient regime in this composition range, particularly at higher temperatures, as can be seen in Figure 6. Figure 7 shows that the rate of change of swelling with nickel content is asymmetrical about the minimum, however, with the high nickel side in general increasing at a slower rate than that of the low nickel side. This observation is also in agreement with the observations of Johnston.

One of the most striking features of Figures 3 through 6 is the lack of saturation. This conclusion may be somewhat misleading, however, and possibly reflects the fact that most of the new data were obtained at the higher nickel levels and higher irradiation temperatures. There is one set of reasonably complete high-fluence data at 427°C, however. As shown in Figure 8 it appears that saturation may be setting in at this temperature.

If saturation is sensitive to void surface area or void sink strength one would expect the saturation level to decline at lower temperatures due to the strong temperature dependence of void nucleation. A limited set of data at 400°C (Figure 9b) tends to confirm this conclusion and some data at higher temperatures (Figure 9a) suggests that this principle may be operating.

Note that at 427°C the level of saturation is inversely proportional to the duration of the transient. Whenever two curves have the same transient duration, their saturation levels are such that the lowest level occurs in the alloy whose void nucleation rate would be expected to be the largest based on compositional differences (i.e., lower nickel or higher chromium).

5.3 Conclusions

At temperatures between 400 and 650°C the eventual swelling rate of austenitic Fe-Cr-Ni alloys appears to be $\sim 1\%/dpa$, with all influence of temperature, nickel and chromium level lying in the duration of the transient regime of swelling. The influence of nickel is opposite that of chromium and exhibits an **asymmetrical** minimum at ~ 35 to 45% nickel. Saturation also appears to be occurring at the lower irradiation temperatures, reaching levels which are dependent on the composition as well as the temperature.

6.0 References

1. F. A. Garner, "Dependence of Swelling on Nickel and Chromium Content in Fe-Ni-Cr Ternary Alloys," DAFS Quarterly Progress Report, DOE/ER-0046/14, August 1983, p. 133.
2. H. R. Brager and F. A. Garner, "Swelling of High Nickel Fe-Ni-Cr Alloys in EBR-II," OAFS Quarterly Progress Report, DOE/ER-0046/14, August 1983, p. 152.
3. H. R. Brager and F. A. Garner, "Radiation-Induced Evolution of Fe-Ni-Cr Ternary Alloys," OAFS Quarterly Progress Report, DOE/ER-0046/12, February 1983, p. 170.
4. H. R. Brager and F. A. Garner, "Microsegregation Induced in Fe-35.5Ni-7.5Cr by Irradiation in EBR-II," DAFS Quarterly Progress Report, DOE/ER-0046-14, August 1983, p. 120.

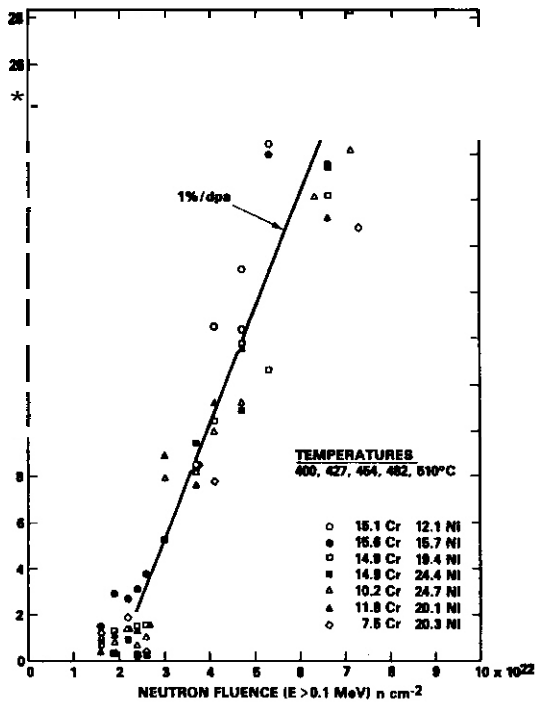


FIGURE 1a. Swelling of Seven Fe-Ni-Cr Alloys at Five Temperatures in the Temperature Range 400-510°C.¹

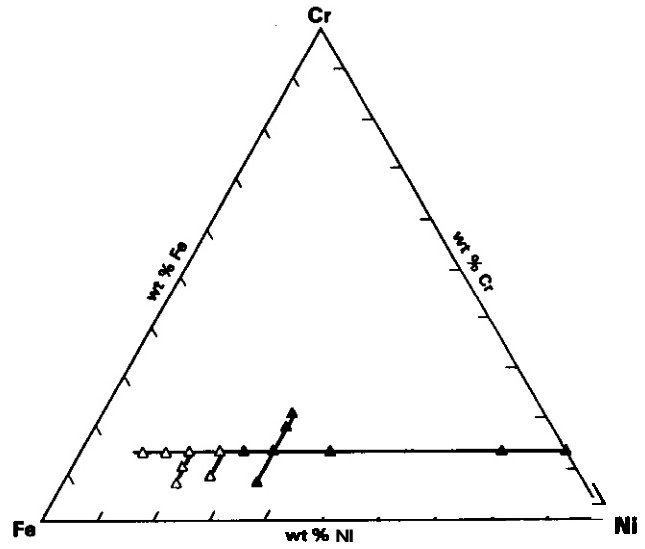


FIGURE 1b. Fe-Ni-Cr Ternary Diagram Showing Matrix of Alloys Used in This Experiment. The open symbols are the alloys whose swelling is shown in Figure 1a.

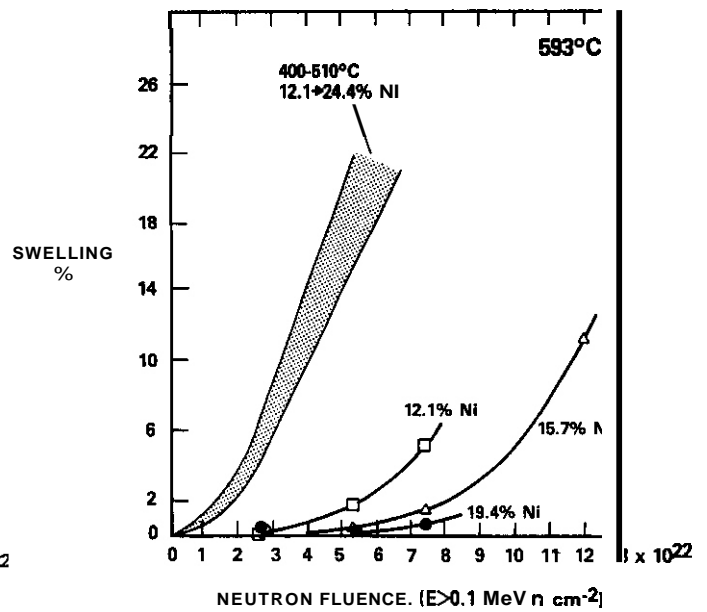
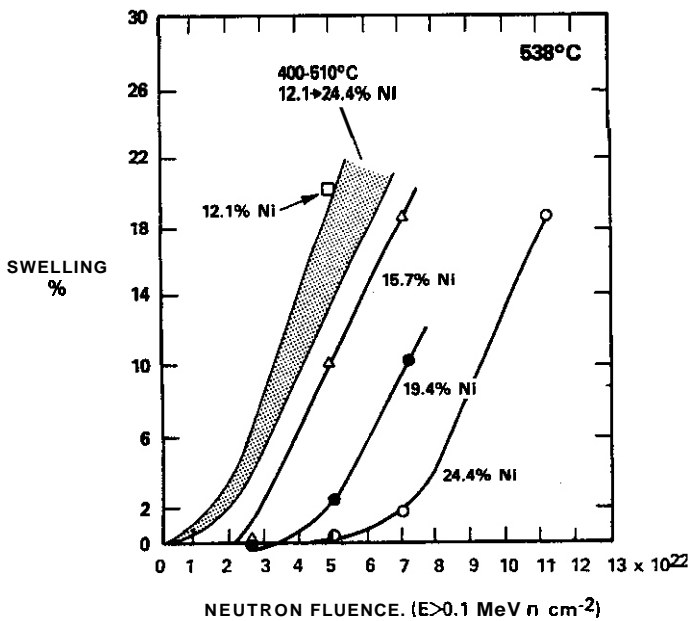


FIGURE 2. Effect of Temperature and Nickel Content of Fe-15Cr-XNi Alloys at Temperatures Above 510°C.³ In this and subsequent figures, a 1%/dpa ($\sim 5\%/10^{22}$ n/cm²) line is shown for comparison.

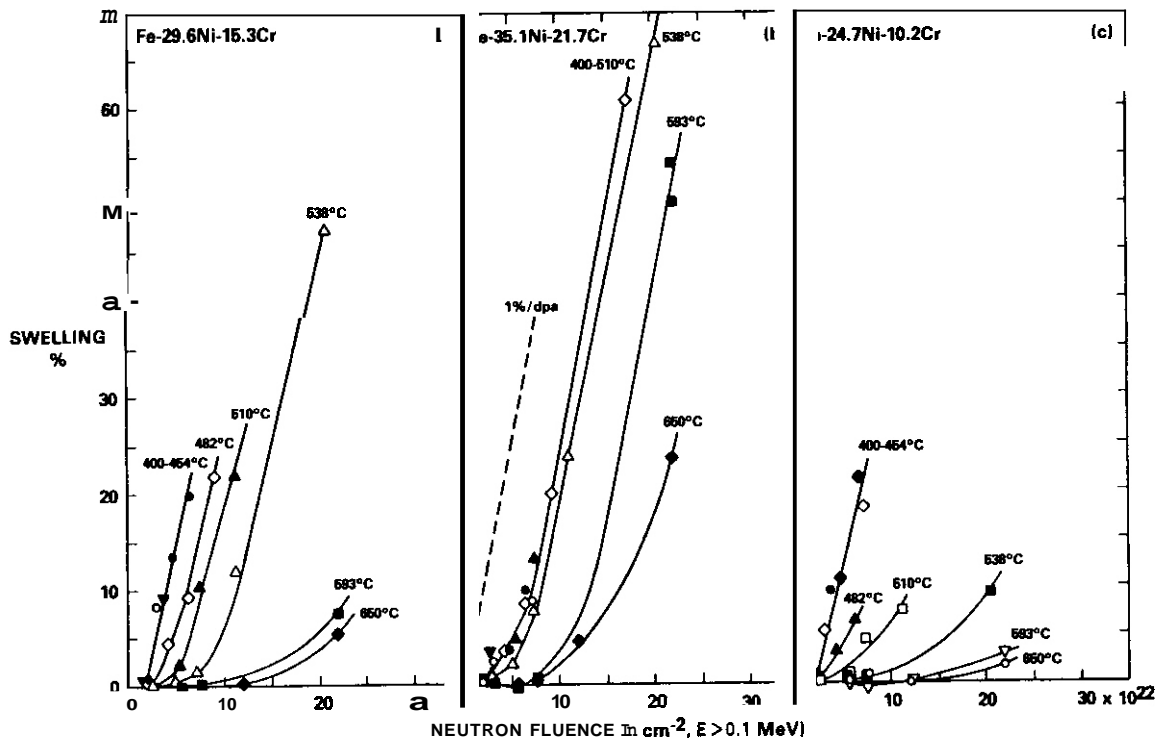


FIGURE 3. Temperature Dependence of Swelling in Three Alloys with High Nickel Levels and Different Chromium Contents.

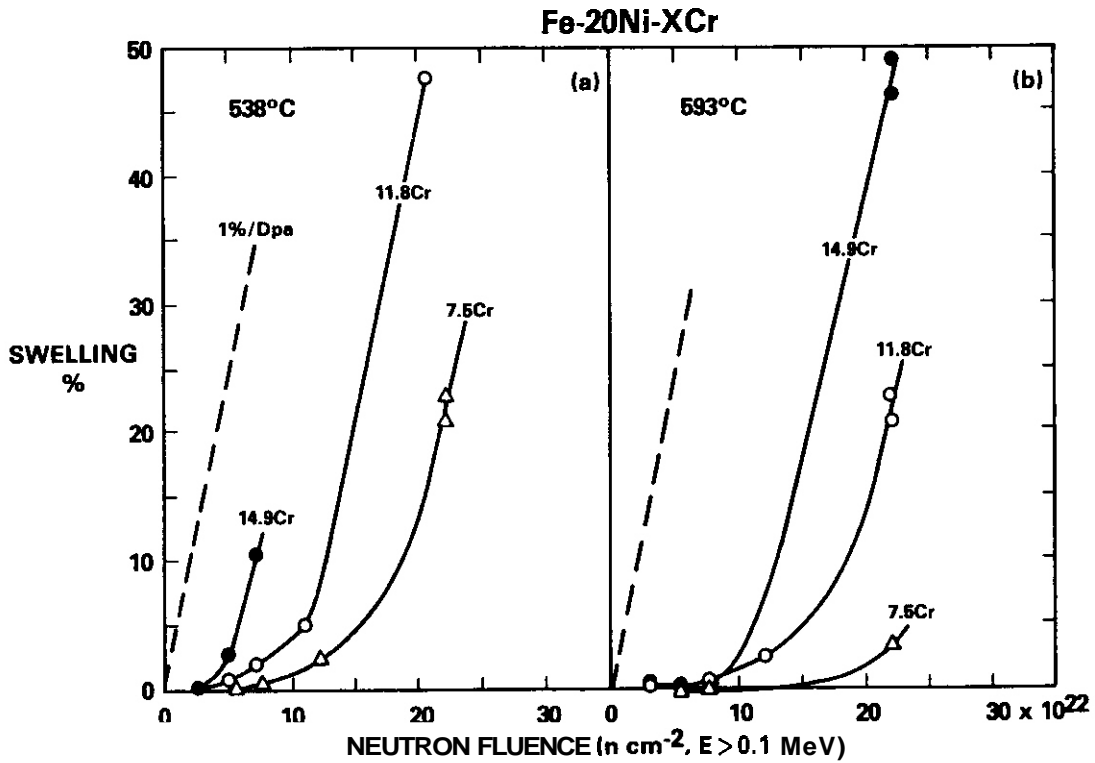


FIGURE 4. Influence of Chromium Level and Temperature on the Swelling of Fe-20Ni-XCr in EBR-II.

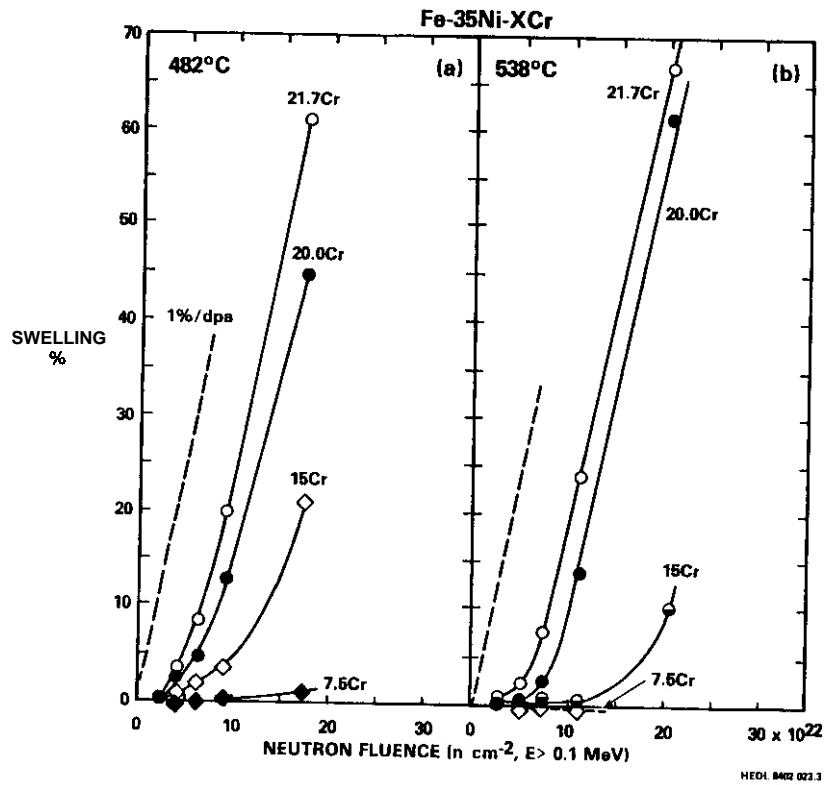


FIGURE 5. Influence of Chromium Level and Temperature on the Swelling of Fe-35Ni-XCr in EBR-II.

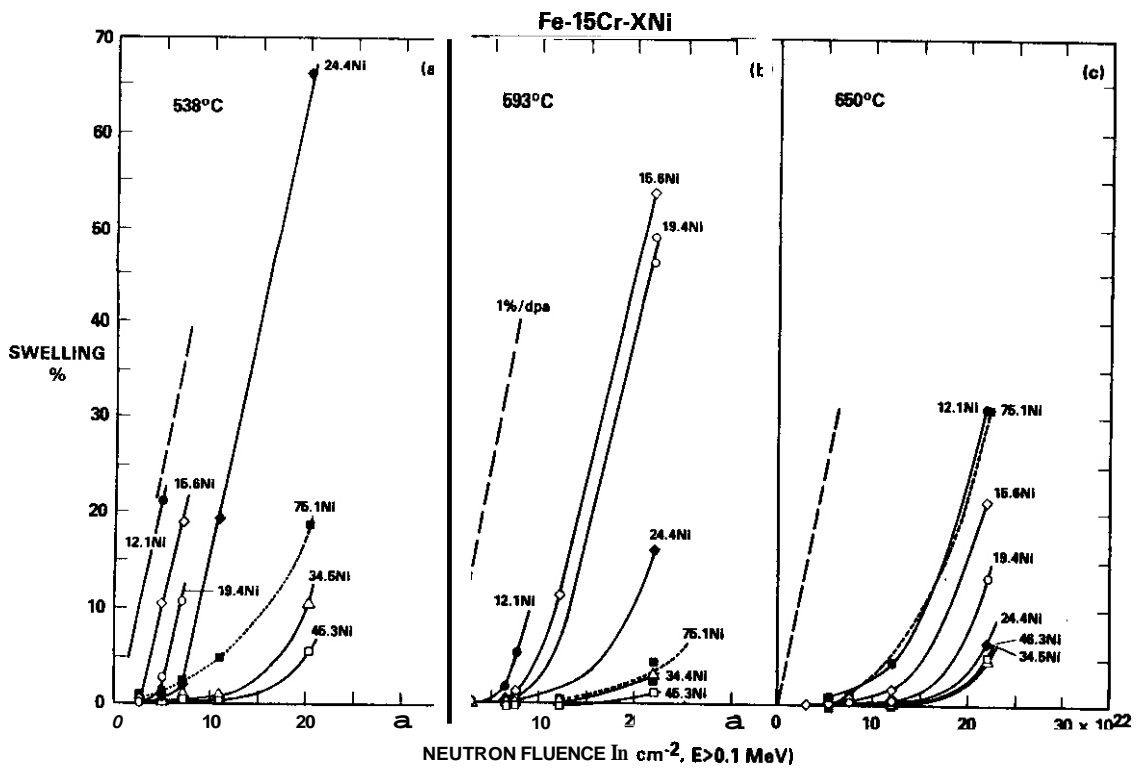


FIGURE 6. Influence of Nickel Level and Temperature on the Swelling of Fe-15Ni-XCr in EBR-II.

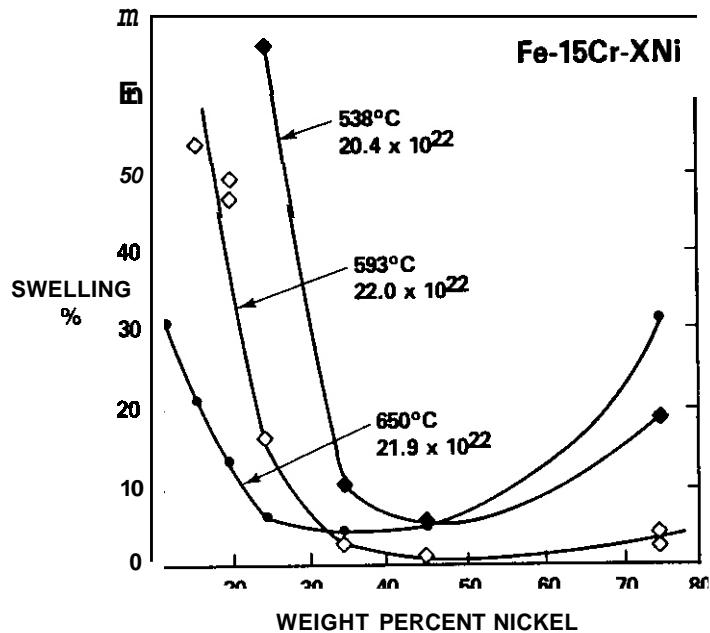


FIGURE 7. Dependence of Swelling on Temperature, Neutron Fluence and Nickel Content in Fe-15Cr-XNi.

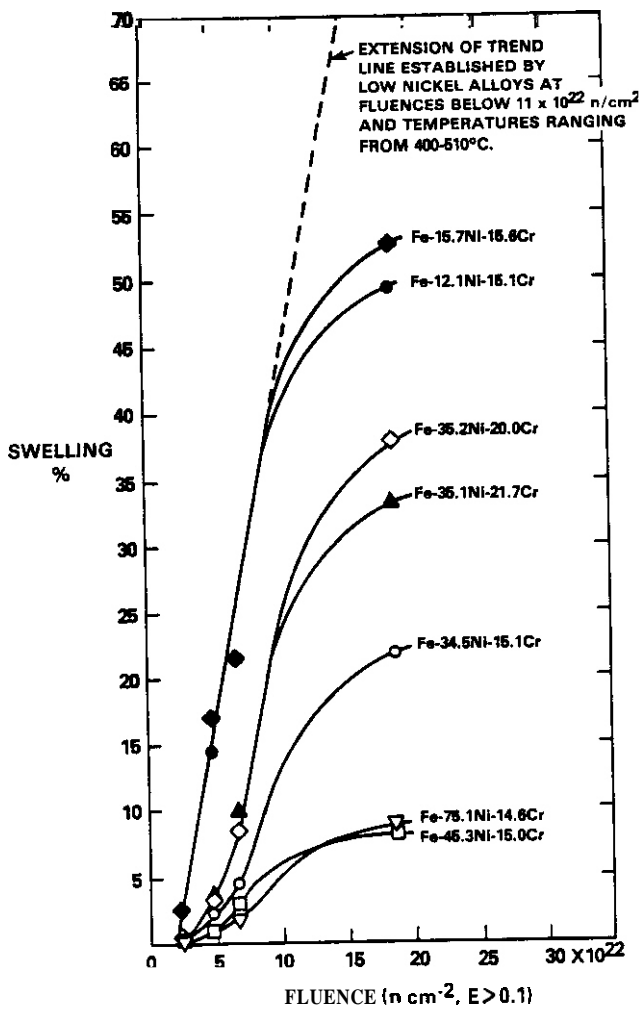


FIGURE 8. Apparent Saturation of Swelling Occurring in Fe-Ni-Cr Alloys Irradiated at 427°C.

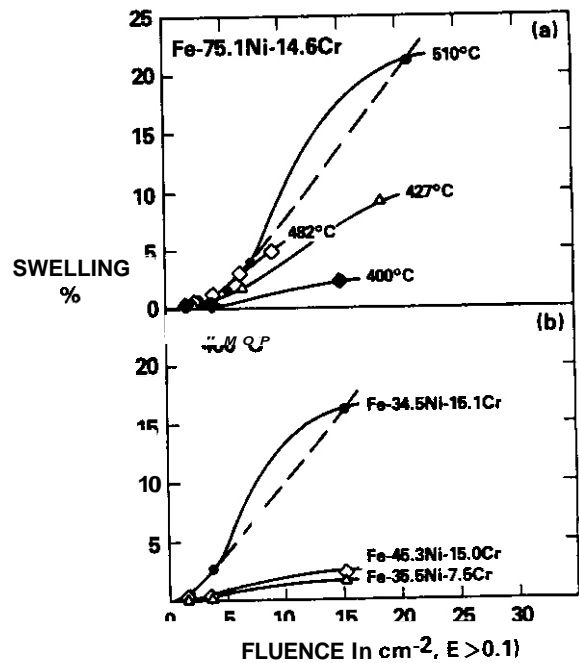


FIGURE 9a. Swelling Behavior Observed in Fe-75.1Ni-14.6Cr.
 b. Swelling of Various Fe-Ni-Cr Alloys at 400°C.

5. F. A. Garner, "Recent Insights on the Swelling and Creep of Irradiated Austenitic Alloys," DAFS Quarterly Progress Report, DOE/ER-0046-16, February 1984, p. 49.
6. H. R. Brager and F. A. Garner, "Dependence of Swelling of Fe-Ni-Cr Alloys on Chromium and Nickel Content," DAFS Quarterly Progress Report, DOE/ER-0046/11, November 1982, pp. 221-231.
7. W. G. Johnston et al., "The Effect of Metallurgical Variables on Void Swelling," Radiation Damage in Metals, N. L. Peterson and S. D. Harkness, Eds., Am. Soc. of Metals, 1976, pp. 227-266.

7.0 Future Work

A void nucleation model is almost completed which explains the major features of the temperature and compositional dependence of swelling in this alloy series. The microstructural development of these alloys is also being examined to determine whether the evolution of loop and dislocation microstructure is sensitive to composition.

8.0 Publications

Reference 5 will be published in the proceedings of the Third Topical Meeting on Fusion Reactor Materials (Albuquerque, NM, September 1983). Reference 1 and References 3 and 4 will form the basis of two papers to be presented in the TMS-AIME symposium on Tailoring and Optimizing Materials for Nuclear Applications (Los Angeles, CA, February 1984).

TRANSMUTATION OF MANGANESE-SUBSTITUTED STEELS IN STARFIRE

H. L. Heinisch and F. A. Garner (Hanford Engineering Development Laboratory)

1.0 Objective

The object of this study is to determine whether the transmutation reactions occurring in a fusion environment will seriously alter the phase stability of the fundamental alloy series employed to study the impact of manganese substitution for nickel in iron-based austenitic alloys.

2.0 Summary

The transmutations calculated for the STARFIRE wall employing the manganese substitution alloys currently under investigation in the DAFS program are not expected to greatly change the phase stability of these alloys.

3.0 Program

Title: Irradiation Effects Analysis (AKJ)
Principal Investigator: D. G. Doran
Affiliation: Hanford Engineering Development Laboratory

4.0 Relevant DAFS Plan Task/Subtask

Task II.C.4 Effects of Solid Transmutants on Microstructure

5.0 Accomplishments and Status

5.1 Introduction

It has been proposed that austenitic alloys based on the Fe-Mn-Cr system might offer significant advantage over the Fe-Ni-Cr system for fusion service with respect to activation. Thus, a series of Fe-Mn-Cr based alloys has been prepared for testing in the DAFS program. It is known that in an irradiation environment with a large component of thermal neutrons, such as HFIR, the transmutation of manganese to iron changes the alloy composition, resulting in a loss of austenitic stability. In fast reactor neutron spectra, such as the FFTF or EBR-II core locations, manganese burnout is much less than in HFIR and does not affect the phase stability of the Fe-Mn-Cr alloys.

In general, the compositional balance between iron and manganese depends on the transmutation and decay of one to the other. There are a variety of important reactions $[(n,p), (n,2n), (n,\gamma)]$, so that radiation-induced changes in the manganese-iron balance depend on the shape of the neutron spectrum. As a prerequisite for the study of the Fe-Mn-Cr alloys for applications in fusion reactors, it was necessary to determine if loss of phase stability due to transmutation might be a problem in typical first-wall spectra. This consideration has been addressed using the REAC code system, which is described in Reference 2. This code calculates both transmutation and activation using libraries of cross sections and decay data based largely on the ENDF/B-V libraries.

For this study the neutron spectrum and flux were assumed to be those of the first-wall portion of the STARFIRE reactor, which has a relatively large low-energy neutron component for a fusion reactor because of the water-cooled blanket design. In this environment, austenitic steels receive about 40 dpa per year. The alloy compositions were determined for continuous irradiation times of 1, 2, 5 and 10 years. The three

alloys chosen for investigation are shown in Table 1; they span the range of interest of Fe/Mn ratios. They also include representative solute-free and solute-modified alloys.

5.3 Results

Table 2 contains the changes in the Fe and Mn concentrations after ten years for Fe, Mn, and Cr. In all three alloys, the manganese burns out while iron burns in. Some reactions transmute Fe to Mn, while other reactions transmute Mn to Fe. The Fe-Mn balance depends strongly on the starting concentrations of each element. Table 3 contains the composition of alloy R77 after each irradiation time. The iron concentration increases by 5%, while the manganese decreases by 18% after ten years. The chromium content doubles. Phase instabilities are not likely to arise for these levels of transmutation.

Table 3 also shows that in solute-modified alloys, only tungsten is expected to change substantially (-40%), but considering the low-starting level of this solute-hardening element, no change in phase-stability is expected.

Calculations for these alloys in the much harder spectrum of the first wall of the MARS conceptual reactor showed compositional changes of smaller magnitude than in STARFIRE and opposite in effect, i.e., relative enrichment of manganese. Thus, in either MARS or STARFIRE, no transmutation-induced phase stability problems are expected.

TABLE 1

PREIRRADIATION COMPOSITION OF ALLOYS STUDIED

| Alloy Designation | Composition (wt%) |
|-------------------|--|
| R67 | 70 Fe, 15 Mn, 15 Cr |
| R72 | 70 Fe, 30 Mn |
| R77 | 64.5 Fe, 30 Mn, 2 Cr, 0.4 C, 0.15 N, 1.0 V, 0.05 P, 0.005 B, 1.0 W, 0.5 Ni, 0.4 Si |

TABLE 2

RELATIVE CHANGES IN ATOMIC FRACTIONS AFTER TEN YEARS IN STARFIRE

| Element | R67 | R72 | R77 |
|---------|-----|------|------|
| Fe | 0% | 4% | 5% |
| Mn | 4% | -17% | -18% |

6.0 References

1. J. R. Bates, F. A. Garner and F. M. Mann, J. Nucl. Mater. 103 & 104, 1981, pp. 999-1004.
2. F. M. Mann, Transmutation of Alloys in MFE Facilities as Calculated by REAC, HEOL-TME 81-37, Hanford Engineering Development Laboratory, Richland, WA, August 1982.
3. R. Kisney, Compiler, ENDF/8 Summary Documentation (ENDF-201), 3rd ed. (ENDF/8-V), BNL-NCS-17451, Brookhaven National Laboratory, Upton, NY, 1979.

7.0 Future Work

None.

8.0 Publications

None.

TABLE 3
STARFIRE-INOUCEO TRANSMUTATIONS IN ALLOY R77

| Element | Atomic Fractions of Elements (wt%) | | | | | Change after 10 yr | |
|---------|------------------------------------|----------|----------|----------|----------|--------------------|-------|
| | Initial | 1 yr | 2 yr | 5 yr | 10 yr | A | % |
| Fe | 0.630 | 0.635 | .640 | .650 | .663 | .033 | 5.2 |
| Mn | 0.298 | 0.292 | .285 | .268 | .245 | -.053 | -17.7 |
| Cr | 0.021 | 0.022 | .024 | .030 | .040 | .019 | 92.5 |
| C | 0.018 | 0.018 | .018 | .018 | .018 | -2.6 (-4) | -1.5 |
| V | 0.011 | 0.011 | .011 | .011 | .011 | 4.0 (-4) | 3.8 |
| Si | 7.7 (-3) | 7.7 (-3) | 7.7 (-3) | 7.6 (-3) | 7.6 (-3) | -1.5 (-4) | -2.0 |
| N | 5.8 (-3) | 5.8 (-3) | 5.8 (-3) | 5.7 (-3) | 5.5 (-3) | 3.5 (-4) | -5.9 |
| Ni | 4.7 (-3) | 4.6 (-3) | 4.5 (-3) | 4.4 (-3) | 4.2 (-3) | 5.0 (-4) | -10.7 |
| W | 3.0 (-3) | 2.5 (-3) | 2.3 (-3) | 2.0 (-3) | 1.8 (-3) | 1.2 (-3) | -39.5 |
| P | 8.8 (-4) | 8.7 (-4) | 8.7 (-4) | 8.5 (-4) | 8.2 (-4) | 5.7 (-5) | -6.5 |
| B | 2.5 (-4) | 1.2 (-4) | 1.3 (-4) | 1.6 (-4) | 2.1 (-4) | 4.5 (-5) | -18.1 |
| Re | - | 4.4 (-4) | 6.8 (-4) | 9.5 (-4) | 1.2 (-3) | 1.2 (-3) | |
| Li | - | 1.4 (-4) | 1.5 (-4) | 1.5 (-4) | 1.6 (-4) | 1.6 (-4) | |
| Co | - | 3.1 (-5) | 5.0 (-5) | 9.2 (-5) | 1.5 (-4) | 1.5 (-4) | |
| Ti | - | 2.2 (-5) | 4.5 (-5) | 1.2 (-4) | 2.6 (-4) | 2.6 (-4) | |
| Be | - | 1.5 (-5) | 3.0 (-5) | 7.5 (-5) | 1.5 (-4) | 1.5 (-4) | |
| Al | - | 1.3 (-5) | 2.7 (-5) | 6.7 (-5) | 1.3 (-4) | 1.3 (-4) | |
| Ta | - | 1.1 (-5) | 1.9 (-5) | 9.9 (-6) | 2.8 (-6) | 2.8 (-6) | |
| Mg | - | 7.6 (-6) | 1.5 (-5) | 3.8 (-5) | 7.6 (-5) | 7.6 (-5) | |
| S | - | 2.3 (-7) | 5.4 (-7) | 1.4 (-6) | 2.7 (-6) | 2.7 (-6) | |
| U | - | - | - | 5.5 (-7) | 1.4 (-6) | 1.4 (-6) | |

RECENT INSIGHTS ON THE SWELLING AND CREEP OF IRRADIATED AUSTENITIC ALLOYS

F. A. Garner (Hanford Engineering Development Laboratory)

1.0 Objective

The object of this effort is to assess the impact of recently attained swelling and creep data on ADIP alloy development efforts, as well as on theoretical modeling efforts and fission-fusion correlation development.

2.0 Summary

It appears that all austenitic Fe-Ni-Cr alloys eventually swell during neutron irradiation at a rate of $\sim 1\%/dpa$ over a surprisingly large range of temperature. In addition, there is no evidence that saturation of swelling will occur in commercial alloys at engineering-relevant levels. The sensitivities of swelling to variations in composition, fabrication and environment lie almost exclusively in the duration of the transient regime of swelling. Irradiation creep rates at high exposures are also expected to exhibit a similar parametric insensitivity, largely because the major creep contribution appears to be proportional to the swelling rate. The implications of these conclusions for various OAFS and ADIP activities are discussed.

3.0 Program

Title: Irradiation Effects Analysis (AKJ)
Principal Investigator: O. G. Doran
Affiliation: Hanford Engineering Development Laboratory

4.0 Relevant OAFS Plan Task/Subtask

Task II.C.16 Composite Correlation Models and Experiments

5.0 Accomplishments and Status

5.1 Introduction

The application of austenitic steels in fusion reactors will be limited in part by their potential for large levels of irradiation creep and swelling, an extreme example of which is shown in Figure 1. The factors governing these two deformation phenomena have recently become better understood as a result of extensive new data fields obtained in the various national breeder reactor programs.

As will be demonstrated in this paper, it appears that swelling and creep are not only strongly interrelated phenomena, but that all austenitic alloys in the Fe-Ni-Cr system tend to evolve during irradiation toward characteristic rates of creep and swelling that are surprisingly independent of compositional and fabrication variables. In addition, the dependence of these characteristic rates on environmental variables such as temperature, displacement rate, helium and stress also appears to be much weaker than previously envisioned by the radiation damage community.

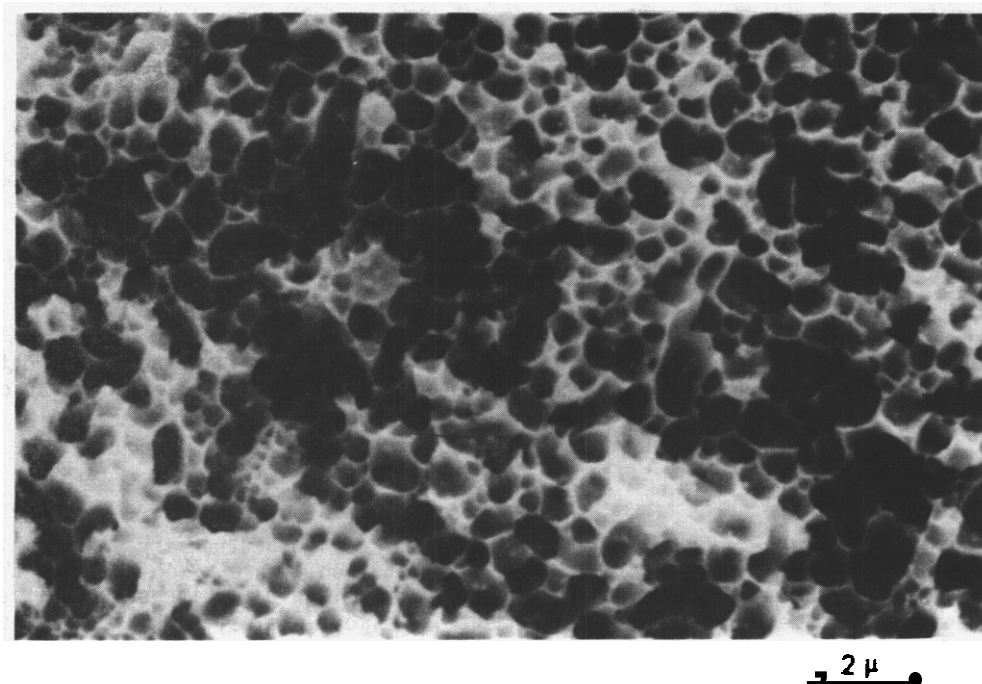


FIGURE 1. Scanning Micrograph of Voids on the Surface of Fractured 20% Cold-Worked AISI 316 Irradiated at 510°C to 120 dpa in EBR-II. The swelling is 72%. (Courtesy of W. J. S. Yang. Westinghouse Hanford Company)

52 Irradiation Creep

Irradiation creep data are generally more difficult to obtain than are swelling data, requiring more and larger specimens and also requiring more out-of-reactor measurement and analysis. The measured strains of creep specimens contain contributions not only from swelling and creep processes but also from recovery and precipitation sequences. With the exception of the swelling-induced strains, these other contributions are usually anisotropically distributed and texture-dependent. All four of the strain contributions can be stress-dependent, however, and since three of these contributions are usually not completely separated from the true creep component of strain, published data on creep rates of different alloys therefore exhibit unavoidably larger scatter than do swelling data.

In spite of differences in availability of data and their ease of interpretation, both creep and swelling appear to respond to compositional, fabrication and environmental variables in the same manner, yielding much circumstantial evidence that supports a correlation of swelling and creep. Puigh and coworkers demonstrated that the peaked temperature dependence of swelling in the alloys AISI 316, M813 and Nimnic PE16 are mirrored in the peaked temperature dependence of irradiation creep. Paxton and coworkers also demonstrated a similar relationship for the alloy A286, which exhibits a valley rather than a peak in the temperature dependency of both swelling and creep. An updated version of these data is shown in Figure 2. Note that the swelling data clearly show the contribution of a precipitate-related densification process, the strains of which are usually designated as components of the "true" creep rate.

More recently, Boutard and coworkers demonstrated that during isothermal irradiation a strong correspondence between swelling and creep exists in several heats of AISI 316 irradiated in two different fast reactors and in both the annealed and cold-worked conditions. Non-isothermal temperature histories which have been shown to accelerate swelling of AISI 316 to rates approaching 1%/dpa were also found to strongly accelerate irradiation creep. A much stronger swelling-creep relationship has been proposed, however, by Foster and coworkers and confirmed by Boutard and others, where:

$$\epsilon/\sigma = B_0 + DS \tag{1}$$

This relationship ignores the short transient usually observed in cold-worked alloys and states that the creep rate per unit stress and displaced atom is described by the creep compliance B_0 plus another contribution proportional to the swelling rate S . Ehrlich has compiled the results of published creep studies and has shown that $B_0 \sim 10^{-10}$ MPa⁻¹ dpa for a surprisingly large range of austenitic steels. Boutard and coworkers reached a similar conclusion. These studies indicated either a rather weak dependence or no dependence of B_0 on irradiation temperature. Atkins and McElroy noted that in proton irradiation studies a

similar insensitivity of β_0 to temperature and composition was also observed in nickel alloys, stainless steels, PE16 and even in non-austenitic metals such as Zr, Mo and Hf.

Ehrlich further noted that to within 20% the D-coefficients determined for both annealed 304L and cold-worked 1.4981 steels agree, with $D \approx 10^{-2} \text{ MPa}^{-1}$. A similar insensitivity of D to starting microstructure and heat identity was observed in AISI 316 by Boutard.⁷ Considering the difficulties associated with analysis of creep data, this level of agreement is surprising.

If we accept the proposed insensitivity of β_0 and D to composition and starting microstructure, then the sensitivities of swelling will dominate the creep behavior at high fluence. Note that Eq. 1 requires a swelling rate of only 0.01%/dpa or greater to give dominance to the DS term over that of the β_0 term. What are the parametric trends in swelling, and are there compositional insensitivities similar to those of the creep behavior?

5.3 Swelling of Pure Nickel

Iron and chromium do not exist with f.c.c. structure at void-relevant temperatures, but f.c.c. nickel has often been irradiated. Two of these studies have been conducted at sufficiently small fluence increments in fast reactors to show that at temperatures in the range 400-460°C pure nickel swells initially at ~1%/dpa but quickly tends to saturate, as shown in Figure 3. Most other researchers did not generate sufficient data at one temperature to discriminate between the saturation and linear swelling regimes.

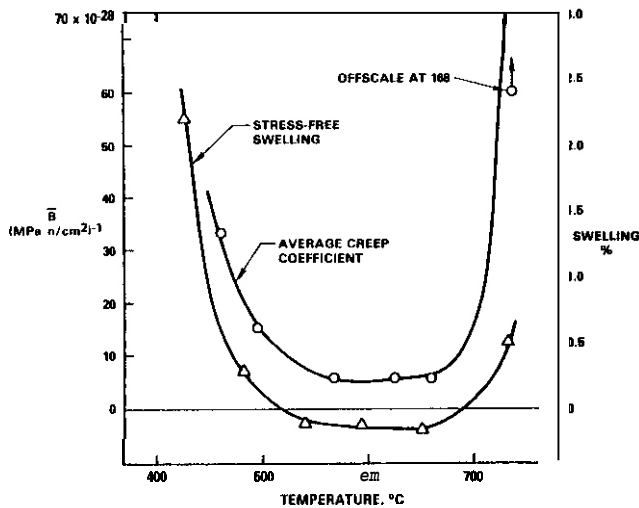


FIGURE 2. Temperature Dependence of Both the Average Creep Coefficient \bar{B} and the Stress-Free Swelling at Solution-Treated and Aged A286 at $3.8 \pm 0.2 \times 10^{21} \text{ n/cm}^2$ ($E \geq 0.1 \text{ MeV}$), or ~19 dpa in EBR-II.

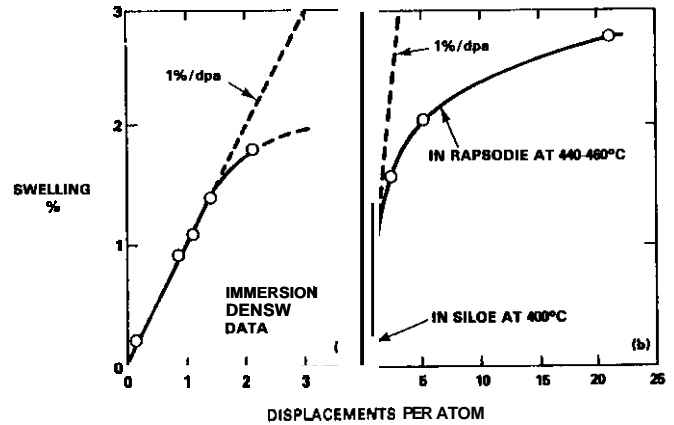


FIGURE 3a. Swelling Observed in 99.95 Nickel at 400°C for Rapsodie.
3b. Swelling Observed in 99.98 Nickel for Rapsodie and Siloe.

5.4 Saturation Regime of Swelling

Ion irradiation studies of nickel have shown both regimes, although the steady-state swelling rate was shown to be depressed by a factor of five or more below the 1%/dpa level by the action of the injected interstitial.¹⁶ In regions of the specimen where the influence of the injected interstitial was minimal, the swelling rate approached 1%/dpa.

Although nickel starts swelling at very low displacement levels, most alloys exhibit a substantial incubation or transient regime prior to the so-called "steady-state" or post-transient regime, as shown in Figure 4. To date the saturation regime has not been observed in neutron irradiations of Fe-Ni-Cr alloys, although it was observed in ion irradiations of Fe-17Cr-16.7Ni-2.5Mo (20% swelling at 627°C, 4 MeV Ni⁺ ions)¹⁷ and AISI 316 (260% swelling at 625°C, 140 keV protons).

The relatively low swelling observed in pure nickel by Johnston and coworkers¹⁶ during 5 MeV Ni⁺ irradiation (Figure 5) is thought to reflect primarily the influence of saturation but also the increasing difficulty at higher temperatures of maintaining bulk-representative microstructures close to the surface of very soft metals. In the Fe-15Cr-Ni alloys shown in Figure 5 saturation either does not happen or occurs at much higher swelling levels.

5.5 Swelling of Simple Ternary Alloys

Figure 5 leads to one conclusion, however, later found to be atypical of neutron irradiation; that there exists a strong dependence of swelling in Fe-Ni-Cr alloys on irradiation temperature. In fact, the temperature dependence of neutron-induced swelling is much less pronounced than that induced by ions. It has been shown that the influence of the injected interstitial effect at low temperature^{16,20} combined with the surface influence^{16,20} at high temperature distorts the temperature dependence of ion-induced swelling.

A strong dependence of swelling on both nickel and chromium content (Figure 6) has also been found in studies on both solute-free ternary alloys and solute-modified commercial alloys, using ion, electron²¹ and neutron²² irradiation. However, none of these studies showed unambiguously whether the influence of compositional variations lies in the transient or post-transient regime.

Garner and Brager^{23,24} have recently published an extensive data base on fifteen Fe-Ni-Cr ternary alloys with low solute levels. These were irradiated in EBR-II at eight temperatures between 400 and 650°C to exposures as large as 110 dpa. These data show that the primary influence of nickel and chromium content lies in the duration of the transient regime and that the post-transient swelling rate is ~1%/dpa, which is relatively insensitive to both irradiation temperature and composition. As illustrated in other papers, the effect of composition on swelling of ternary alloys is a second-order void nucleation effect visible only at higher neutron irradiation temperatures,²⁵ the impact of which is distorted in low-temperature ion irradiations.^{16,26}

For each neutron-irradiated ternary alloy, a temperature can be designated as the break-away temperature T_B . Below T_B there is essentially no composition or temperature dependence of swelling in the range $400^\circ\text{C} < T < T_B$, as shown in Figure 7. For $T > T_B$ the duration of the transient regime increases with temperature as shown in Figures 8 and 9a. The break-away temperature decreases with increasing nickel and decreasing chromium content. The longest transient regimes at a given temperature above T_B occur at ~35-40% nickel and relatively low chromium levels, as shown in Figure 9b. The behavior shown in Figures 7 through 9 is quite typical of that exhibited by the other ternary alloys described in References 29-31.

There does not appear to be any possibility of early saturation of swelling in Fe-Ni-Cr ternaries. For those higher-nickel alloys irradiated to the highest exposures (90-110 dpa), swelling levels of 50-70% were frequently observed.³²

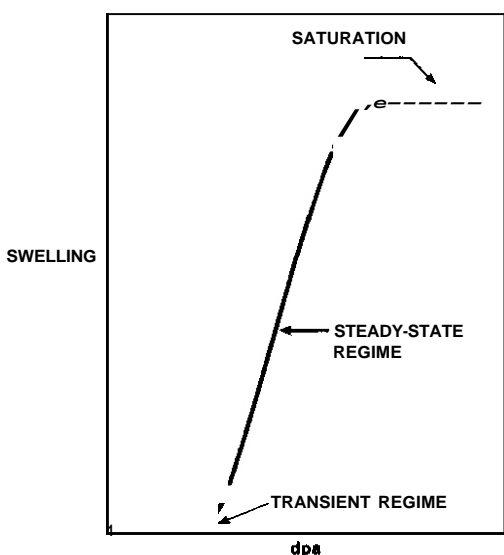


FIGURE 4. Schematic Representation of the Three Regimes of Radiation-Induced Swelling.

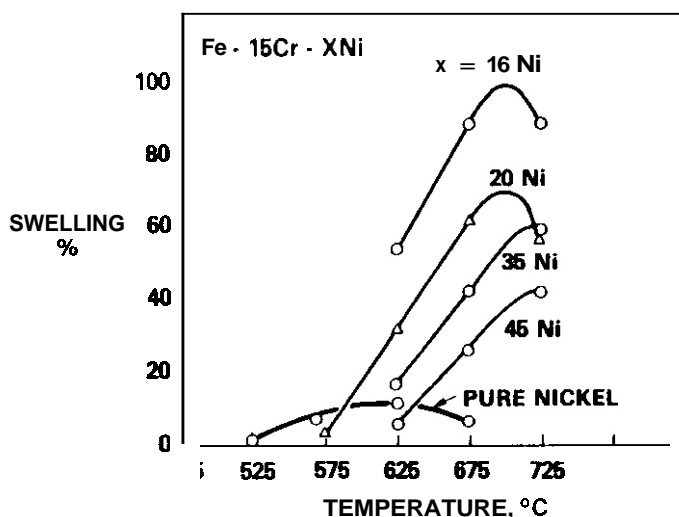


FIGURE 5. Swelling of Nickel and Fe-15Cr-Ni Ternary Alloys After Irradiation with 5-MeV Ni⁺ Ions to 140 dpa.¹⁹

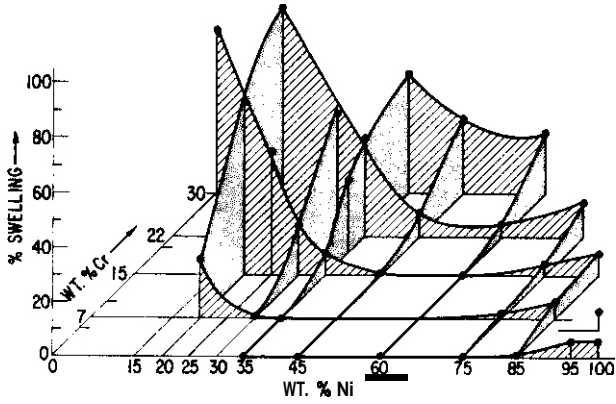


FIGURE 6. Swelling of Fe-Ni-Cr Alloys After Irradiation at 675°C with 5-MeV Ni⁺ Ions to 116 dpa.²¹

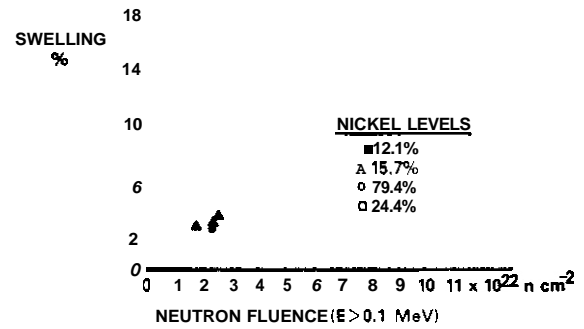


FIGURE 7. Swelling of Neutron-Irradiated Fe-15Cr-Ni Alloys for Temperatures Between 400°C and 510°C, Ni Levels Between 12.1% and 24.4%.²⁹ Note that $1.0 \times 10^{22} \text{ n/cm}^2$ is ~ 5 dpa.

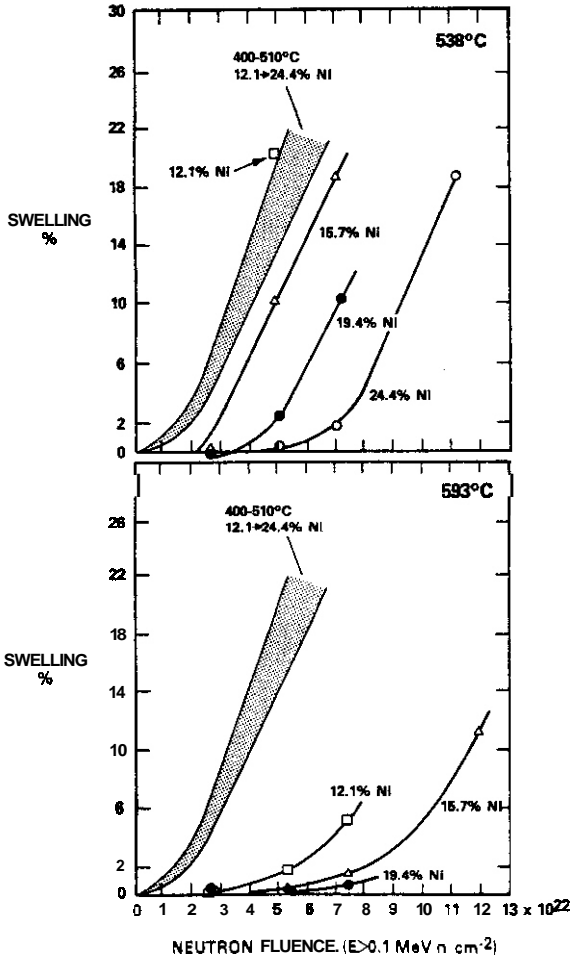


FIGURE 8. Influence of Temperature and Ni Content on the Neutron-Induced Swelling of Fe-Ni-15Cr Alloys.²⁹

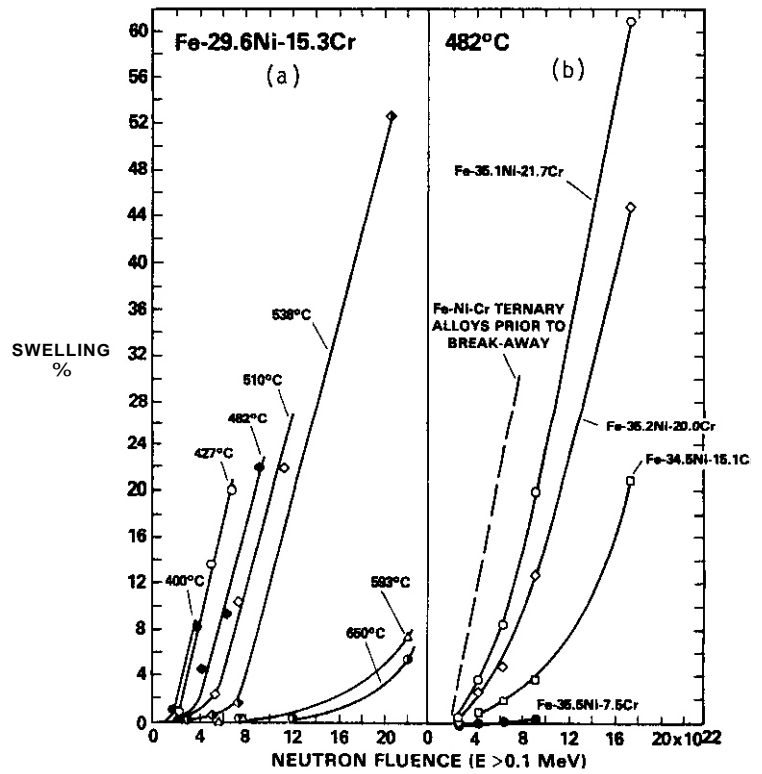


FIGURE 9. Influence of Temperature and Cr Level on Neutron-Induced Swelling of Fe-Ni-Cr Alloys Above T_B .^{29, 31}

The swelling of stainless steels is known to be sensitive to temperature, composition, displacement rate and preirradiation thermal-mechanical treatment. In general, the addition of solute, particularly silicon, leads to an extension of the transient regime by temporarily suppressing void nucleation. The development of swelling in these steels has also been correlated with the irradiation-induced micro-chemical evolution in which the silicon and nickel levels of the matrix are reduced by precipitation of phases rich in these nucleation-suppressing elements. (Silicon is much more effective per atom in suppressing void nucleation than is nickel, however). It has also been shown that the parametric sensitivities of swelling in the transient regime are mirrored in the sensitivities of the precipitation process.

This microchemical evolution is ordinarily very sluggish and leads to long transient regimes, particularly in cold-worked steels. As shown later this often yields continuous curvature in the swelling vs. fluence behavior to very high swelling levels. It has been demonstrated, however, that this evolution in AISI 316 can be accelerated under some conditions such as in-reactor temperature decreases or preirradiation thermal aging. Both of these temperature histories accelerate the rate of curvature and foster the quick attainment of the 1%/dpa swelling rate characteristic of the austenitic Fe-Ni-Cr system. There were indications of this behavior in a number of 300 series steels as early as 1975. Figure 10a shows that three steels aged at 704°C in sodium for 10,000 to 15,000 hours all swelled at ~1%/dpa when subsequently irradiated at 480°C. Even without aging, this swelling rate was observed in AISI 304L (Figure 10b) where the combined influence of annealing, low nickel content (~9%) and low carbon level leads to the shortest incubation periods observed in the 300 series steels.

Several factors precluded the earlier recognition of both the magnitude and parametric insensitivity of the post-transient swelling rate in the 300 series steels. The major factor was the long duration of the solute-extended transient coupled with its sensitivity not only to temperature history but also to gradients in displacement rate. Note in figures 11 and 12 the strong and temperature-dependent effect of displacement rate on the duration of the transient regime of AISI 316. At temperatures in the vicinity of 500°C or below the effect of displacement rate on the transient reverses in the annealed steel, and swelling increases at higher displacement rate, as shown in Figure 13. This reversal has been attributed to the displacement rate dependence of low temperature radiation-stable phases such as γ' and the time dependence of high temperature intermetallic phases. In cold-worked AISI 316 the effect of displacement rate below 500°C is much smaller.

Other studies have shown that the effects of cold-working, reactor spectra and helium and applied stress also manifest themselves in the transient regime.

In data derived from many different structural components some of the less obvious parametric trends are often obscured by data scatter as shown in Figures 11, 12 and 14. This scatter has been shown to arise from the sensitivity of the transient regime to the combined effects of a large number of local environmental parameters. In addition, the accumulated strain at large exposures causes long reactor components to grow such that points far from the fixed end experience relatively large and time-dependent changes in position and environment. This adds to the uncertainties associated with description of environmental parameters.

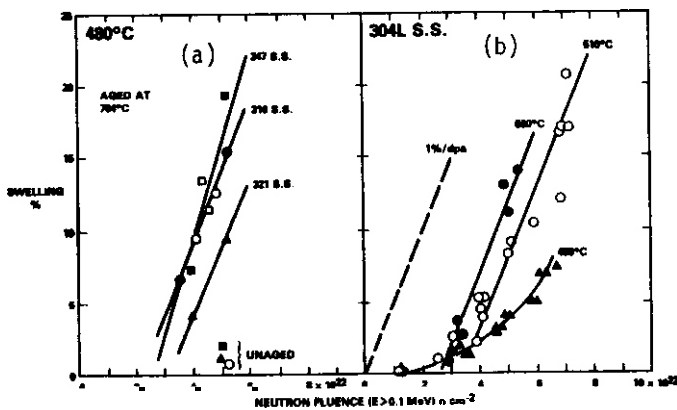


FIGURE 10a. Comparison of Swelling of Aged and Unaged 300 Series Steels.
 10b. Swelling of Annealed 304L. All four steels were irradiated in EBR-II and swelled at ~1%/dpa.

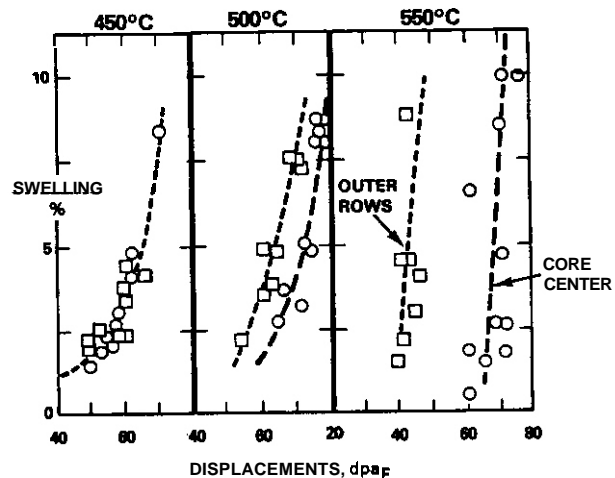


FIGURE 11. Influence of Temperature and Displacement Rate on Swelling of Annealed AISI 316 Cladding in Rapsodie.

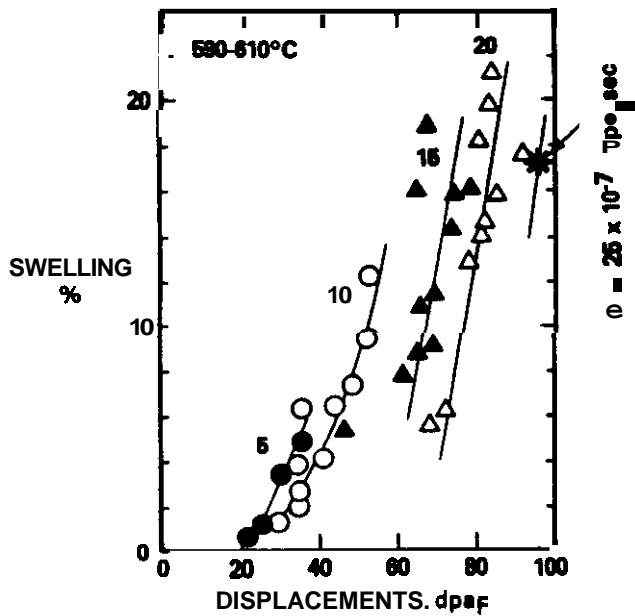


FIGURE 12. Influence of Displacement Rate on Swelling of CW AISI 316 Cladding at $\sim 600^\circ\text{C}$ in Phenix.⁴⁵ Note that 100 French $\text{dpa}_F = 77 \text{ dpa}_{\text{NRT}}$ (see p. 5 in Ref. 27).

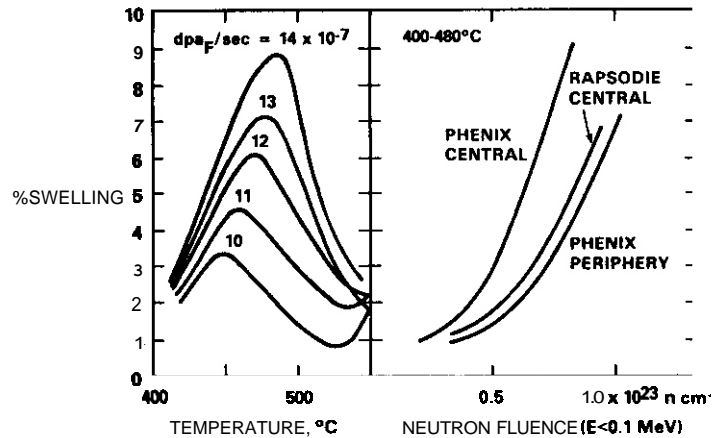


FIGURE 13. Influence of Displacement Rate on Swelling of Annealed AISI 316 at Temperatures Below 500°C .⁴⁶ The periphery of Phenix and the central region of Rapsodie have displacement rates roughly 1/2 that of the central region of Phenix.

Whereas an earlier analysis of annealed 304L swelling data concluded that there is a strong dependence of "steady-state" swelling rate on temperature,⁴⁷ Figure 14 shows that, even in the absence of corrections for neutron spectra, there exists a broad temperature range over which the swelling is essentially independent of temperature.⁴⁸⁻⁵⁰ The scatter in the range $450\text{--}538^\circ\text{C}$ camouflages a continuing increase in swelling rate with fluence. At lower temperatures, the transient duration increases, but the apparent slow decrease in the eventual swelling rate reflects primarily the softening of the neutron spectra in the region where these temperatures exist. When plotted vs. dpa the curves in Figure 14b become more parallel to the band shown in Figure 14a.

While the transient swelling regime may be sensitive to temperature for some heats of steel, other heats are relatively insensitive to temperature, as shown in Figure 15. The continuous "curvature" or increase in swelling rate is not masked by data scatter since the three data points shown at every temperature in Figure 15 represent interim measurements on a single specimen. Note the sharp discontinuity in swelling at $\sim 460^\circ\text{C}$. Other data at higher exposures show that at both above and below this discontinuity the swelling rate indeed reaches $\sim 1\%/ \text{dpa}$ (see Figure 20, for example, at 500 and 420°C). The sensitivity of the transient regime to environmental history is graphically demonstrated in Figure 15b, where the same heat and lot of tubing was used as fuel pin cladding.⁵¹ Not only is the transient regime longer but the range of temperature insensitivity is larger. A compilation of single-specimen swelling data is presented elsewhere for many heats of AISI 316 stainless steel.⁵²

Figure 16a demonstrates that the complex temperature dependency often reported for swelling of some heats arises from a strong dependence of the transient regime on temperature. The valley at 450°C in Figure 16b is a remnant of the "double-bump" swelling behavior usually observed in annealed AISI 316, but suppressed by cold-working.⁵³ Note that for this heat there appears to be a plateau in swelling above $\sim 550^\circ\text{C}$. In general it is difficult to assess the high temperature behavior, since swelling profiles derived from structural components at temperatures above 600°C are dominated by the steep flux gradients associated with these temperatures.⁵⁴

Whereas it is usually assumed that swelling of 300 series steels ceases in the range $650\text{--}700^\circ\text{C}$, swelling of AISI 316 has been found to show no hint of decreasing swelling rate at 650°C ⁵⁵ and to extend above 700°C when sufficient exposure is attained (Figure 17).⁵² In fact, AISI 304 has been observed to swell to temperatures as large as 800°C .⁵³ The upper limit of swelling has not been determined, but the presumed absence of swelling in the range $700\text{--}800^\circ\text{C}$ reflects more the absence of high fluence experiments in this range than the absence of swelling itself.

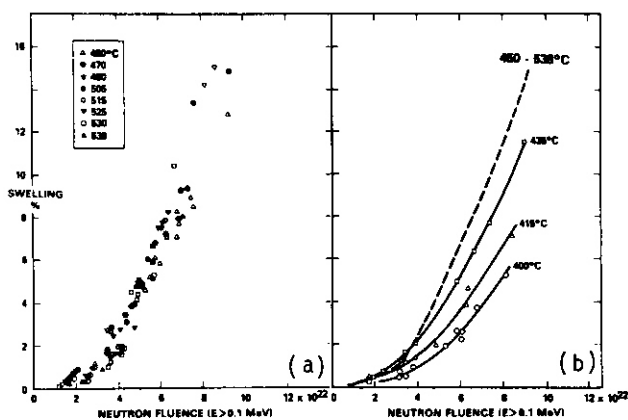


FIGURE 14. Swelling of EBR-II Outer Fuel Capsules Constructed from Solution-Annealed AISI 304L.^{49/50}

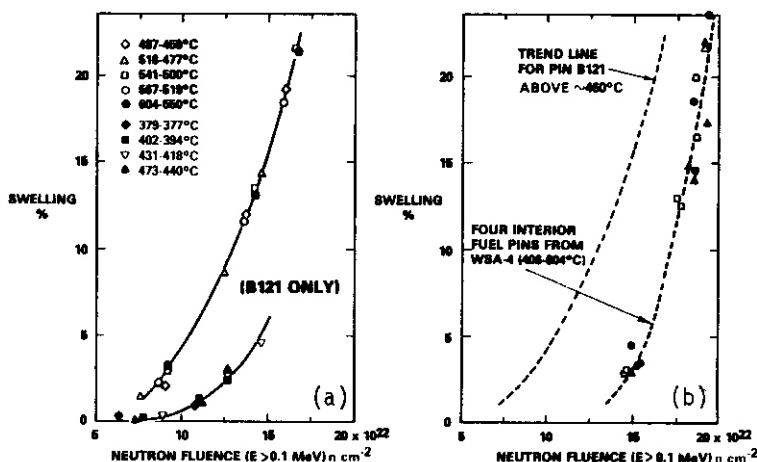


FIGURE 15. Swelling of 20% CW N-Lot AISI 316 in Two Separate EBR-II Experiments, Showing a Relative Insensitivity of Swelling to Temperature as well as a Strong Dependence of Transient on Environmental History." The slope of the WSA-4 curve above 10% swelling is R1%/dpa.

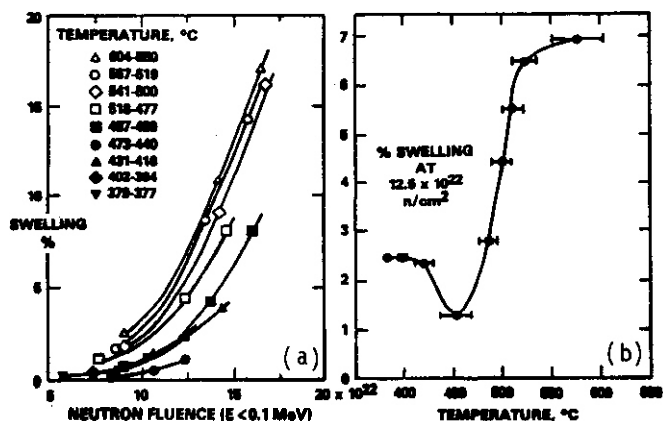


FIGURE 16. Swelling of 20% Cold-Worked R-Lot AISI 316 in EBR-II. (Single-specimen immersion density data.)

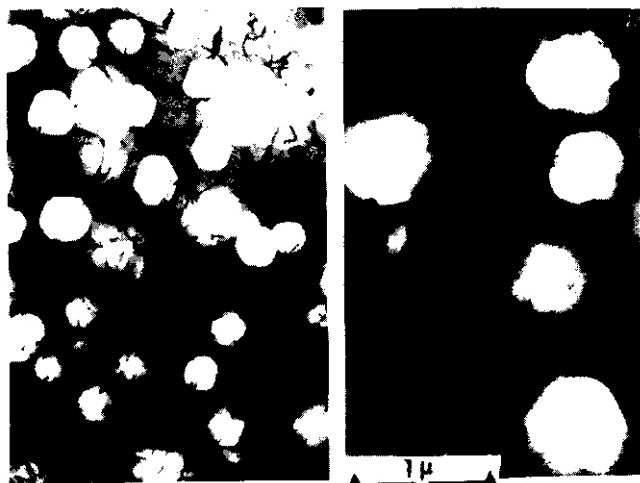


FIGURE 17a. 2.5% Swelling at 38 dpa and 667-710°C.
17b. 2.8% Swelling at 31 dpa and 700-718°C, Determined by Immersion Density Measurement. Voids observed in 20% CW AISI 316 (Lot CN-13) after irradiation in EBR-II.⁵²

5.7 Titanium-Modified 300 Series Stainless Steel

Extensive neutron-induced swelling data from the U.S. Breeder program show that modification of 300 series stainless steels by titanium addition does not change the eventual swelling rate. Titanium does change the duration of the transient regime, however, and exhibits strong synergisms with other solute elements. Once the MC-type precipitates are replaced by nickel and silicon-rich precipitates, swelling accelerates quickly,⁵⁴⁻⁵⁵ as demonstrated in Figure 18. This loss of phase stability and its relationship to swelling has also been shown to be sensitive to pulsing of the radiation environment.⁵⁵

With an appropriate balance of various solutes and with thermal-mechanical pretreatments designed to stabilize MC-type precipitates, it appears that the potential exists for extending the transient regime somewhat. Based on current studies, however, 150-200 dpa appears to be the upper exposure limit and the microchemical stability appears fragile enough that it might not survive welding or even various in-reactor temperature histories. Other papers in these proceedings describe the U.S. effort to develop a Prime Candidate Alloy (PCA) for fusion applications based on titanium-modified AISI 316.^{56/57}

5.8 Swelling of Other Commercial Alloys

The ion studies of Johnston and coworkers^{19,21} greatly influenced the design of U.S. neutron experiments and led to irradiation of many alloys with higher nickel levels. High fluence data have only recently become available on these alloys.^{23,33} As shown in Figures 19 and 20, once swelling of these alloys commences they do so at rates that quickly approach 1%/dpa. The transients at a given temperature exhibit trends with nickel, chromium and solute levels that are quite consistent with the trends exhibited by the simple ternary alloys, but the transients have been extended by the solute additions. This is particularly easy to see in annealed alloys. In general, cold-working further extends the transient regime.^{28,58}

It should also be noted that transients at high nickel levels are shortest at the lower irradiation temperatures. Not only does this observation agree with the results of the ternary alloy irradiations but it suggests that the peaks in swelling might exist at lower temperatures (<400°C) than investigated in these studies.

The largest levels of neutron-induced swelling to date are shown in Figure 70 for Hastelloy-X (80%) and 20% cold-worked heat 81583 AISI 316 (72%). The latter was also shown in Figure 1. These two alloys have vastly different compositions and yet eventually swell at essentially identical rates.

5.9 Implications for Alloy Development

If swelling and creep behavior were the only considerations invoked as criteria for further development, two major approaches in the austenitic system are suggested by these results. The first is to probe the low chromium range (<10%) of the higher nickel alloys,^{24,29,30} employing solute modification to extend the transient and hopefully stabilize the phases existing prior to irradiation. However, the most successful swelling-resistant commercial alloys to date, Inconel 706⁵⁹ and Inconel 718⁶⁰ actually have slightly higher chromium levels. Note in Figure 20, however, that high nickel levels per se are no guarantee of transient regimes that are longer than those of AISI 316.

The second approach is to continue pursuing the stabilization of the matrix and MC-type precipitates in titanium-modified alloys, recognizing that once these precipitates are replaced by nickel and silicon-rich phases, accelerated swelling will commence shortly thereafter.

Perhaps the most sobering implication of this work is that, on the single consideration of swelling, no austenitic alloy studied to date has the potential to reach exposures in excess of 700 dpa or first-wall loadings of 20 MWyr/m². For goals of this magnitude one must consider the ferritic steels which appear to swell at much lower rates.^{58,59}

5.10 Implications for Theoretical Modeling

The insights gained from these studies focus our attention more strongly on void nucleation theory and phase stability considerations, and deemphasize the attention paid to conventional rate theory. One can use rate theory, however, to describe the relative insensitivity of the post-transient swelling rate to temperature, displacement rate, helium/dpa ratio and applied stresses.^{32,60} At the high sink strengths generated in irradiated austenitic alloys, rate theory shows that the sensitivities of swelling are effectively decoupled from the sensitivities of the microstructure. This largely explains why the homogenization of the cavity structure at high helium/dpa ratios does not appear to affect the post-transient swelling rate.⁵²

The compositional sensitivity of void nucleation is now being explored^{32,36,61} and involves both composition-dependent diffusion behavior of point defects in the alloy matrix and the consequences of radiation-induced segregation of nickel at void surfaces. An area requiring additional attention is the compositional sensitivity of Frank loop and dislocation evolution.

5.11 Application of Fission-Derived Insights to Fusion Environments

There are a number of considerations involved in the application of these fission-derived insights to fusion conditions. The spectral dependence of displacement damage for 14 MeV neutrons has been assumed in this paper to be adequately covered by the use of dpa as the exposure index, but this assumption can not be fully tested in existing facilities.

The differences in non-gaseous transmutants in various neutron spectra can be substantial,³² but for AISI 316 in HFIR and EBR-II such differences were found to manifest themselves primarily in the precipitate compositions and not in the transient duration or the post-transient swelling rate.^{52,63,64} Considering the

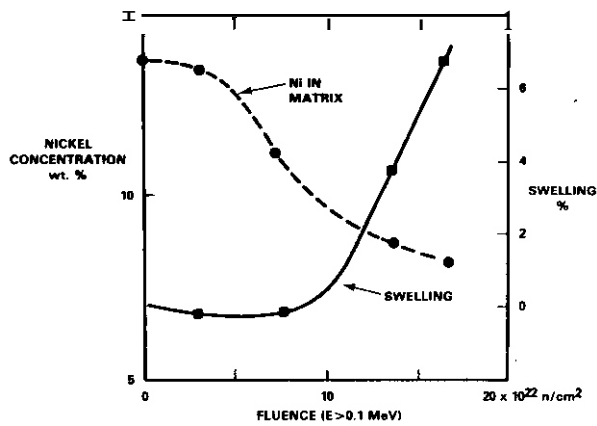


FIGURE 18. Correlation of Swelling with Matrix Ni Content Measured by EDX Microanalysis in 20% CW Ti-Modified AISI 316 Irradiated at 538°C in EBR-II.⁵⁴ Silicon is removed in a similar manner.

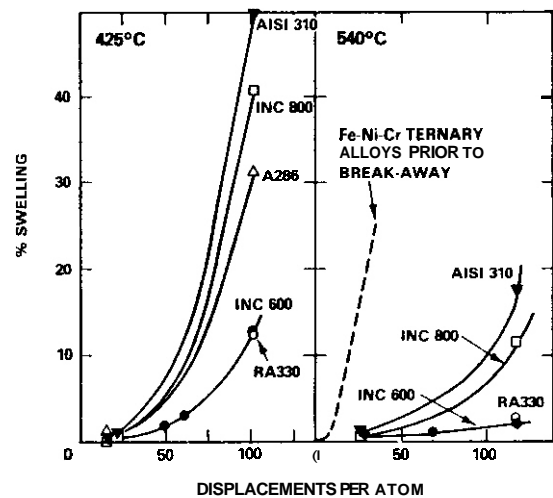


FIGURE 19. Swelling in Annealed Commercial Alloys Irradiated in EBR-II.^{28,58}

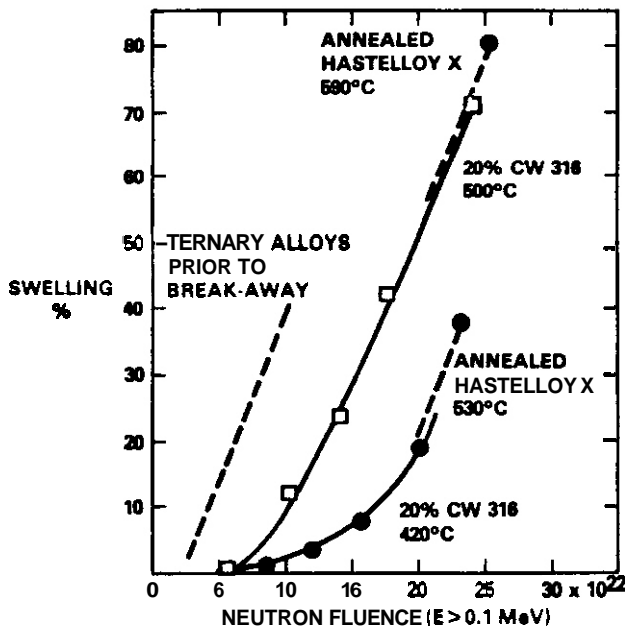


FIGURE 20. Maximum Swelling Levels Observed to Date in the US Breeder Program. "Hastelloy-X is a 19Fe-49Ni-21Cr-9Mo alloy."

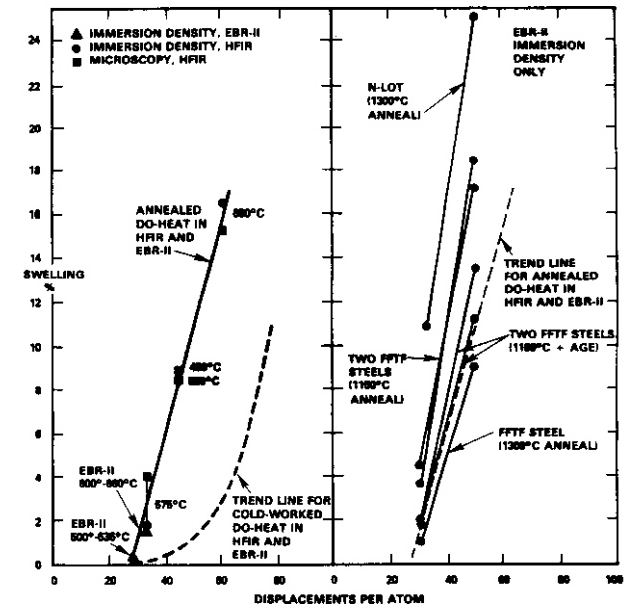


FIGURE 21. Comparison of Several Heats of Annealed AISI 316 Irradiated in HFIR and EBR-II, Showing Relative Insensitivity of Post-Transient Swelling to Temperature and Neutron Spectra."

compositional insensitivity of the post-transient regime demonstrated in this study, such a result is not surprising, and is not expected to be altered in fusion environments.

Another consideration is that of the helium/dpa ratio. As shown in Figure 21, the very large difference in helium/dpa ratio between HFIR and EBR-II did not lead to a difference in the post-transient swelling rate of annealed AISI 316. A compilation of other helium effects studies has led to the conclusion that relatively small differences in starting composition have a greater effect on the transient regime than do large variations in helium level."

There is no guarantee that these spectrum-related conclusions will apply to all alloys at all irradiation conditions. A point of additional concern is the effect of differences in environmental history. While we can specify with some confidence the eventual swelling rate, we cannot specify the duration of the transient regime for a given alloy in any untested environment. The greatest sensitivities of the transient regime of AISI 316 were found to be to temperature, displacement rate, and stress." In a Tokamak all three of these parameters will vary simultaneously, with currently unpredictable consequences.

6.0 References

1. F. A. Garner, E. R. Gilbert and D. L. Porter, ASTM STP 725, 1981, p. 680.
2. F. A. Garner, W. V. Cummings, J. F. Bates and E. R. Gilbert, Densification-Induced Strains in 20% Cold-Worked 316 Stainless Steel During Neutron Irradiation, HEDL-TME 78-9, Hanford Engineering Development Laboratory, Richland, WA, June 1978.
3. R. J. Puigh, A. J. Lovell and F. A. Garner, "Thermal Creep and Stress-Affected Precipitation of 20% Cold-Worked 316 Stainless Steel," OAFS Quarterly Progress Report, DOE/ER-0046/15, p. 114.
4. R. J. Puigh, E. R. Gilbert and B. A. Chin, ASTM STP 782, 1982, p. 108.
5. B. A. Chin and R. J. Puigh, *ibid*, p. 122.
6. M. M. Paxton, B. A. Chin and E. R. Gilbert, J. Nucl. Mater. 95, 1980, p. 185.
7. J. L. Boutard, Y. Carteret, R. Cauvin, Y. Guerin and A. Maillard, Proc. Conf. on Dimensional Stability and Mechanical Behavior of Irradiated Metals and Alloys, Brighton, England, 1983, Vol. 1, p. 109.
8. F. A. Garner, E. R. Gilbert, D. S. Gelles and J. P. Foster, ASTM STP 725, 1981, p. 698.
9. J. P. Foster, W. G. Wolfer, A. Biancheria and A. Boltax, Proc. BNES Conf. on Irradiation Embrittlement and Creep in Fuel Cladding and Core Components, London, 1972, p. 273.
10. K. Ehrlich, J. Nucl. Mater. 100, 1981, p. 149.
11. T. Atkins and R. J. McElroy, ASTM STP 782, 1982, p. 841.
12. Y. Adda, Proc. Inter. Conf. on Radiation-Induced Voids in Metals, CONF-710601, Albany, NY, 1971, p. 31.
13. G. Silverstre, A. Silvent, C. Regnard and G. Sainfort, J. Nucl. Mater. 57, 1975, p. 135.
14. G. L. Kulcinski, J. L. Brimhall and H. E. Kissinger, J. Nucl. Mater. 40, 1971, p. 166.
15. J. B. Whitley, G. L. Kulcinski, P. Wilkes and J. Billen, J. Nucl. Mater. 85 & 86, 1979, p. 701.
16. F. A. Garner, J. Nucl. Mater. 117, 1983, p. 177.
17. N. H. Packan and K. Farrell, ASTM STP 782, 1982, p. 885.
18. A. Kumar and F. A. Garner, J. Nucl. Mater. 117, 1983, p. 234.
19. W. G. Johnston, T. Lauritzen, J. H. Rosolowski and A. M. Turkalo, Radiation Damage in Metals, ASM, Cleveland, OH, 1976, p. 227.
20. F. A. Garner and J. J. Laidler, Proc. Work-Shop on Correlation of Neutron and Charged Particle Damage, CONF-760673, Oak Ridge, TN, 1976, p. 177.
21. W. G. Johnston, J. H. Rosolowski, A. M. Turkalo and T. Lauritzen, J. Nucl. Mater. 54, 1974, p. 24.
22. D. R. Harries, Proc. Consultant Symposium on the Physics of Irradiation Produced Voids, AERE-R7934, Harwell, September 1974, p. 287.
23. I. V. Gorynin and A. M. Parshin, Atomnaya Energiya 50, (5), 1981, p. 319.
24. D. Gulden and K. Ehrlich, "Void Swelling and Microstructural Development In Experimental Austenitic Alloys," Proc. Conf. on Dimensional Stability and Mechanical Behavior of Irradiated Metals and Alloys, Brighton, England, 1983, Vol. 1, p. 13.
25. A. Hishinuma, Y. Katano and K. Shiraishi, J. Nucl. Mater. 103 & 104, 1981, p. 1063.
26. J. S. Watkin, ASTM STP 611, 1976, p. 270.
27. J. F. Bates and W. G. Johnston, Proc. Inter. Conf. on Radiation Effects In Breeder Reactor Structural Materials, Scottsdale, AZ, June 1977, p. 625.
28. J. F. Bates and R. W. Powell, J. Nucl. Mater. 102, 1981, p. 200.

29. F. A. Garner, OAFS Quarterly Progress Report, DOE/ER-0046/14, August 1983, p. 133, to be published in Proc. of AIME Symp. on Tailoring and Optimizing Materials for Nuclear Applications, February 1984, Los Angeles, CA.
30. H. R. Erager and F. A. Garner, *ibid.*, p. 152.
31. F. A. Garner and H. R. Erager, to be published, Proc. 12th ASTM Inter. Symp. on Effects of Radiation on Materials, June 18, 1984, Williamsburg, VA.
32. F. A. Garner and W. G. Wolfer, "Factors Which Determine the Swelling Behavior of Austenitic Stainless Steels," DAFS Quarterly Progress Report, DOE/ER-0046/15, p. 89.
33. D. L. Plumton, H. Attaya and W. G. Wolfer, "Conditions for the Suppression of Void Formation During Ion-Bombardment," Proc. 3rd Topical Meeting on Fusion Reactor Materials, J. Nucl. Mater., in press.
34. F. A. Garner, Proc. of AIME Symp. on Phase Stability During Irradiation, Pittsburgh, PA, Oct. 5-9, 1980, p. 165.
35. H. R. Brager and F. A. Garner, *ibid.*, p. 219.
36. F. A. Garner and W. G. Wolfer, J. Nucl. Mater. 102, 1981, p. 143.
37. H. R. Brager and F. A. Garner, ASTM STP 683, 1979, p. 207.
38. H. R. Erager and F. A. Garner, ASTM STP 725, 1981, p. 470.
39. F. A. Garner and D. L. Porter, ASTM STP 782, 1982, p. 295.
40. W. J. S. Yang and F. A. Garner, ASTM STP 782, 1982, p. 186.
41. A. Boltax, J. P. Foster and U. P. Nayak, "High Dose Stainless Steel Swelling Data on Interior and Peripheral Oxide Fuel Pins," Proc. Conf. on Dimensional Stability and Mechanical Behavior of Irradiated Metals and Alloys, Brighton, England, 1983, Vol. I, p. 21.
42. H. J. Busboom, G. C. McClellan, W. L. Bell and W. K. Appleby, General Electric Report GEAP-14062, July 1975, Appendix A
43. J. E. Flinn and T. A. Kenfield, Proc. Work-Shop on Correlation of Neutron and Charged Particle Damage, CONF-760673, June 1982, pp. 253-289.
44. J. L. Seran and J. M. Dupouy, ASTM STP 782, 1982, p. 5.
45. J. L. Seran and J. M. Dupouy, Proc. Conf. on Dimensional Stability and Mechanical Behavior of Irradiated Metals and Alloys, Brighton, England, 1983, Vol. I, p. 25.
46. J. L. Boutard, G. Brun, J. Lehmann, J. L. Seran and J. M. Dupouy, Proc. Conf. on Irradiation Behavior of Metallic Materials For Fast Reactor Core Components, Corsica, France, June 5-14, 1979, p. 137.
47. F. A. Garner, OAFS Quarterly Progress Report, DOE/ER-0046/12, February 1983, p. 178.
48. F. A. Garner, OAFS Quarterly Progress Report, DOE/ER-0046/16, February 1984.
49. F. A. Garner and D. L. Porter, "A Reassessment of the Swelling Behavior of AISI 304 Stainless Steel," Proc. Conf. on Dimensional Stability and Mechanical Behavior of Irradiated Metals and Alloys, Brighton, England, 1983, Vol. 11.
50. F. A. Garner and D. L. Porter, "Factors Influencing the Swelling of 300 Series Stainless Steels," DAFS Quarterly Progress Report, DOE/ER-0046/9, May 1982, p. 170.
51. J. P. Foster and J. E. Flinn, J. Nucl. Mater. 89, 1980, p. 99.
52. H. R. Erager and F. A. Garner, J. Nucl. Mater. 117, 1983, p. 159.
53. J. L. Straalsund, H. R. Brager and J. J. Holmes, "Effect of Cold Work on Void Formation in Austenitic Stainless Steel," Proc. Inter. Conf. on Radiation-Induced Voids in Metals, CDNF-710601, Albany, NY, 1971, p. 142.
54. L. E. Thomas, Proc. 40th Annual Meeting Electron Microscopy Soc. Amer., Washington, D.C., G. W. Bailey ed., 1982, p. 597.

55. E. H. Lee, N. H. Packan and L. K. Mansur, J. Nucl. Mater. 117, 1983, p. 123.
56. P. J. Maziasz, "Anticipating Fusion Swelling Resistance for Austenitic Stainless Steels Based on Fission Reactor Data," Proc. 3rd Topical Meeting on Fusion Reactor Materials, J. Nucl. Mater., in press.
57. See papers by N. J. Grant, O. K. Harling and coworkers, Proc. 3rd Topical Meeting on Fusion Reactor Materials, J. Nucl. Mater., in press.
58. D. S. Gelles, "Swelling in Several Commercial Alloys Follows Very High Fluence Neutron Irradiation," Proc. 3rd Topical Meeting on Fusion Reactor Materials, J. Nucl. Mater., in press.
59. J. L. Straalsund, R. W. Powell and B. A. Chin, J. Nucl. Mater. 108 & 109, 1982, p. 299.
60. W. G. Wolfer, "Advances in Void Swelling and Helium Bubble Physics," Proc. 3rd Topical Meeting on Fusion Reactor Materials, J. Nucl. Mater., in press.
61. W. G. Wolfer, F. A. Garner and L. E. Thomas, ASTM STP 782, 1982, p. 1023.
62. J. F. Bates, F. A. Garner and F. M. Mann, J. Nucl. Mater. 103 & 104, 1981, p. 999.
63. H. R. Brager and F. A. Garner, J. Nucl. Mater. 103 & 104, 1981, p. 993.
64. H. R. Brager and F. A. Garner, J. Nucl. Mater. 108 & 109, 1982, p. 347.

7.0 Future Work

An irradiation creep equation based on the results of these studies will be developed for the Fusion Materials Handbook.

8.0 Publications

This report **summarizes** an invited panel paper and will be published in the Journal of Nuclear Materials as part **of** the proceedings of the Third Topical Meeting on Fusion Reactor Materials, (Sept. 1983), Albuquerque, **NM**.

9.0 Acknowledgments

This work supported by the U.S. Department of Energy under Contract DE-AC06-76FF02170.

SWELLING OF AISI 304L IN RESPONSE TO SIMULTANEOUS VARIATIONS IN STRESS AND DISPLACEMENT RATE*

D. L. Porter (Argonne National Laboratory-Idaho Falls) and F. A. Garner (Hanford Engineering Development Laboratory)

1.0 Objective

The object of this effort is to determine the factors which govern the swelling of austenitic alloys and provide guidance for the development of history-dependent swelling equations.

2.0 Summary

The duration of the transient regime of neutron-induced swelling in annealed AISI 304L at 400°C is sensitive to both stress and displacement rate variations. The simultaneous application of both variables exerts a synergistic effect on the transient regime. The duration of this regime cannot be reduced below an exposure of ~10 dpa, however, which has been found to be characteristic of all Fe-Ni-Cr austenitic alloys. This is four times larger than that currently assumed in the stress-affected swelling equation for 20% cold-worked AISI 316.

3.0 Program

Title: Irradiation Effects Analysis (AKJ)
Principal Investigator: D. G. Doran
Affiliation: Hanford Engineering Development Laboratory

4.0 Relevant DAFS Plan Task/Subtask

Task II.C.16 Composite Correlation Models and Experiments

5.0 Accomplishments and Status

5.1 Introduction

It is known that the transient regime of swelling in austenitic alloys is sensitive to a large array of variables, some of which may act synergistically. The development of history-dependent fission-fusion correlations for swelling requires that some estimate be made of the synergistic influences of those variables known to be different in the two neutron environments. It is not known, for instance, how short the duration of the transient regime can become or how to superimpose on the transient the influence of two separate variables.

Recently, it has become clear that the displacement rate is one of the important environmental variables which determine the duration of the transient regime in AISI 316. Unfortunately, well-defined experiments with separable environmental variables are in general not available.

This report describes one experiment where the combined action of temperature, displacement rate and stress can be studied. The action of the latter variable can be separated from the influence of the first two, however. The material employed in this experiment was annealed 304L stainless steel, which, by virtue of its lower nickel and carbon levels, swells somewhat earlier than does annealed 316 stainless steel.

*Work supported in part by US DOE under contract W-31-109-ENG-38.

5.2 Experimental Details

The X065 in-reactor creep experiment was conducted in Row 7 of EBR-II to study the swelling and creep behavior of annealed AISI 304L, the material which forms most of the cladding for EBR-II fuel. There were 19 pressurized tubes in this experiment, each 60 inches in length (152 cm). Each had an outer diameter of 0.737 cm, 0.051-cm wall thickness and a nominal grain size of ASTM 6. They were pressurized to yield one of seven levels of hoop stress, varying from 0 to 190 MPa. The temperature of these tubes varied from 380°C at the bottom to 415°C at the top.

The tubes were removed periodically from the reactor and the total creep and swelling deformation was measured using profilometry along the tube axis. At the termination of the irradiation series, seven of the tubes were cut into 2.5-cm sections and their density change determined using an immersion technique.

5.3 Results

Figures 1 and 2 show the results of the density change measurements. (Two figures were plotted to avoid data overlap.) The four-fold displacement variation for any one stress level arises from the variation in displacement rate along the tube. Since the tube is fixed at its bottom end each point on the original tube tends to move upward through the core during irradiation. The amount of upward displacement is the sum of the total integrated linear swelling below that point. Therefore, swelling data were obtained only from the bottom half of each tube to minimize uncertainties in position and total displacement level. The temperature varied from ~385 to ~400°C over the range chosen for examination.

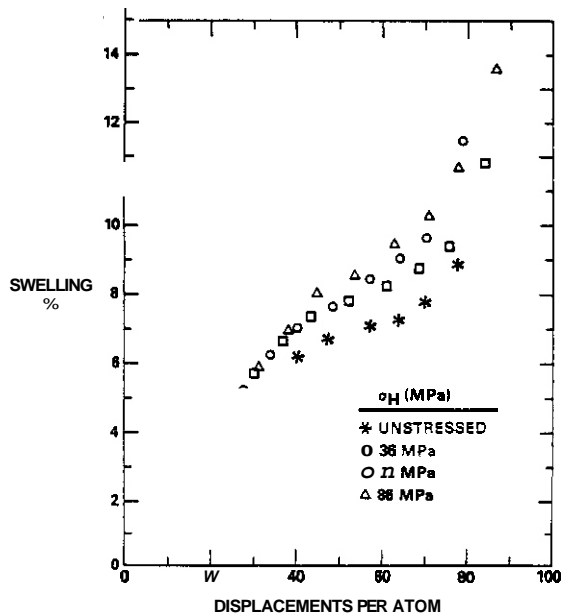


FIGURE 1. Swelling Data from AISI 304L Creep Tubes, Derived by Immersion Density.

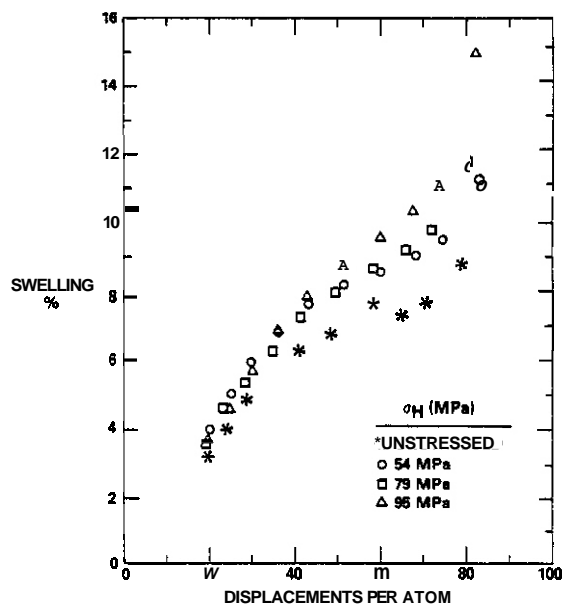


FIGURE 2. Additional Swelling Data from Creep Tubes.

The stress levels quoted in Figures 1 and 2 are those of the hydrostatic stress σ_H , which for a gas-pressurized tube is one-half of the hoop stress. This stress parameter was chosen for consistency with stress-affected swelling models developed in earlier studies.

At lower fluences and flux levels there appears to be no effect of stress on swelling. The data from all seven capsules are colinear in this range and reflect an extrapolated intercept on the exposure axis of approximately 10 dpa. At higher fluence levels, however, there is a consistent increase in swelling (at a given displacement rate) with increasing stress level.

5.4 Discussion

Each of the curves shown in Figures 1 and 2 is shaped by the combined action of three variables; displacement rate, temperature and stress level. It is very difficult to separate the effects of the first two

variables, however, particularly where there is a relatively steep gradient in displacement rate, such as occurs near the bottom edge of the core. Since the temperature varies only about 15°C in this experiment, however, the impact of temperature is presumed to be overshadowed by that of displacement rate.

Two features of these curves require explanation. The first is the shape of each curve at a given stress level. As shown in Figure 3, a similar experiment on 5% cold-worked AISI 316 yielded a similarly-shaped curve when core center profilometry measurements at different exposure levels were compared with axially varying measurements upon the termination of the experiment.³ Figure 4a shows the presumed effect of variations in displacement rate alone, drawing on the experimental observation that the influence of the displacement rate is manifested primarily in the transient regime.¹ The second feature is the shift toward lower exposures upon application of tensile stresses. Figure 4b shows the known effect of tensile stresses at constant displacement rate.⁸ In this temperature range, however, stress is usually thought to be a second order variable.^{6,7} Figure 5 shows that the effect of stress indeed saturates rather quickly, exerting a much smaller influence above 50 MPa.

At a given stress level, however, the effect of displacement rate (or conversely time-at-temperature) exerts its influence by shortening the transient until a minimum transient is approached, as shown in Figures 6 and 7. It is significant, however, that the transient duration cannot be shortened below the minimum of 2×10^{22} n/cm² ($E > 0.1$ MeV) or ~ 10 dpa observed in the solute-free austenitic Fe-Ni-Cr alloy series irradiated in the core of EBR-II,^{3,10} as illustrated in Figure 8. As shown in Figure 9 a similar minimum is observed in various 300 series steels whose temperature histories were such as to quickly yield the $\sim 1\%/dpa$ swelling rate characteristic of austenitic Fe-Ni-Cr alloys.¹¹

It is apparent then that the transient is extended primarily by the action of the solutes in 304L, primarily silicon and carbon. This is consistent with the results of recent studies on the influence of these elements.^{10,12} At the higher displacement rate, these elements apparently *do* not segregate into precipitates as readily as they do at the longer times associated with lower displacement rates. The silicon and carbon levels are thus maintained in solution for a longer period, depressing void nucleation. Apparently the action of stress on void nucleation can be more pronounced at the higher displacement rates where void nucleation is more difficult.

The 10-dpa minimum incubation period observed in various austenitic metals may be related to the minimum time required to develop the requisite dislocation microstructures in solute-bearing alloys. Porter recently demonstrated in 304L that it is not related to the time required to nucleate and grow voids.¹³ He annealed specimens irradiated at $\sim 415^\circ\text{C}$ to 22 dpa such that the dislocation density was greatly reduced, and the various solutes dispersed. This did not reduce the void density measurably nor did it reduce the $\sim 3\%$ swelling accumulated. Even though there were approximately 10^8 voids/cm the swelling curve upon subsequent reirradiation exhibited an incubation period or transient regime of ~ 10 dpa, as shown in Figure 10.

These data thus provide a rationale for placing a lower limit on the incubation parameter τ employed in the current stress-affected swelling equation. A lower limit currently exists but is a factor of four lower than that suggested by the results of this study. If the parallel with the ternary alloy results is maintained, this lower limit should also apply to AISI 316 and other 300 series alloys.

It does not appear feasible, however, to specify the magnitude and sign of the displacement rate effect for other 300 series alloys. While the effect of displacement rate measured by Porter and Hudman appears to be roughly the same for both AISI 304L and AISI 316 in Figure 11, this impression may be misleading. The strain differences measured in AISI 316 are much smaller and may represent primarily the effect of time-at-temperature on precipitate-related densification, a process known to develop small anisotropic and negative strains in this alloy.¹⁴ Otherwise one would expect that at these low temperatures that increasing the displacement rate would shorten the transient regime.³ At higher temperatures ($>500^\circ\text{C}$), however, the influence of displacement rate reverses in sign and becomes much more pronounced with increasing temperature.¹⁵

5.5 Conclusions

It appears that the transient regime of any 300 series stainless steel is sensitive to the synergistic influences of those factors which affect void nucleation, namely, solute content, displacement rate, temperature, helium and applied stress. In AISI 304L at 400°C the addition of carbon and silicon works to extend the transient regime while longer times at lower displacement rates in reactor tend to shorten the transient, presumably by facilitating the removal of these elements from the alloy matrix. Applied tensile stresses can also accelerate void nucleation and shorten the transient regime, but only if the duration of the transient is already relatively long. The transient duration cannot be reduced below that of the base Fe-Ni-Cr ternary system by the synergistic action of any of these variables, however. This insight will be used to update the current stress-affected swelling equation for 20% cold-worked AISI 316 and also in the development of a history-dependent swelling equation.

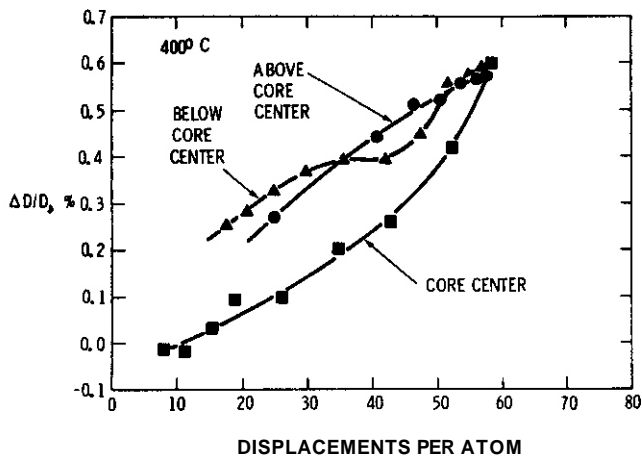


FIGURE 3. Diametral Strains of 5% Cold-Worked AISI 316 at $\sim 400^{\circ}\text{C}$, Showing Influence of Displacement Rate and/or Time-at-Temperature.

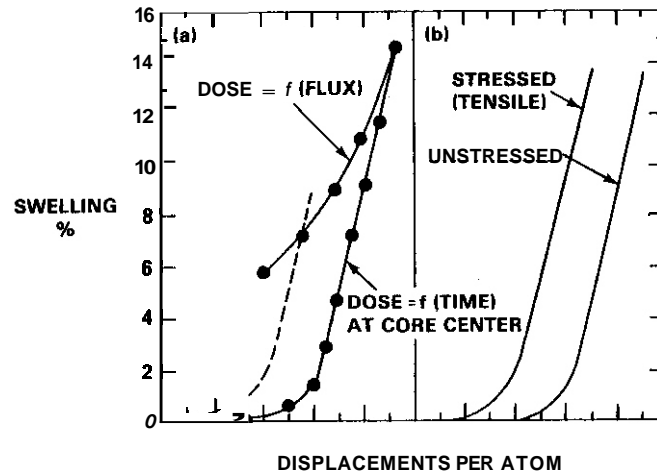


FIGURE 4. Schematic Representation of Separate Effects of Displacement Rate and Applied Stress.

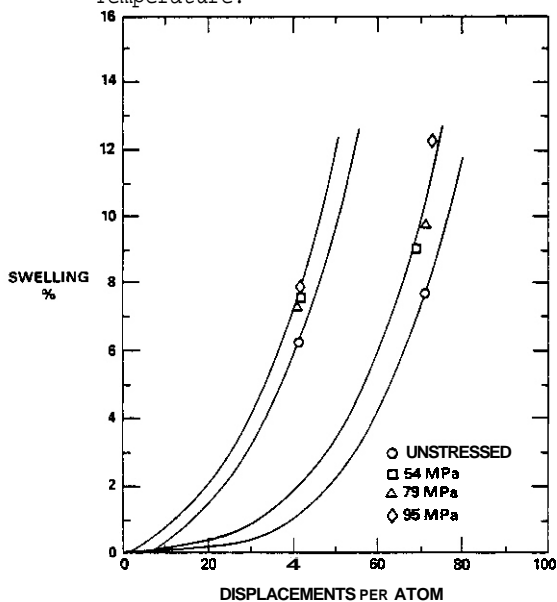


FIGURE 5. Subset of Data Showing Saturation of Stress Influence on Swelling at Relatively Low Stress Levels.

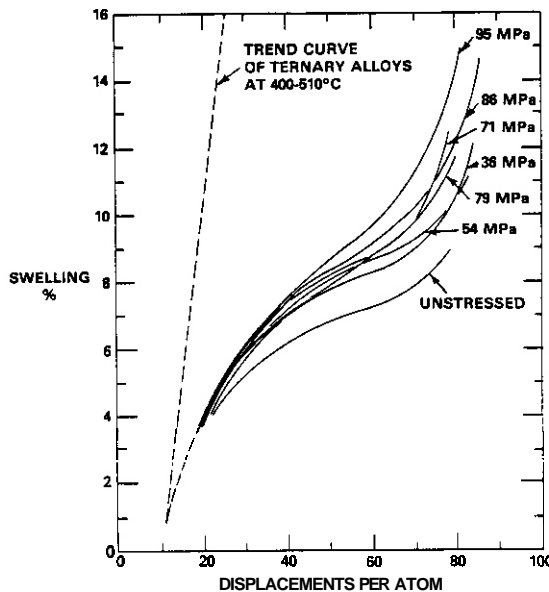


FIGURE 6. Comparison of Seven Swelling Curves from Figures 1 and 2 With Trend Curve from the Ternary Irradiation Series Shown in Figure 7.

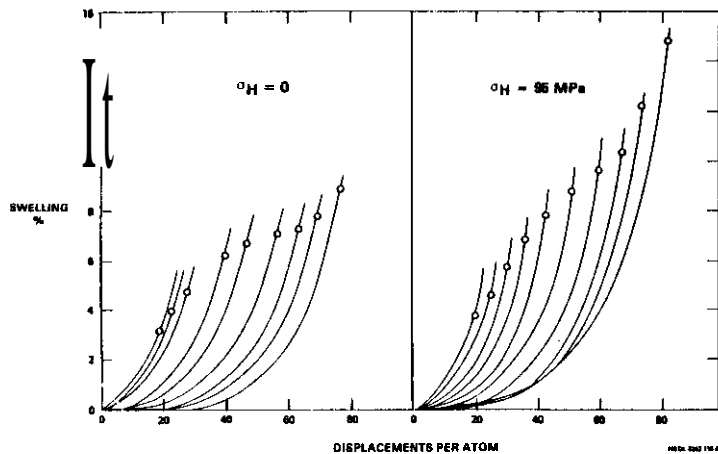


FIGURE 7. Illustration of Flux Dependence of Swelling at Two Stress Levels.

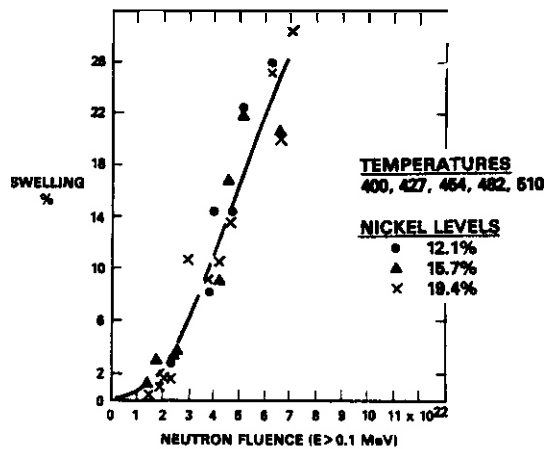


FIGURE 8. Swelling of Neutron-Irradiated Fe-15Cr-Ni Alloys in EBR-II, $\frac{3}{10}$

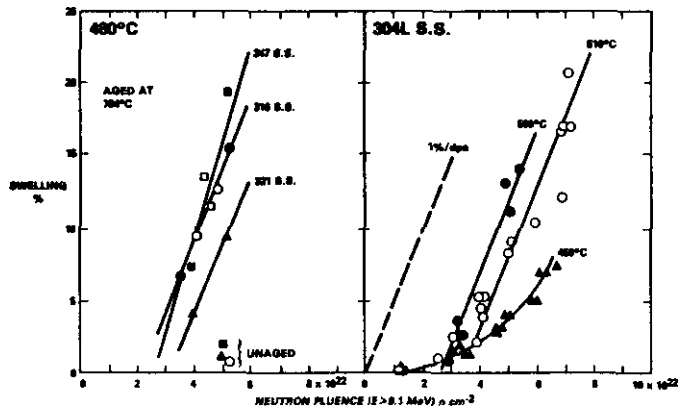


FIGURE 9a. Comparison of Swelling of Aged and Unaged 300 Series Steels.¹⁵
 9b. Swelling of Annealed 304L.¹⁶
 (All four steels were irradiated in EBR-II and swelled at $\sim 1\%/dpa$.)

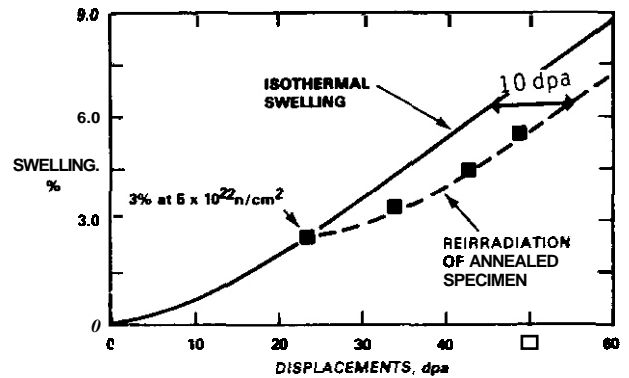


FIGURE 10. Experiment Demonstrating that the 10-dpa Minimum Incubation Period Observed in Annealed 304L at 415°C is Not Related to the Time Required to Nucleate and Grow Voids.**

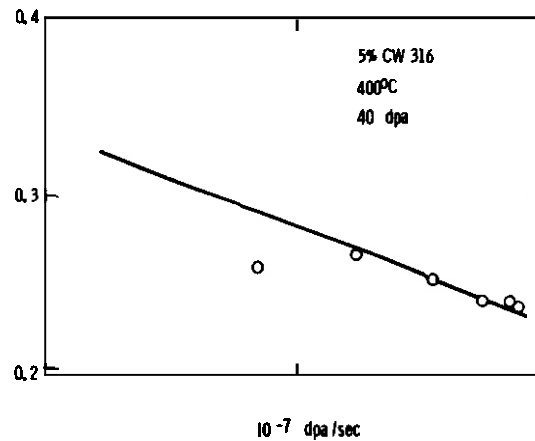
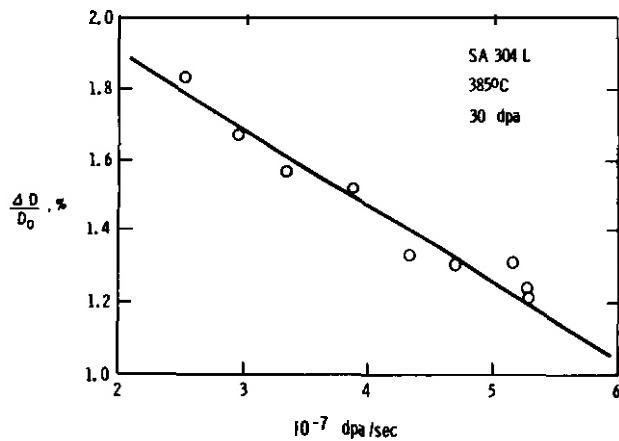


FIGURE 11. Influence of Displacement Rate on Swelling of Annealed AISI 304L and 5% Cold-Worked AISI 316 in EBR-II.

6.0 References

1. F. A. Garner, Proc. Symp. on Phase Stability During Irradiation, eds. J. R. Holland, I. K. Mansur and D. I. Potter, The Metallurgical Society of AIME, 1981, p. 165.
2. J. L. Boutard, G. Brun, J. Lehman, J. L. Seran and J. M. Dupouy, Proc. Symp. on Irradiation Behavior of Metallic Materials for Fast Reactor Core Components, Ajaccio, Corsica, June 5-7, 1979.
3. J. L. Seran and J. M. Dupouy, ASTM STP 782, 1982, p. 5.
4. J. L. Seran and J. M. Dupouy, Proc. Conf. on Dimensional Stability and Mechanical Behavior of Irradiated Metals and Alloys, Brighton, England, 1983, Vol. 1, p. 109.
5. F. A. Garner and D. L. Porter, DAFS Quarterly Progress Report, DOE/ER-0046/9, May 1982, p. 171.
6. F. A. Garner, E. R. Gilbert and D. L. Porter, "Stress-Enhanced Swelling of Metal During Irradiation," ASTM STP 725, 1981, p. 680.
7. F. A. Garner, DAFS Quarterly Progress Report, DOE/ER-0046/5, January 1981, p. 198.
8. D. L. Porter and G. O. Hudman, J. Trans. Amer. Nucl. Soc., 1980, p. 230.
9. F. A. Garner, DAFS Quarterly Progress Report, DOE/ER-0046/14, August 1983, p. 133.

10. F. A. Garner and W. G. Wolfer, "Factors That Determine The Swelling Behavior of Austenitic Stainless Steels," OAFS Quarterly Progress Report, DOE/ER-0046/15, November 1983.
11. F. A. Garner, "Recent Insights on the Swelling and Creep of Irradiated Austenitic Alloys," DAFS Quarterly Progress Report, DOE/ER-0046/16, February 1984.
12. F. A. Garner and W. G. Wolfer, J. Nucl. Mater. **102**, 1981, p. 143.
13. D. L. Porter, G. L. McVay and L. C. Walters, in Ref. 6, p. 500.
14. F. A. Garner, W. V. Cummings, J. F. Bates and E. R. Gilbert, Densification-Induced Strains in 20% Cold-Worked 316 Stainless Steel During Neutron Irradiation, HEDL-TME 78-9, Hanford Engineering Development Laboratory, Richland, WA, November, 1971.
15. H. J. Busboom, G. C. McClellan, W. L. Bell and W. K. Appleby, GEAP-14062, General Electric Report, July 1975, Appendix A.
16. J. E. Flinn and T. A. Kenfield, Proc. Workshop on Correlation of Neutron and Charged Particle Damage, CONF-760673, June 1982, pp. 253-289.

7.0 Future Work

A history-dependent swelling equation will be developed incorporating the insight gained from this study on the stress and flux dependence of swelling.

8.0 Publications

This report will be published in the proceedings of the Twelfth ASTM Symposium on the Effects of Radiation on Materials, to be held June 18-20, 1984 in Williamsburg, Va.

SIMPLE POLYNOMIAL EXPRESSIONS FOR THE HELIUM EQUATION OF STATE

B.B. Glasgow and W.G. Wolfer (University of Wisconsin)

1.0 Objective

To facilitate the use of recently developed equations of state for gaseous and solid helium, simple polynomial fits have been developed.

2.0 Summary

The compressibility factor $z = pV/NkT$ for gaseous and solid helium has been fitted to expressions of the form $z = A + Bx + Cx^2 + Dx^3$, where x is the density and the coefficients A through D are functions of temperature. By fitting this expression to the theoretical results obtained previously, A through D have been determined. These simple polynomial expressions agree to within 11% with the experimental and theoretical results.

3.0 Program

Title: Effect of Radiation and High Heat Flux on the Performance of First-Wall Components
Principal Investigator: W.G. Wolfer

4.0 Relevant OAFS Program Plan Task/Subtask

Task II.C.17 Microstructural Characterization
Subtask II.B.2.3 Correlation Methodology

5.0 Accomplishments and Status

5.1 Introduction

The need for an adequate equation of state for helium at elevated temperatures and at the very high pressures encountered in bubbles has been emphasized previously. (1) Accordingly, theoretical equations of state have been developed previously based on accurate interatomic potentials and elaborate theories for the fluid and the solid State of helium. Comparison of the theoretically derived equations of state with experimental results gave excellent agreement. At very high densities and temperatures, however, where no data exists presently, the solid equations of state developed by Glasgow and Wolfer (1) and by Trinkhaus (2) give somewhat different results for reasons discussed earlier. (3) Nevertheless, the different theoretical approaches give remarkably similar results, as shown in Figs. 1 to 3. Figure 1 and Fig. 2 show the results of Glasgow and Wolfer (1) for the Beck (4) and the Young (5) potential, respectively. Figure 3 gives the equation of state according to Trinkhaus. (2) The dashed curves in the above figures shows the empirical equation of state developed by Mills et al. (6) from their data at and below room temperature. Trinkhaus uses a different empirical fit for his gaseous equation of state to the data by Mills et al., (6) while Glasgow and Wolfer (1) derived their results from first principles using the perturbation theory for dense fluids.

All these equations of state are judged very adequate for applications in void nucleation and growth theories, in models for blistering, and in models for grain boundary cavitation and helium bubble growth. However, the numerical evaluation of the theoretical equations of state by Glasgow and Wolfer⁽¹⁾ are cumbersome. Accordingly, simple polynomial expressions have been developed to represent these theoretical results in a more convenient form.

5.2 Polynomial Form of Equation of State

At low densities, all three equations of state shown in Figs. 1 to 3 give very similar and accurate results. As mentioned before, the results deviate from each other noticeably only at high densities. For these densities, many-body interactions become significant, and pair-wise potentials appear to be no longer adequate. Young et al.⁽⁵⁾ have incorporated in their interatomic potential these many-body effects, and the results derived from their potentials are therefore judged to be the most accurate.

As a result, the polynomial fit is given only for the results derived with the Young potential.

For low densities, covering the gaseous state, the compressibility factor $z = pV/NkT$ can be approximated by

$$z = A_g + B_g x + C_g x^2 + D_g x^3, \quad \text{for } x < 1.7 T^{0.41} \quad (1)$$

where x is the density in (moles/liter) and

$$A_g = (T/1300)^{1/25} \quad (2)$$

$$B_g = 5.83(1/T)^{0.58} \quad (3)$$

$$C_g = \log_{10}(T/800)/(0.69 T^{0.65}) \quad (4)$$

$$D_g = 8.6(1/T)^{1.44} \quad (5)$$

T is the absolute temperature. For the solid equation of state,

$$z = A_s + B_s x + C_s x^2, \quad \text{for } x > 1.7 T^{0.41} \quad (6)$$

where:

$$A_s = -3.89 + 6.59 \cdot 10^{-2} T - 1.15 \cdot 10^{-4} T^2 + 5.46 \cdot 10^{-8} T^3 \quad (7)$$

$$B_s = -0.523 + 4.39 \cdot 10^{-4} T + 1.77 \cdot 10^{-6} T^2 - 1.37 \cdot 10^{-9} T^3 \quad (8)$$

$$C_s = 0.101 - 2.91 \cdot 10^{-4} T + 3.01 \cdot 10^{-7} T^2 - 1.045 \cdot 10^{-10} T^3 \quad (9)$$

Figure 4 gives the comparison for the compressibilities according to the theory and the polynomial fit for three different temperatures, 200, 600, and 1000 K. Within the ranges $200 < T < 1200$ K and $0 < x < 50$ (moles/liter), the agreement is within 11%.

It should be noted that computer programs for both the polynomial fits and for the extensive theory of the helium equation of state are available on the MFE computer network.

5.3 Curvature Corrections

The pressure obtained from the above expressions for $z = pV/NkT$ is for a flat surface. As shown previously,⁽⁷⁾ curvature corrections are required when the equation of state is to be applied to small bubbles with radii on the order of 20 Å or less. At the present time, it is recommended that the pressure obtained from the above expressions be multiplied with an appropriate factor. This factor can be obtained from the graphical results given in Ref. 7 for $P(y,R)/P(y,\infty)$, where R is the bubble radius and y the packing fraction.

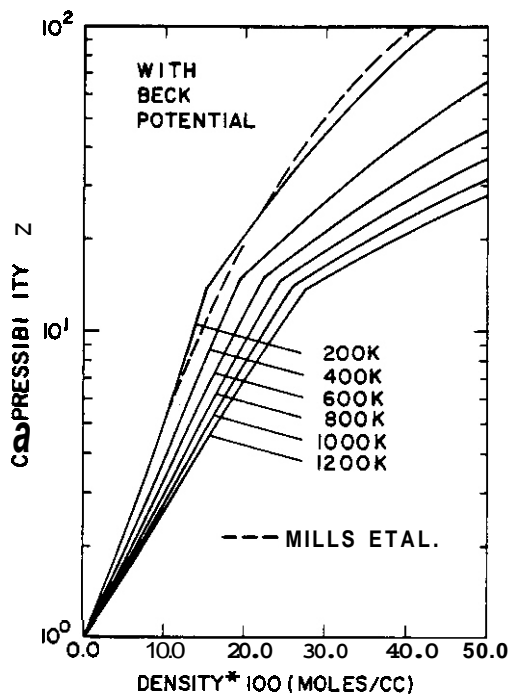


FIGURE 1. Theoretical EOS of Glasgow and Wolfer⁽¹⁾ Using the Beck Potential for Fluid EOS.

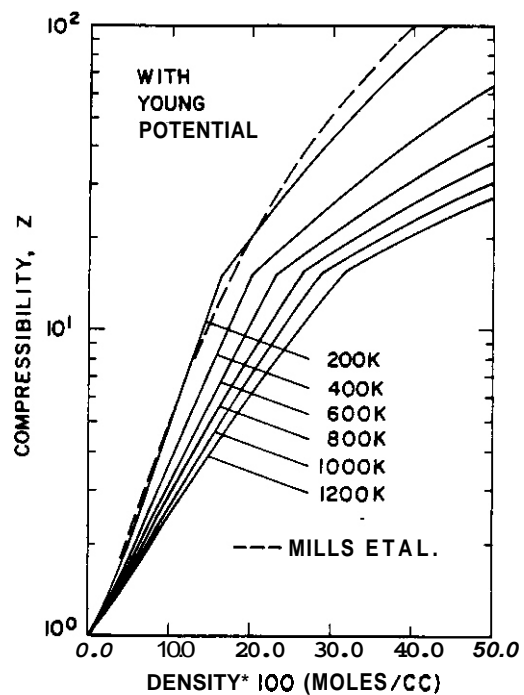


FIGURE 2. Theoretical EOS of Glasgow and Wolfer⁽¹⁾ Using the Young Potential for Fluid EOS.

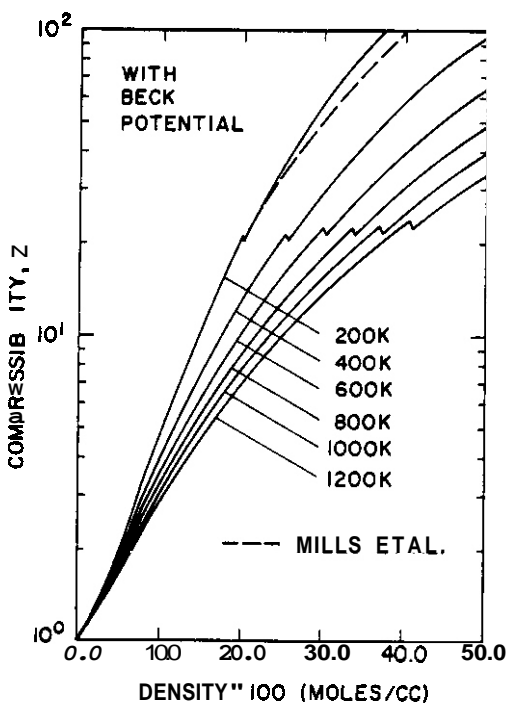


FIGURE 3. EOS for Liquid and Solid States of Helium After Trinkaus.^(2,3)

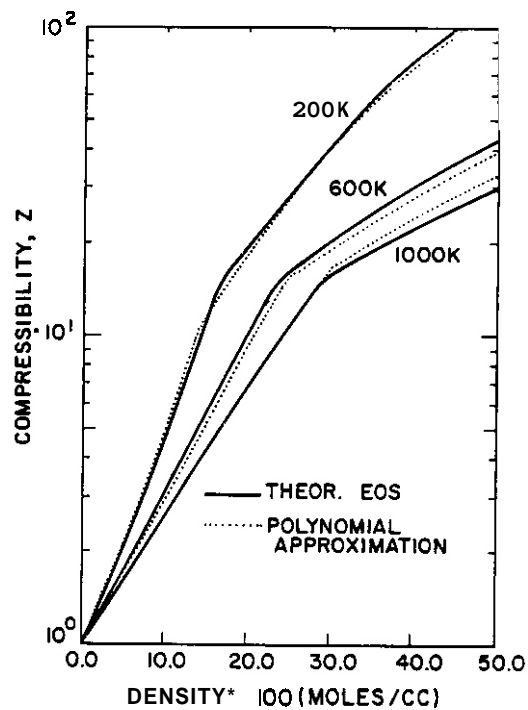


FIGURE 4. Comparison Between the Theoretical EOS and the Approximate Polynomial Fit.

6.0 References

1. B.B. Glasgow and W.G. Wolfer, "Extension and Comparison of Various Equations of State for Gaseous and Solid Helium," DAFS Quarterly Progress Report, DOE/ER-0046/12 (May 1982).
2. H. Trinkaus, "Energetics and Formation Kinetics of Helium Bubbles in Metals," Rad. Effects, **78**, 189-211 (1983).
3. W.G. Wolfer, B.B. Glasgow, M.F. Wehner and H. Trinkaus, "Helium Equations of State for Small Cavities: Recent Developments," Paper presented at the 3rd Topical Meeting on Fusion Reactor Materials, Albuquerque, September 1983, to be published in J. Nucl. Materials. Also, published as Report UWFDM-556, September 1983.
4. D.E. Beck, Mol. Phys., **14**, 311 (1968).
5. D.A. Young, A.K. McMahon and M. Ross, Phys. Rev., **B24**, 5119 (1981).
6. R.L. Mills, D.H. Liebenberg and J.C. Bronson, Phys. Rev., **B21**, 5137 (1980).
7. M.F. Wehner and W.G. Wolfer, "Effect of Bubble Radiation on Equation of State for Gases," DAFS Quarterly Progress Report, DOE/ER-0046/13, Vol. 1, May 1983, pp. 148-163.

7.0 Future Work

Simple polynomial expressions will be developed for the curvature corrections.

EXTERNAL DISTRIBUTIONUC-20 (106)UC-20c (69)DOE-HQ/Office of Breeder
Technology Projects

Washington, DC 20545

PB Hemmig, Asst Director,
Reactor Physics TechDOE-HQ/Office of Fusion Energy (3)
Washington, DC 20545JF Clark, ER-70
JF Decker, ER-54, G-256
S. Parket, ER-62, GTNArgonne National Laboratory (5)
9700 South Cass Avenue
Argonne, IL 60439LR Greenwood BA Loomis
A. Taylor H. Wiedersich
RE NygrenBattelle
Pacific Northwest Laboratory (3)
P.O. Box 999
Richland, WA 99352JL Brimhall
DA Dingee
TD ChikallaBrookhaven National Laboratory
Associated Universities
Upton, Long Island, NY 11973

Chairman, Nuclear Energy Dept

Columbia University
Plasma Physics Laboratory
New York, NY 10027

RA Gross

Commission for the European Communities
200, Rue de la Loi
B-1049 Brussels, Belgium

J. Darvas

Energieonderzoek Centrum Nederland (2)
Netherlands Energy Research Foundation
Westinghouse 3
Postfach 1
NL-1755 ZG Petten, The NetherlandsB. vanderSchaaf
W. vanWitzenburg, Materials DeptEURATOM
Joint Research Center Ispra
Materials Science Division
I-21020 Ispra, Varese, Italy

P. Schiller

General Atomic Company (2)
P.O. Box 81608
San Diego, CA 92138GR Hopkins
JR GillelandHahn-Meitner Institut für Kernforschung
Glienickerstrasse 100
D-1000 Berlin,
Federal Republic of Germany

H. Wollenherger

Hokkaido University (2)
Metals Research Institute
Kita-hu, Sapporo, 060 JapanMihio Kiritani, Precision Eng
Taeo TakeyamaINESCO
11011 Torreyana Rd
San Diego, CA 92121

RD Stevenson

EXTERNAL DISTRIBUTION (Cont'd)

Japan Atomic Energy Research Institute (2)
Physical Metallurgy Laboratory
Tokai Research Establishment
Tokai-mura, Naka-gun, Ibaraki-ken, Japan

Shuichi Iwata, Physics
Kensuke Shiraishi, Nucl Fuel Research

Kernforschungsanlage Julich GmbH
Postfach 1913
D-517 Julich,
Federal Republic of Germany

H. Ullmaier

Kernforschungsanstalt Karlsruhe
Institut für Reaktorbauelemente
Postfach 3640
D-7500 Karlsruhe 1,
Federal Republic of Germany

K. Ehrlich

Kyushu University
Research Institute for Appl Mechanics
6-10-1 Hakozaki, Higashi-ku,
Fukuoka, 812 Japan

Kazunori Kitajima

Lawrence
Livermore National Laboratory (4)
P.O. Box 808
Livermore, CA 94550

W. Barmore
D. Oorn
M. W. Guinan, L-396
C. M. Logan

Lawrence
Livermore National Laboratory
P.O. Box 5511
Livermore, CA 94550

EC Dalder, L-643

Los Alamos National Laboratory (3)
P.O. Box 1663
Los Alamos, NM 87544

DJ Dudziak
CR Emigh
J. Fowler, E-546

Massachusetts Institute of Technology (4)
77 Massachusetts Avenue
Cambridge, MA 02139

I. W. Chen, 13-5118
N. J. Grant, 8-305
L. Lidsky
J. B. van der Sande, 13-5025

Massachusetts Institute of Technology
Nuclear Reactor Laboratory
138 Albany St
Cambridge, MA 02139

OK Harling, NW12-204

Max-Planck-Institut
für Plasma Physik
The NET Team
D-8046 Garching bei München,
Federal Republic of Germany

DR Harries, Technology

McDonnell-Douglas Astronautics Co.
P.O. Box 516
St. Louis, MO 63166

D. Kummer

Mound Laboratory
P.O. Box 32
Miamisburg, OH 45342

Manager, Tech Appl & Oev

National Bureau of Standards
Gaithersburg, MD 20760

JA Grundl

EXTERNAL DISTRIBUTION (Cont'd)

National Research Council
Montreal Road
Ottawa, Canada

EV Kornelson

National Research Institute for Metals
Nuclear Materials Division
1-2-1 Sengen, Sakura-mura,
Niihari-gun, Ibaraki, 305 Japan

Naoki Kishimoto

Naval Research Laboratory (3)
Washington, DC 20375

I. Manning, Code 6672
JA Sprague, Code 6395
LE Steele, Code 6390

North Carolina State University
Department of Nuclear Engineering
Raleigh, NC 26707

JR Beeler Jr

Oak Ridge National Laboratory (12)
P.O. **Box** X
Oak Ridge, TN 37830

| | |
|--------------|------------------|
| Director | M. Roberts |
| K. Farrell | J. Sheffield |
| ML Grossbeck | JD Stiegler |
| PJ Maziasz | C. Weisbin |
| LK Mansur | FW Wiffen |
| NH Packan, | Bldg 9204-1 |
| FG Perey, | Bldg 9201-2 |

Osaka University (2)
2-1, Yamada-oka, Suita,
Osaka, Japan 565

Kenji Sumita, Dept of Nuclear Eng
Toichi Okada, Institute of
Scientific & Industrial Research

Princeton University (2)
Plasma Physics Laboratory
Forrestal Campus
P.O. Box 451
Princeton, NJ 08544

H. Furth
K. Wakefield

Risø National Laboratory
Postfach 49
DK-4000 Roskilde, Denmark

B.N. Singh

Rockwell International
8900 DeSoto Ave
Canoga Park, CA 91304

O. Kramer

Sandia National Laboratories (2)
P.O. **Box** 5800
Albuquerque, NM 87185

FL Vook, Org 5100

Sandia National Laboratories (2)

W. Garrison, Div 8314
WO Wilson

Science Applications, Inc.
1200 Prospect
LaJolla, CA 92037

Or. H. Gurol

Science University of Tokyo
Engineering Dept
Kagurazaka, Shinjuku-ku,
Tokyo, 162 Japan

RR Hasiquti

EXTERNAL DISTRIBUTION (Cont'd)

Studiecentrum voor Kernenergie
Centre d'Etude de l'Energie Nucleaire
Boeretang 200
 B-2400 Mol, Belgium

J. Nihoul

Swiss Federal Institute
for Reactor Research
 CH-5303 Wuerenlingen, Switzerland

WV Green

Tokyo Institute of Technology
 12-1, 2-Chome, O-okayama
 Meguro-ku, Tokyo, Japan

Kensutaka Kawamura

United Kingdom Atomic Energy Authority
Atomic Energy Research Establishment
Oxfordshire, UK

R. Bullough, Theoretical Physics Div

United Kingdom Atomic Energy Authority
Culham Laboratory
Applied Physics and Technology Div
 Abingdon, Oxfordshire OX14 30B, UK

GJ Butterworth

university of California (2)
 Los Angeles, CA 90024

RW Conn
 NM Ghoniem

University of Michigan
Nuclear Engineering
 Ann Arbor, MI 48109

T. Kammash

University of Missouri
Mechanical & Aerospace Eng
 1006 Engineering Bldg
 Columbia, MO 65211

M. Jolles

University of Missouri
Dept of Nuclear Engineering
 Rolla, MO 65401

A. Kumar

University of Tokyo (3)
 7-3-1 Hongo
 Bunkyo-ku, Tokyo 113, Japan

Naohira Igata, Met & Mater Science
 Shiori Ishino, Nuclear Eng
 Taijiro Uchida

University of Virginia
Dept of Materials Science
 Charlottesville, VA 22901

WA Jesser

University of Wisconsin
 1500 W. Johnson Drive
 Madison, WI 53706

WG Wolfer

Westinghouse
Advanced Energy Systems Division
Fuels Materials Technology
 P.O. Box 158
 Madison, PA 15663

A. Boltax, Manager

Westinghouse
Research and Development Center (2)
 1310 Beulah Road
 Pittsburgh, PA 15235

JA Spitznagel
 S. Wood

INTERNAL DISTRIBUTION

DOE-RL/AMPF (2)
 FMI Facility Project Office
 FED/675

GM Chenevert, Proj Mgr

HEOL (31)

| | |
|-------------|--------|
| SO Atkin | W/A-58 |
| HR Brager | W/A-58 |
| LL Carter | W/B-47 |
| DG Doran | W/A-57 |
| EA Evans | W/C-23 |
| FA Garner | W/A-58 |
| DS Gelles | W/A-58 |
| R. Gold | W/C-39 |
| WV Hagan | W/M-81 |
| HL Heinisch | W/A-58 |
| DL Johnson | W/A-4 |
| GD Johnson | W/A-65 |
| FM Mann | W/A-4 |
| WN McElroy | W/C-39 |

DOE-RL/AMAR
 breeder Technology Division
 Technology Development Branch
 FED/210

KR Absher, Chief

| | |
|--------------------|---------|
| EK Opperman | W/A-58 |
| NF Panayotou | W/A-65 |
| RW Powell | W/A-58 |
| RJ Puigh | W/A-58 |
| FH Ruddy | W/C-39 |
| FA Schmittroth | W/A-4 |
| WF Sheely | W/C-62 |
| RL Simons | W/A-57 |
| JL Straalsund | W/A-61 |
| HH Yoshikawa | W/C-44 |
| Central Files (3) | W/C-110 |
| Publ Services | W/C-115 |
| Microfilm Services | W/C-123 |
| Program Files (2) | W/A-57 |

